MICROMACHINED BIOMIMETIC OPTICAL MICROPHONES WITH IMPROVED PACKAGING AND POWER CONSUMPTION

A Thesis
Presented to
The Academic Faculty

by

Frederic A. Banser Jr.

In Partial Fulfillment
of the Requirements for the Degree
Master of Science in the
George W. Woodruff School of Mechanical Engineering

Georgia Institute of Technology
May 2012

MICROMACHINED BIOMIMETIC OPTICAL MICROPHONES WITH IMPROVED PACKAGING AND POWER CONSUMPTION

Approved by:

Dr. F. Levent Degertekin, Advisor
George W. Woodruff School of Mechanical Engineering
Georgia Institute of Technology

Dr. Todd Sulchek
School of Mechanical Engineering
Georgia Institute of Technology

Dr. Venkatesh (Venky) Sundaram
School of Electrical Computer Engineering
Georgia Institute of Technology

Date Approved: March 2012

To my family,

for all of their support over the years.

ACKNOWLEDGEMENTS

This work would not have been possible without the help and guidance of a number of individuals. I would like to first thank my thesis advisor, Professor F. Levent Degerteking, it was through his mentorship and wisdom that I was able to complete this thesis, as well as help me develop myself as an individual and an engineer. I would also like to thank the members of my thesis reading committee; Dr. Todd Sulchek, and Dr. Venkatesh Sundaram for their constructive feedback.

I am grateful also the members of the Micromachined Sensors and Transducers (MiST) Laboratory their support and guidance helped me greatly throughout my Masters. Especially to Dr. Baris Bicen, it was through his work and initial mentorship that lead me to the results that have been achieved today. I also, owe thanks to all the previous members of MiST who contributed to the microphone project.

I would also like to thank the Vibrations Research Laboratory at Binghamton University New York. Specifically to Professor Ron Miles and Dr. Weili Cui for supplying the microphone diaphragms and their valuable insight to the project. I would also like to thank the Integrated Acoustics Laboratory, especially Professor Ken Cunefare, who allowed me to use their equipment and test facilities at Georgia Tech.

TABLE OF CONTENTS

LIST OF TABLES

LIST OF FIGURES

SUMMARY

Low noise, directional microphones are critical for hearing aid applications. Specifically, the use of directional microphones in hearing aid applications can improve a person's speech intelligibility in noisy enviroments. For hearing aid applications, directional microphone technology is currently limited by scaling issues, noise levels, and device operation frequency range. This thesis is focused on further development of a biomimetic micromachined directional microphone based on the ear structure of the *Ormia Ochracea*, a parasitic fly able to locate sound sources in the audio frequency range with high accuracy.

The objective of this thesis have been on implementing a newer version of the directional microphone for a behind the ear (BTE) package while improving the overall optical efficiency and noise level. Technical challenges associated with creation of the new device package included: implementing a microfabricated lens array, active alignment of the new revision of the biomimetic microphone diaphragm, and characterization of the new package with improved optics. Operation issues with the device were also investigated by demonstrating pulsed laser operation for reduced power consumption, and electrostatic control of the microphone diaphragm position for stable operation over a long time.

The new packaging method for the microphone addressed the need for tighter placement tolerances along with a redesigned diaphragm and integration of a microscale optical lens array to improve the optical efficiency of the device. The completed packages were characterized for sensitivity improvement and optical efficiency. The overall optical efficiency was significantly increased from less than 1% to the

photo diode array collecting 50% of the emitted optical power from the Vertical Cavity Surface Emitting Laser (VCSEL). This, coupled with the new diaphragm design, improved the acoustic performance of the microphones. Consequently, the noise levels recorded on the devices were about 31 dBA SPL, more than 15dB better than conventional directional microphones with nearly 10 times larger port spacing.

Since the application for this technology is hearing aids, the power consumed by the working device needs to be at an acceptable level. The majority of the power used by the microphone is from continuously operating the VCSEL with 2mW optical output power. To reduce this power requirement, it was suggested to pulse the VCSEL at high enough frequency with low duty cycle so that the acoustic signals can be recovered from its samples. In this study, it was found that the VCSEL can be pulsed with little to no degradation in signal to noise ratio as long as the thermal mechanical noise dominated the noise spectrum. The results also indicated that a pulse train with a duty cycle of around 20% can be used without a major loss of performance in the device, meaning the device can effectively run at 1/5 of its original power under pulsed operation mode.

Finally, a control technique to overcome some inherent problems of the microphone was demonstrated. Since the optical sensitivity of the microphone depends on the gap between the diaphragm grating and the integrated mirror, it is important to keep that bias gap constant during long term operation against environmental variations and charging effects. Using a simple electrostatic bias controller scheme, the sensitivity variation of the microphone was improved by a factor of 8 with bias control. Overall, this thesis has addressed several important aspects of a micromachined biomimetic microphone and further demonstrated its feasibility for hearing aid applications.

CHAPTER I

INTRODUCTION

This chapter introduces sound measurements used in industry and for commercial applications. It will also discuss different acoustic detection methods for sound pressure and intensity. The chapter then compares these devices and detection methods through discussion of their advantages and limitations, giving motivation for the work completed on the biomimetic directional optical microphone.

1.1 Sound Measurements

Sound can be described as the mechanical vibration of particles moving through a medium. These oscillations can be characterized in different forms in order to understand their properties. The most common characterization methods for sound are measurements in the form of pressure and intensity.

Sound pressure is measured via local pressure deviations from the ambient environment. The actual measurement is quantified as a force per unit area which in metric units is a Pascal (N/m^2). For comparison the pressure measurement is normalized to a reference pressure of 20 μPa. This reference level comes from a reference standard intensity of 10^{-12} W/m^2, which is thought to be the lower threshold of human hearing at 1 kHz. Using the Root Mean Square (RMS) value of the measured pressure a pressure level can be determined as shown in the following.

$$L_p = 10 \cdot \log \frac{P_{rms}^2}{P_{ref}^2} \text{ where } P_{ref} = 20\mu Pa \tag{1}$$

Equation 1 is how sound pressure level (SPL) is calculated. The importance of sound pressure measurements is that this is the form that human ears perceive sound.

Often in addition to normalizing the pressure to the lower threshold of human hearing the pressure level is filtered to a weighting curve. For standard hearing an A-weighting is used.

$$R_A(f) = \frac{12200^2 \cdot f^4}{(f^2 + 20.6^2)\sqrt{(f^2 + 107.7^2)(f^2 + 737.9^2)}(f^2 + 12200^2)}$$
$$A_{wgt}(f) = 2.0 + 20 \log R_A(f) \tag{2}$$

The A-weighting equation shown above in Equation 2 is a filtering curve that is normalized to 1 kHz and has a global maximum around 3 kHz. By applying this filter to collected data the pressure measurement can tell how "loud" a pressure wave will be perceived by a person. The range for human hearing is from 20 Hz to 20 kHz and so most sound measurements try and have good measurement within this frequency band.

Another widely used measurement for pressure variations is an intensity measurement. Unlike pressure measurements which are scalar quantities the velocity measurement contains directionality information about the measured pressure wave. The intensity level is useful in determining the position of a sound source as well as finding the sound power emitted by one such source. The intensity can be described as a time-averaged product of a wave's pressure and particle velocity; however, particle velocity can be related to pressure gradient so that can also be used to collect intensity measurements. For this reason there are two accepted methods for determining the sound intensity of a source, these are through a Pressure-Pressure (PP) and Pressure-Velocity (PU) method. Both methods will be discussed further in a later section. Sound intensity is measured in acoustic power per area and has a reference value that it can be normalized to, which was mentioned previously as 10^{-12}W/m^2. The intensity level then can be defined as follows.

$$L_I = 10 \cdot \log \frac{I_{rms}}{I_{ref}} \text{ where } I_{ref} = 10^{-12} W/m^2 \tag{3}$$

The motivation for using intensity over pressure measurements is that since this value is not a scalar value measurements of a source can be made in a variety of sound fields. For example power measurements of a machine can be measured on a factory floor instead of setting a single machine up in a controlled room like an anechoic chamber. In addition the intensity measurements can be taken in the nonlinear near field, which is problematic for pressure measurements.

1.2 Capacitive Microphones

There are many different sensing techniques that are available for pressure measurement. The basic principle of a microphone is that the device can convert mechanical pressure differences into the electrical domain for sensing.

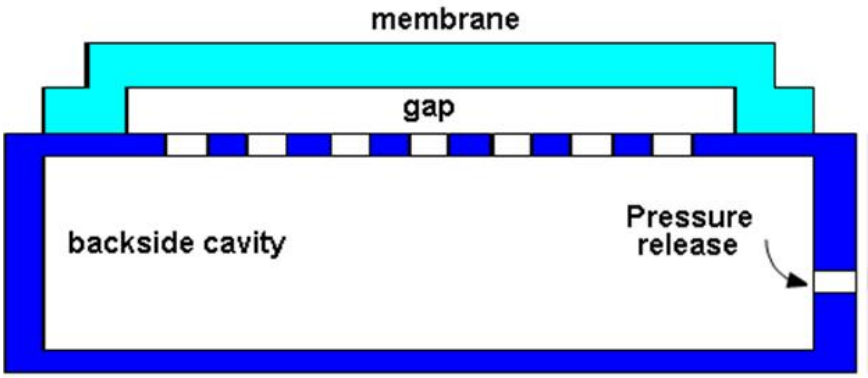

Figure 1: A cross section view of a condenser microphone [14]

Figure 1 shows a condenser microphone schematic. The mechanical vibrations of the acoustic wave are obtained via a diaphragm that contains two different pressure fields on either side of it. One of the sides is exposed to the open environment and the other is a shielded backside cavity that is representative of the ambient pressure in the environment. The vibration of the diaphragm is the result of differences between the

two pressure fields. The other component of the microphone is its ability to transduce the pressure signal from the mechanical to electrical domain. The most common way microphones address this issue is through parallel plate gap capacitance. The two electrodes making this gap capacitor is the microphone diaphragm which in most cases is grounded and a rigid back plate that is charged either via a voltage bias or by materials that are precharged. Typically the former is used for microphones but the latter can be used to reduce the voltage level of the microphone especially since biasing voltages can be in the range of 200V. The transduction principle for the capacitive measurement is shown as follows.

$$\begin{aligned} V \cdot C &= Q_0 \\ (V_0 + v) \cdot \frac{\epsilon \cdot A}{D_0 + d} &= V_0 \cdot \frac{\epsilon \cdot A}{D_0} \\ S_e = \frac{v}{d} &= \frac{V_0}{D_0} \end{aligned} \tag{4}$$

In Equation 4, V is the instantaneous voltage in the system, D is the displacement of the system, A is the electrode area, ϵ is the dielectric constant of air, C is the instantaneous capacitance, and Q represents the charge between the gaps. A lower case of each letter denotes the variation of that variable from rest position and a subscript of 0 is its initial value. The formulation of voltage measured to gap displacement is derived from the charge being held constant. As seen in Equation 4 the result yields a linear relationship between gap displacement and change in voltage.

To have a good microphone a good signal to noise ratio (SNR) is desired from any design, which is heavily reliant on the microphone's sensitivity. Since the microphone is defined in two domains i.e. the mechanical and electrical, the sensitivities of such microphones relies on these two components. [8, 25]

The first is the diaphragms mechanical sensitivity (S_m) which is the ratio of gap displacement to a pressure input. Since the diaphragm can often be modeled as a

simple spring mass damper system, this sensitivity component of the microphone is mostly dependent on the diaphragm's dynamics, although issues like air stiffness and venting may contribute to this sensitivity.

$$S_m = \frac{p}{x} = \frac{A}{m\frac{d^2}{dx^2} + b\frac{d}{dx} + k} \tag{5}$$

The Equation 5 shows the second order differential equation that can be used for the mechanical sensitivity of the microphone. Here A is the diaphragm area, m is the mass of the diaphragm, b is the microphone's damping constant, and k is the device's stiffness. From a design prospective it is desirable for a microphone diaphragm to have small mass to detect smaller pressure signals and large compliance for large displacement values. Optimal damping values are determined by the pressure field that the device will measure for example critical damping is used for pressure field microphones while over damping are used in the free field.

The other component to the microphones sensitivity is the electronic sensitivity (S_e). This involves the microphones ability to take the diaphragms displacement due to variations in pressure and convert it into an electrical signal. As seen in Equation 4, the voltage measured is largely due to the initial charge imposed onto the device. Thus the capacitance measurement has dependence on the area, bias voltage and initial gap of the capacitor. For high electrical sensitivity it is desirable that the microphone has a large sensing area with small air gap. The overall sensitivity is the combination of the mechanical and electrical sensitivities i.e. $S = S_m \cdot S_e$. Also, optimization of a microphones sensitivity is not trivial as there are tradeoffs between the parameters which will be addressed later.

While microphone technology has been in existence for an extended period of time and been developed to a high degree of precision and low noise levels. [6, 7, 9, 16, 32, 39, 44, 49, 51] The emergence of technologies such as the cell phone has created a need

for the mirofabrication of microphones with similar performance; however, scaling the capacitive microphone is difficult for several reasons. [21] As mentioned above the electrical sensitivity is directly proportional to the capacitive area of the device which is proportional to length squared making sensitivity of the microphone drop off very quickly at small sizes. While problematic, this can be offset in a number of ways for example by making the gap smaller. The decrease in gap size, while being a good solution to the decrease in sensing area of the microphone, can lead to another problem occuring in the damping of the membrane. The air gap in a microphone adds a certain amount of resistance and compliance to the mechanical sensitivity; this is due to air behind the diaphragm compressing and venting out from the air gap when the diaphragm is displaced. Normally for larger sized microphones the area and volume of the air gap is large enough to compensate for this; however, when the size of the microphone is reduced the volumetric damping no longer dominates the air gap and squeeze film effects which scale with area now dominate. If not properly vented, the diaphragm is stiffened significantly and the diaphragm starts to exhibit lag in its pressure measurements caused by choking of the vent holes. [13] So there exists a trade off in that by venting the back plate even more sensing area is lost or having the air gap effectively stiffen and dampen the membrane. Often microphone designs use the air gap venting to fine tune the diaphragm's damping ratio to an acceptable value for the pressure field being measured.

Another design issue that arises with the microfabrication of capacitance microphones is the biasing of the microphones diaphragm. Typically, not including the precharged designs, to improve both electrical and mechanical sensitivity an electrostatic bias on the gap capacitor is applied. This serves to electrically soften the mechanical spring constant as well as reduce the gap distance. The limiting factor to this approach is that there is an inherent instability associated with this system commonly known as snap down, where at a certain point of biasing (approximately

deflections of 1/3 of the original gap or more) the effective spring constant of the diaphragm is zero and so with no restoring force left in the system the diaphragm crashes into the back plate. This is problematic because it not only limits the modulation of the diaphragm but it may also destroy the device's diaphragm which are fragile. Snap down voltage for a capacitor is as follows.

$$V_{snap} = \sqrt{\frac{8KD_0^3}{27A\epsilon}} \tag{6}$$

Here, the new variable K is the spring constant for the device. So as the size of the microphone is reduced the operating voltage for the device has to be reduced as well to avoid this phenomenon. This further illustrates the tradeoffs that exist when trying to reduce the size of the microphone. While many drawbacks exist for capacitive microphones in MEMs packaging, the capacitive microphone technology sets the standard for pressure measurements in a variety of pressure fields, and has been proven useful in many markets and industries to this day.

1.3 Optical Microphones

As shown in the previous section, scaling is a major issue with current capacitive microphone technology. To circumvent some of these drawbacks different transduction methods have been of interest to pressure measurement. In particular, optical detection shows a lot of promise in this field. [15]

Optical transduction methods are particularly attractive because of their scaling and physical properties. In particular, light can be classified by its intensity, polarization, and phase. [31,36,43] This section will focus on interferometer measurement. While the other types have shown to be successful in observing small vibrations due to pressure variations, phase measurement has been more successful and more accepted. Phase modulation usually is a variation of four forms. They are the Fabry Perot, Mach Zehnder, Two mode fiber, and the Michelson. The simplest to implement and

as a result the most common is the Michelson, which will be focused on.

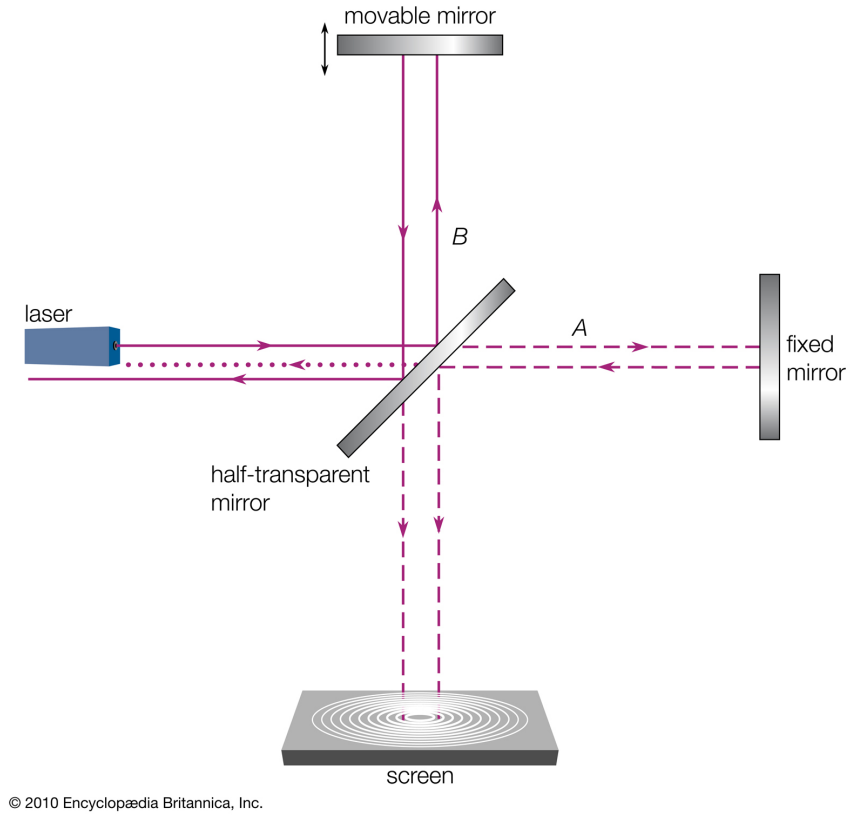

Figure 2: A schematic of a Michelson interferometer [11]

The Michelson setup is shown in Figure 2. The setup contains a coherent light source, a beam splitter, a fixed reference surface, a movable surface, and a type of light detector. The Michelson interferometer is a two pass phase phase modulator, since light is reflected back instead of moving in a single path, and the output signal is a result of a phase difference between two beams. As seen from Figure 2 the coherent source is split into two beams a reference beam that hits a mirror of known and fixed position and another mirror that is allowed to vibrate with an external input. The two beams after hitting their reflecting surfaces are allowed to interfere with each other either constructively, destructively, or a combination of the two.

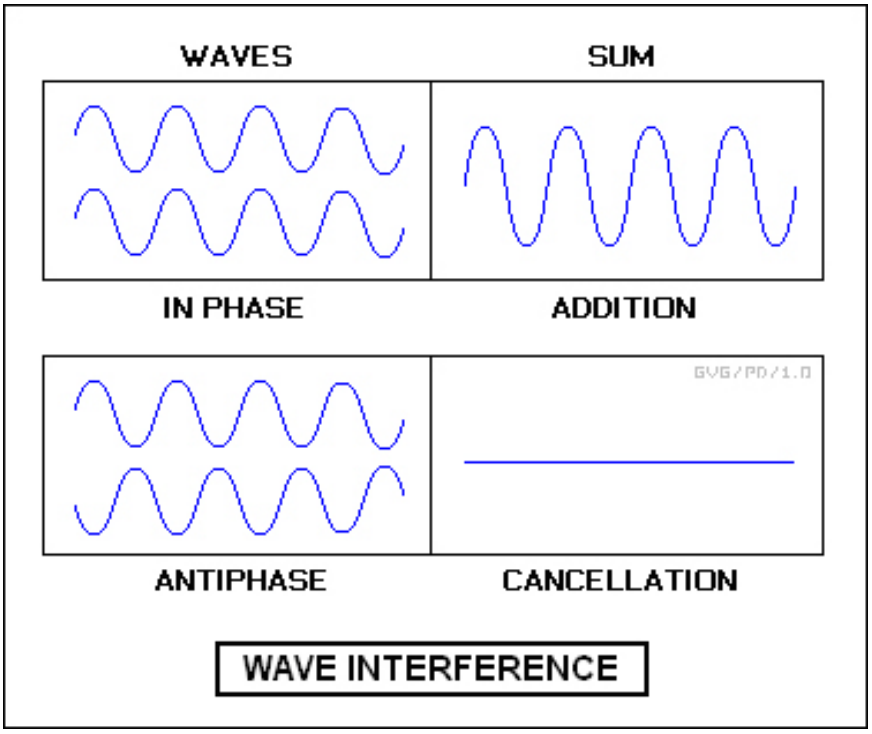

Figure 3: Interference patterens [5]

Figure 3 shows constructive and destructive interference of a waveform. As seen in this figure whether destructive or constructive interference is present is heavily dependent on the phase of each waveform being combined. As mentioned before the source of the interferometer is a coherent source and so these measurements make the important assumption that the testing is conducted within the sources coherent length and time. How the interferometer actually detects movement can be attributed to the Doppler effect. For a Michelson interferometer, the generated output is a combination of the electric fields of the test and reference beams, of the following form.

$$E_{ref} = E_{0ref} \cos(\omega_0 t - 2k_0 L_{ref}) \tag{7}$$

$$E_{test} = E_{0test} \cos(\omega_0 t - 2k_0 L_{test} - 2k_0 \mu) \tag{8}$$

In Equation 7, E is the electric fields of both the reference and test beam, ω_0 is the frequency of the coherent laser being used k_0 is the optical wave number which

is 2π divided by the wavelength of the source, L_{ref} and L_{test} are the distances to the reference and test mirrors respectively, lastly μ represents the displacement of the test mirror from its resting place. Since the voltage output is proportional to the intensities of these quantities the sum of the electric fields must be squared and averaged over time. Expanding these squared quantities yields the following formula.

$$\begin{aligned} V_{out} = \alpha_{Photodiode}\langle 0.5(E_{0ref}^2 + E_{0test}^2)\cdots \\ + 0.5E_{0ref}^2\cos(2\omega_0 t - 4k_0 L_{ref}) + 0.5E_{0test}^2\cos(2\omega_0 t - 4k_0 L_{test}\cdots \\ - 4k_0\mu) + E_{0ref}E_{0test}\cos(2\omega_0 t - 2k_0(L -_{ref} + L_{test}) - 2k_0\mu)\cdots \\ + E_{0ref}E_{0test}\cos(2k_0(L_{test} - L_{ref}) + 2k_0\mu)\rangle \end{aligned} \tag{9}$$

The $\alpha_{photodiode}$ term is a constant associated with the photodiode used, $\langle\rangle$ denote a time average of the values within them. To simplify Equation 9 contributions to the output containing the sources frequency will be zeroed out. Thus any term with ω_0 can be cancelled out of the equation, this is valid under the assumption that the period of the source is much smaller than the response time of the photodiode, thus the time average of any term with ω_0 will yield 0. This leaves only the first and last terms in Equation 9,the first term produces a DC constant, while the last is an AC signal based on the displacement of the test surface. Just looking at the AC term the equation for voltage output becomes as follows.

$$\begin{aligned} V_{out} &= E_{0ref}E_{0test}\cos(2k_0(L_{test} - L_{ref}) + 2k_0\mu) \\ &= E_{0ref}E_{0test}(\cos(2k_0\mu)\cdot\cos(2k_0(L_{test} - L_{ref}))\cdots \\ &- sin(2k_0\mu)\cdot\sin(2k_0(L_{test} - L_{ref}))) \end{aligned} \tag{10}$$

Since sound pressure is small variations in a pressure field it can be assumed that the relative deflection of the test surface is small, and so small angle approximation can be used to further reduce Equation 10 into the following final form.

$$V_{out} = E_{0ref}E_{0test}(\cos(2k_0(L_{test} - L_{ref})) - 2k_0\mu \cdot \sin(2k_0(L_{test} - L_{ref})) \qquad (11)$$

The leftover trigonometric terms are a result of ambient conditions in the test setup which may fluctuate over time. The important thing to note though about Equation 11 is that the dependence on the output voltage to displacement of the test surface is linear.

The advantages for use of optical detection schemes for acoustic sensing are that high sensitivity can be achieved through interferometric transduction. The modulation of a signal is every half period of the source i.e. $\lambda/2$, which for most light sources can be in the nanometer range. Another advantage for this type of sensor is that there doesn't need to be a back plate for the device so squeeze film damping effects are reduced. A disadvantage to this approach is that it adds to the complexity of the device as it needs additional components like a light source and photo detector. Also, depending on the light source the device may require more power than a capacitive microphone of similar dimension.

1.4 Directional Microphones

A large role that directional microphones have is the ability to be able to assign vector quantities to observed pressure levels. This allows for such a device to be able to measure sound pressure from a source in a range of conditions as well as allow for pressure intensity to be measured directly. [45] As mentioned earlier there are two methods that are commonly used to detect such measurements in air, the PP and PU methods. [29, 30]

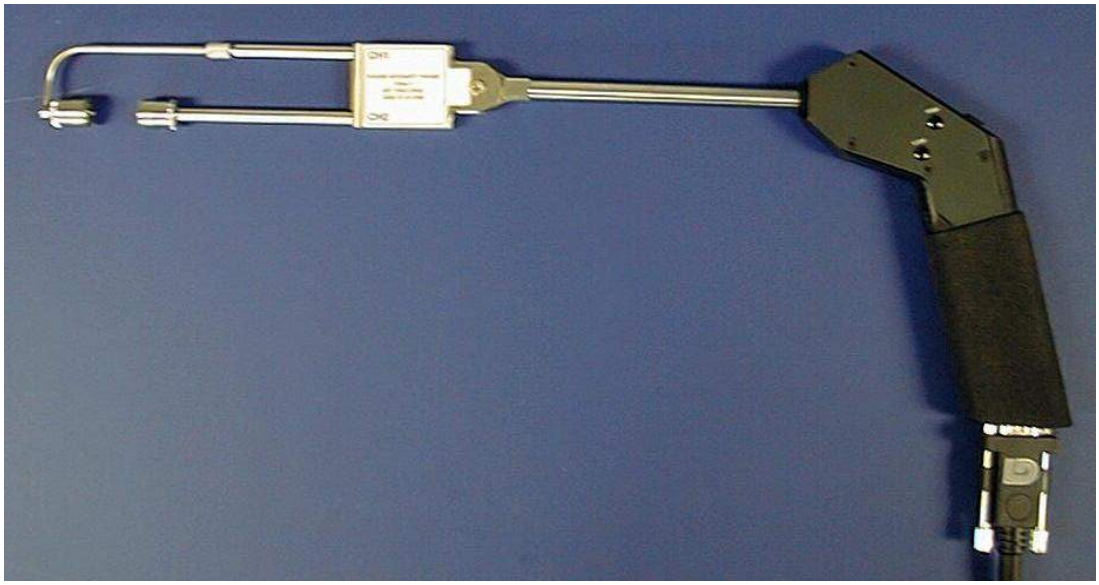

Figure 4: Directional microphone using two inphase microphones [10]

The PP or pressure-pressure method utilizes pressure gradients in order to determine particle velocity, Figure 4 shows one such PP directional microphone. This particular type of PP directional microphone needs good phase matching between the two microphone diaphragms, which is also why the microphones face each other when separated by a spacer. This detection method is considered the most successful method in measuring sound intensities in air thus far. Specifically, the method uses a finite-difference approximation in order to estimate the particle velocity of the pressure wave. Through the use of Euler's equation a relationship between pressure gradient and particle velocity is formed.

$$u = -\int \frac{1}{\rho}\frac{\delta P}{\delta r}dt \tag{12}$$

The term ρ is the density of the medium, t is time, P is pressure, and r is the distance along the pressure wave. From Equation 12 in order to determine $\delta p/\delta r$ from the two microphones a finite difference is calculated from the two measurements. The resulting formula is shown in Equation 13.

$$u = -\int \frac{1}{\rho} \frac{P_B - P_A}{\Delta r} dt \tag{13}$$

When Equation 13 is combined with average pressure to get the intensity measurement the end result is as follows.

$$I = \langle u \cdot P \rangle = -\frac{P_A + P_B}{2\rho\Delta r} \int (P_B - P_A) dt \tag{14}$$

As one can see the distance Δr is important to the detection of intensity. For an accurate measurement the microphone or port spacing of the directional microphone must be a set length for a frequency range. This is because if the spacing is too large the phase difference will not be representative of the waveform, since the gradient will be much shallower than the actual waveform. If the spacing is too narrow there is a degradation of the device's sensitivity making measurement difficult as illustrated in Figure 5.

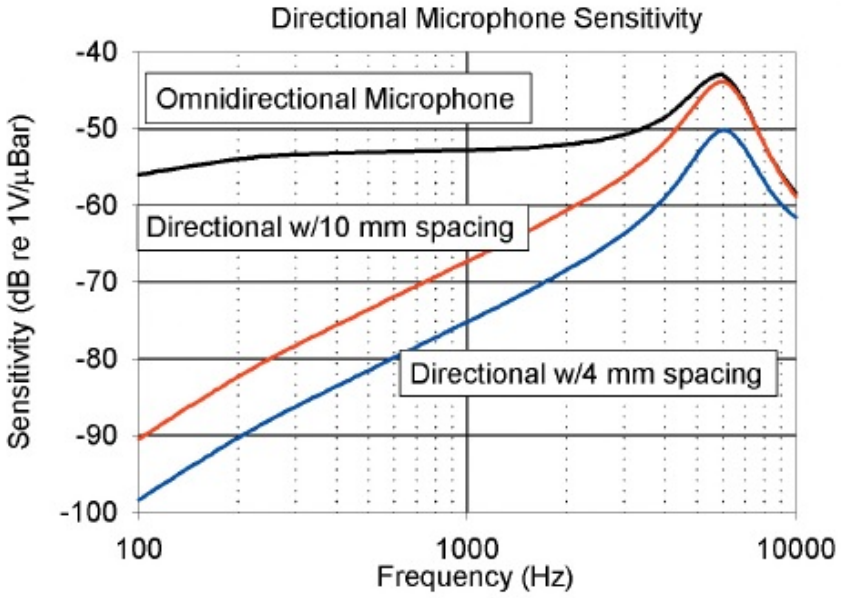

Figure 5: Directional sensitivity profile for different port spacing [48]

A unique property of the PP type directionality microphone is their directivity profiles. Since their measurements contain phase data of the pressure their sensitivity

profiles are dependent on the incident angle of the pressure wave.

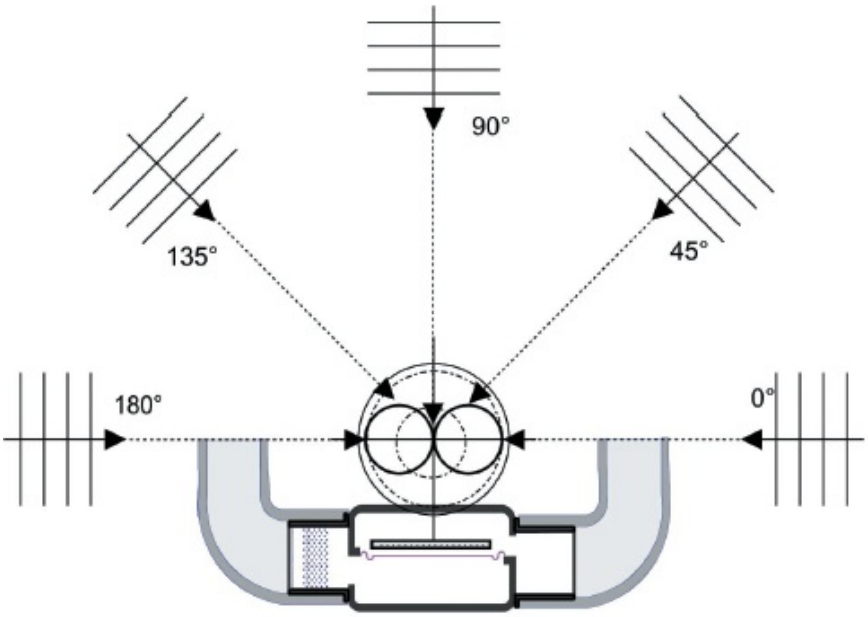

Figure 6: Directional profile of a 2 port microphone [48]

In Figure 6 a schematic of a directional microphone is shown other than the one in Figure 4, with this setup the two microphones are replaced with two ports. As discussed in the capacitive microphone section movement of the microphone diaphragm is the result of a pressure differential between the environment pressure field and the back side cavity pressure field on either side of the diaphragm. For this two port design the back side cavity is opened up to the environment so any detected movement of the diaphragm is a result of a phase difference across the two ports. Also shown in Figure 6 is the figure eight directivity profile that is typical of most directional microphones. As one can imagine the phase difference at zero and 180 degrees offers the most sensitivity this is due to the plane wave hitting one detection port then the other in a sequential fashion relying solely on the speed of sound. As the angle is varied from this position, the speed of the wave doesn't change; however, the transverse component velocity of the wave across the sensor will increase reducing

the phase difference until the source is perpendicular to the probe. At which time the transverse component of velocity is infinite, meaning both ports of the probe have the same phase. It is for this reason there exists the null point in the directivity profile and no deflection of the two port diaphragm is recorded.

The other accepted detection method for directional sound measurements in air is the PU method. This method uses a velocity sensor to capture particle velocity data directly, bypassing the need for the finite differential approximation of pressure gradients. The most common velocity sensor used is the microflown flow sensor. [18–20]

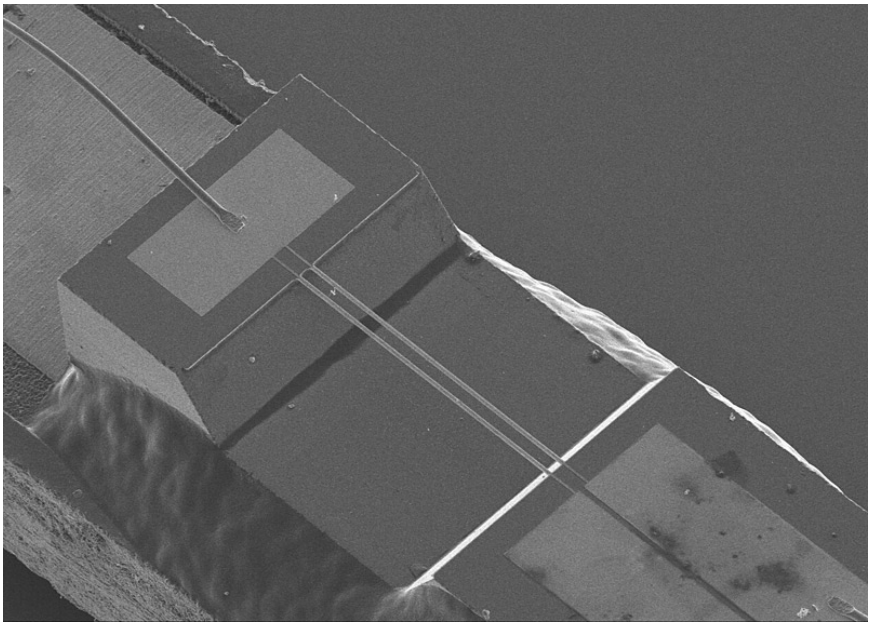

Figure 7: SEM image of a Microflown flow meter [20]

Figure 7 shows a close up image of the sensor. The sensor is composed of two microwires that act as thermo resistors. Any fluid motion across the wires will cause a temperature differential via convection, which in turn is converted into a resistance change between the two wires. The advantage to the microflown is that because of this detection method the forward/backward direction of the velocity can be determined whereas the differential detection can only determine the angle of the incident pressure

wave. The actual PU directional microphone is shown in Figure 8.

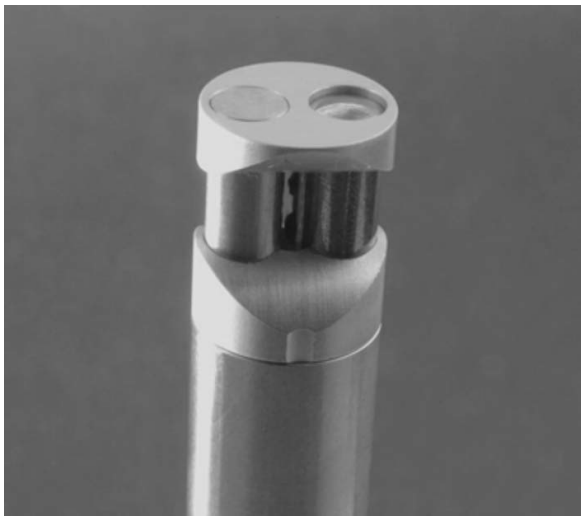

Figure 8: Microflown directional microphone fully packaged [29]

The fully packaged directional microphone contains the microflown wire array shown in Figure 7 in one port. The other port is an omnidirectional microphone to acquire the pressure measurements since for intensity as shown in Equation 14, a time average measurement of $I = \langle u \cdot P \rangle$.

Comparison of the two measurement methods shows that each is preferred for particular situations. This is due to their response to different types of external noise. For the PP method while the pressure differential allows for pressure waves to pass through a measurement surface for power measurement, it will still raise the RMS value recorded by the device. Meaning that while the instrument can detect intensity level from a source in a noisy environment large noise signals will make the device more susceptible to phase error. This is true especially if there exists a phase mismatch between the two sensing microphones, which is the largest issue with this type of directional microphone. Also, as a result of this the PP method shows lower performance at higher frequencies. Furthermore, the requirement to change spacers for each frequency range shows the probe's low bandwidth at each configuration. This shows that these directional microphones can't be micromachined since spacing may

require several millimeters of spacing. The PU probe exhibits more problems in the lower frequency range due to the fact that at lower frequencies the pressure field tends to be more reactive. In terms of calibration the PP method is more advantageous to get rid of any phase mismatch. This is because by reversing the probe the intensity of the signal will change signs but the error will not so any error due to phase mismatch can be cancelled out of the system. The PU probe's mismatch error however cannot do this since when reversed the mismatch error also is reversed so calibration is more tedious.

1.5 Motivation

Current microphone technology as discussed in the previous sections of this chapter each have their advantages and disadvantages to them. Table 1 shows a comparison of the two transduction technques discussed in this chapter for sound measurements.

Table 1: Comparison of microphone sensing techniques

Detection Method	Pros	Cons
Capacitive	• Low cost • Low noise floor • Straightorward design • Linear sensing • Flat frequency response for audible frequency range	• Poor scaling properties • High bias voltages needed • Squeeze film effects leads to membrane stiffening • Limited by snapdown voltage
Optical	• Small sensing area needed • Good scaling properties • High displacement sensitivity • Small air gap leading to lower noise	• Nonlinear sensing • High cost • Difficult to align properly • High power consumption • Device modulation limited to half of the light wavelength used

Since the main objective for the device was to apply the microphone onto a hearing aid, how the device would scale was a critical factor. As Table 1 shows, optical sensing was more advantageous in this regard. This was mainly due to optical sensing not being dependent on the sensing area of the device as much as the capacitive microphone. As a result, using optical detection would be able to minimize a number of tradeoffs associated with scaling, and so was the choosen method for the biomimetic directional optical microphone.

Table 2: Comparison of directional microphone methods

Microphone Type	Pros	Cons
PP method	• Simple design • Easy to calibrate • Uses low noise capacitive microphones • Good sound measurement in noisy enviroments	• Fixed port spacing (not able to scale) • Has difficulty when signal becomes too high frequency • Poor noise floor • Phase matching of the two microphones can be expensive • Needs several devices to span the audible frequency range
PU method	• Measures pressure velocity directly • Scaling limited mostly by the microphone used • Can use a high percision microphone for good pressure measurement • Good sound measurement in noisy enviroments	• Poor noise floor • Can falsely detect air movement as pressure velocity • Poor measurement at low frequencies • Difficult to calibrate

Table 2 lists the pros and cons of two types of directional microphones discussed previously in this chapter. Despite their advantages, neither method is an ideal choice for a directional hearing aid. This is due to their poor ability to scale, large noise floors, and inability to capture the audible frequency range in its entirety without use of multiple devices. Thus the main purpose for this study is to produce a low cost

directional microphone for intensity measurements, improve current design's sensitivity to pressure levels, and widen the device bandwidth for determining pressure intensity. The study introduces a redesigned version of the biomimetic differential microphone from previous work that allows for detection of pressure gradients by manipulating the diaphragm dynamics such that membrane deflection was proportional to the pressure field's gradient. Proof of concept of this detection method has already been shown and the devices have been implemented in working packages for characterization [26, 28, 37, 38]. The new design of the microphone serves to improve its dynamic response, and in addition implements a new optical setup to maintain a high optical efficiency for the device.

In addition to this focus, the overall goal of this thesis was then to incorporate this technology into a hearing aid device. The motivation for which was that directional sensing on such a device will allow for better speech intelligibility for a person in noisy environments. This issue has been a problem for current hearing aids in that most directional microphones that do fit on a hearing aid have poor noise levels and so do not help as much in these setting as they should. As an additional motivation for integrating this device onto a hearing aid it will open up a larger market for the technology in addition to the intensity measurement market. It is for these reasons power optimization of the device is discussed along with performance improvements through active control is discussed for the design.

The following chapter will briefly summarize the design of the biomimetic microphone and discuss the packaging of the device. Chapter 3 will go over characterization of the finished device in terms of acoustic sensitivity, noise levels, optical profiles, and directivity. The following chapter will then discuss the power optimization through pulsing operation of the light source, as well as how this operation will affect the output of the device. Lastly active control of the device will be discussed in being able to control damping values and suppress higher orders of the diaphragm in order

to extend the operation range of the device.

CHAPTER II

BIO-MIMETIC DIRECTIONAL OPTICAL MICROPHONE AND PACKAGING

The goal for this chapter is to introduce the bio inspired optical directional microphone; specifically, its intuitive mechanical design and transduction principle. The chapter will then divulge into the different components for the microphone; describing their specs and how they contribute to the overall microphone design. This will be followed by an overview of the packaging process and finally a proposed design for the integration of the microphone into a hearing aid design.

2.1 The Bio-mimetic Microphone

As mentioned previously the goal for the device was to make a small microphone that would improve speech intelligibility of a hearing aid in a noisy environment. To accomplish this, a directional microphone was necessary to reduce additional noise sources that may be present. The issue then was to come up with a detection method that allows for a microphone less than a couple of millimeters in dimension to detect pressure gradients over a the audible frequency range (20Hz-20kHz). Since as mentioned before in the previous chapter, current directional microphone has limitations that would not work in a hearing aid, so a new detection method needed to be invented to meet with this application's requirements.

The solution to this issue came from a biological study done on a parasitoid fly known as the *Ormia ochracea*. [26, 28, 37, 38] A particular capability that brought a lot of attention to this particular fly is its ability to sense where a sound originates from. Since the fly uses crickets to survive it must be able to detect their symbiotic

partners from a distance via the cricket's mating calls. Usually this would not be a significant discovery since most animals are able to do this simply by having two ears and letting neural connections in the brain create the phase mismatch in pressure fields; however, this fly, as a parasite on a cricket, is very small and so can't use a neural network to detect the pressure difference. In fact if it were to use that method in detecting pressure gradients it would have to process the signal with a time delay of 2 μs, which isn't possible since a typical neuron will fire at an upper threshold rate of 1ms or 1 kHz, and the fly is too small to have enough neurons to fire constantly. The *Ormia ochracea* accomplishes this by being able to transduce the pressure gradient directly, and in doing so can detect sound sources with up to 2 $^\circ$ of accuracy.

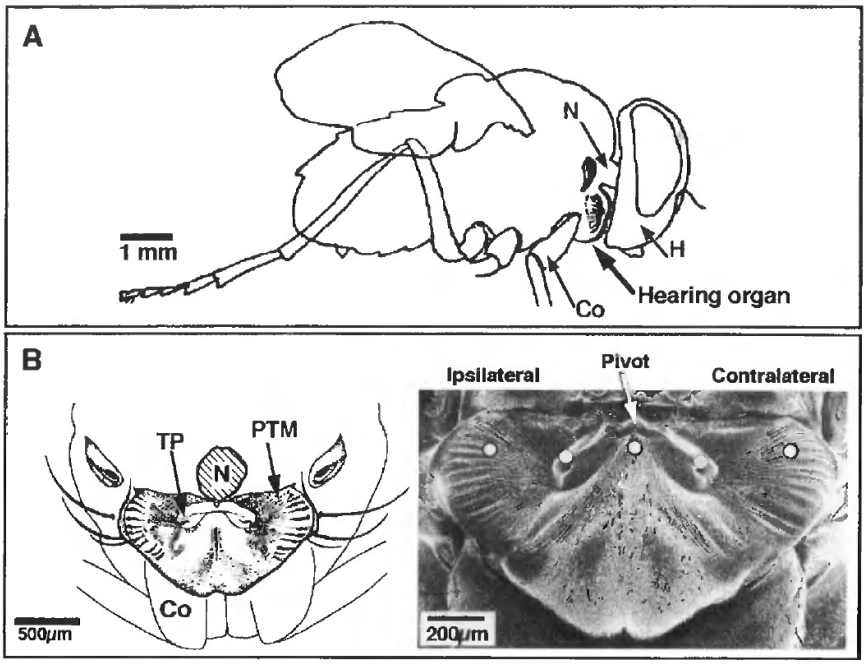

Figure 9: *Ormia Ochracea* with image of its membrane used to sense sound [38]

Figure 9 gives an overview of the fly and its ear anatomy. The unique part of the ear was that its two membranes are coupled by a pivot. This pivot then can detect the phase difference of the two membranes by how much it rotated, because of this pressure gradient can be detected with minimal spacing, a short coming of current

PP probe technology.

The transduction method for the fly is directional since the pressure gradient is measured directly by the membrane. Basically, any pressure gradient across the two membranes will give rise to a see-saw type of motion between the membranes. The pivot as such behaves like a torsional spring and the two membranes apply a moments to it in either direction. The pressure wave and moment felt by the pivot can be related in the following manner. Consider a pressure wave dependent on time and position denoted as P(x,t), with the pivot position at x=0, hitting the ear of the *Ormia ochracea*. The wave excites both membranes on either side of the pivot which results in a force being applied over each area of the fly's ear. Also, for simplicity let both membrane's be square and of equal size. Thus, the moment produced onto the pivot was as follows. [37]

$$M(t) = \int_{-L/2}^{L/2} bxP(x,t)dx \tag{15}$$

Here, L is the length of both membranes together, b is the width of each membrane and x and P were defined above. To make this equation more meaningful the pressure can be broken down into a two part Taylor expansion series. It s assumed that the higher orders in the series are negligible.

$$P(x,t) \approx p(0,t) + x\frac{\delta p}{\delta x}\bigg|_{x=0} \tag{16}$$

Now pressure is approximated by the pressure and the pressure gradient located at the pivot. Combining Equations 15 and 16 gives a moment equation that displaying a relationship to pressure gradient.

$$M(t) \approx \int_{-L/2}^{L/2} bxP(0,t)dx + \int_{-L/2}^{L/2} bx^2 \frac{\delta p}{\delta x}\bigg|_{x=0} dx \tag{17}$$

Taking the integrals of Equation 17 shows that the P(0,t) term zeros out, since both sides of the membrane are symmetric. The other term dependent on the pressure

gradient does not. In fact, the result leads to the gradient being multiplied by the diaphragms area moment of inertia as shown in Equation 18.

$$M(t) \approx \frac{bL^3}{12} \left.\frac{\delta p}{\delta x}\right|_{x=0} = \left.\frac{\delta p}{\delta x}\right|_{x=0} I_A \tag{18}$$

Thus it can be shown by Equation 18 that the rotational force experienced by the pivot was approximately proportional to the pressure gradient. Furthermore, this relationship was not dependent on finite difference approximations like conventional PP probes thus it eliminates the need for a fixed space to determine pressure gradient for a specific frequency band.

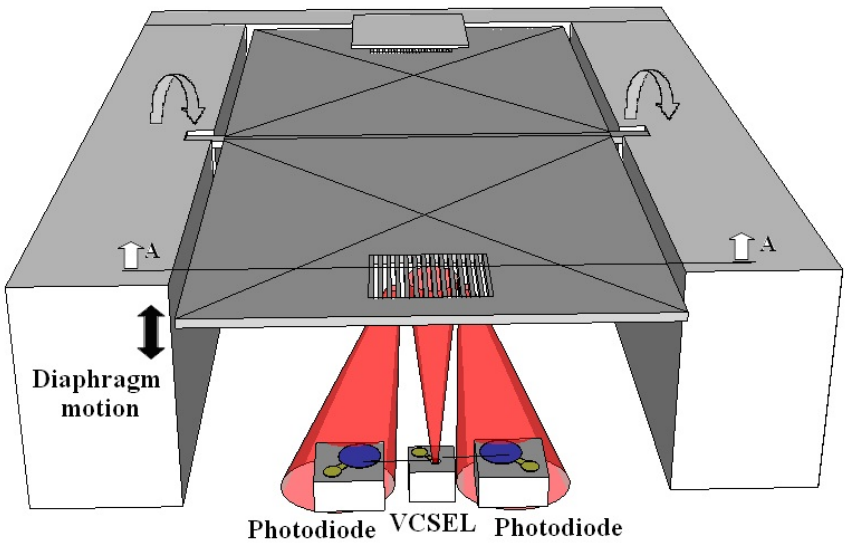

Figure 10: Basic overview of the directional microphone diaphragm [14]

Figure 10 shows an overview of the microphone diaphragm, which was 1x3mm in size and 1-2 μm in thickness. The two membranes of the fly ear are replaced with two thin plates that are attached in the middle to a torsion spring acting like the pivot point. The spring was attached to bulk silicon, which was sealed off to make the device's back side cavity. Also, an important aspect to the design was that unlike the fly which detects the rotational displacement at the pivot point, the diaphragm

detects the rotation of the diaphragm either end of the diaphragm as Figure 10 shows. The detection method is not the only advantage in using this mechanical design.Since the movement of the diaphragm is limited to rotation the backside volume of the microphone remains constant [14]. Thus issues like air stiffening the diaphragm and noise caused by venting the backside cavity are reduced with this design. A more detailed view of the microphone diaphragm is displayed in Figure 11.

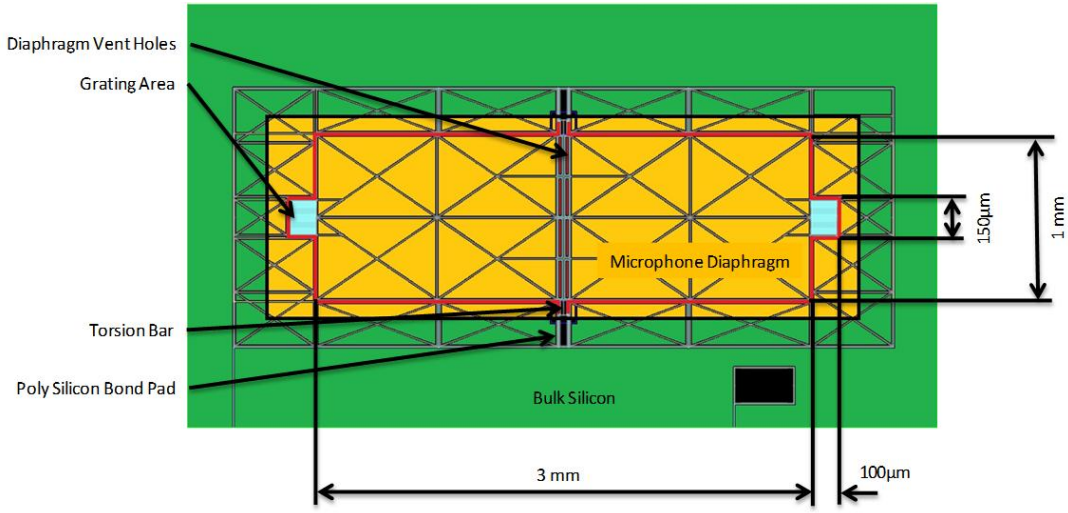

Figure 11: Detailed drawing of the microphone design with diaphragm outlined in red

To transduce the mechanical displacement of the diaphragm into a usable signal a Michelson interferometer as described in section 1.3. This method was chosen over other methods like using capacitive sensing because using an optical transduction method allows for high displacement sensitivity and still acts in a linear sensing region, whereas in capacitive sensing would be nonlinear due to the rotation of the diaphragm. In addition to this using optical detection methods eliminated the need for a large rigid back plate, and so complications due to squeeze film damping were less noticeable.

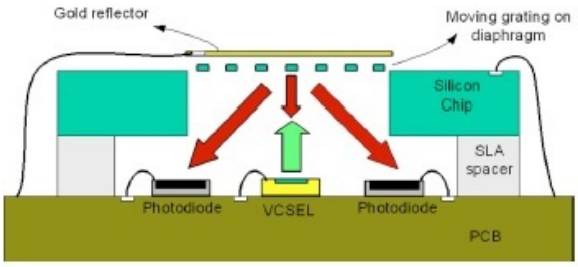

Figure 12: Schematic of Michelson detection method via diffraction grating [26]

The Michelson interferometer has been applied to several MEMS devices via diffraction grating. Figure 12 shows the basic detection setup for the directional microphone. The test surface was the movable diffraction grating while a gold mirror acts as a reference surface. Also shown is the appearance of diffraction orders in this case the device was measuring the 0^{th} and 1^{st} orders of the diffracted light. Ideally the 0^{th} order should be measured since it has the highest intensity, but 1^{st} orders can be used as well. The intensity for each order can be described as follows.

$$I_0 = I_{in} cos^2 \left(\frac{2\pi d}{\lambda_0} \right) \tag{19}$$

$$I_{\pm 1} = \frac{4 I_{in}}{\pi^2} sin^2 \left(\frac{2\pi d}{\lambda_0} \right) \tag{20}$$

The intensity equations shown in Equations 20 and 20 were derived from scalar diffraction theory. An important relation between the orders shows an out of phase relationship, which is a result of the conservation of energy across the intensity profiles; this will be discussed in further detail when differential detection of the microphone is discussed.

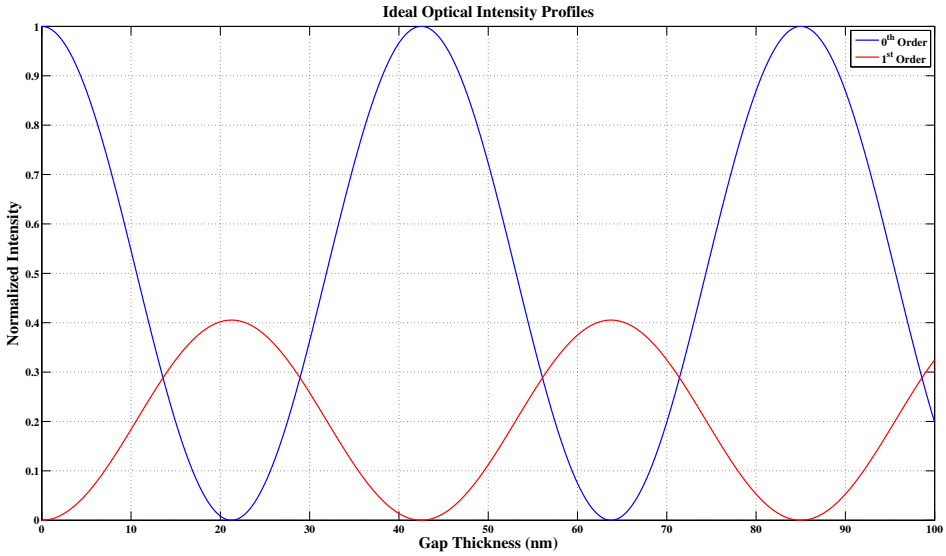

Figure 13: Ideal optical intensity profiles of the 0^{th} and 1^{st} orders

In Figure 13 the normalized intensity profiles are plotted for the 0^{th} and 1^{st} orders over a 100 nm gap change with a 850 nm laser meaning the periodicity of the intensity profile was λ /2. Meaning, every displacement of the diaphragm of $\lambda/4$ goes through one period of the optical intensity profile since the distance traveled for the light source would be twice the gap distance. The profiles are considered ideal because there were no losses or distortions, as will be shown later, there are significant losses due to scattering and divergence that will affect these profiles. It should also be noted that although not shown, there are higher diffraction orders, which was why the addition of the 0^{th} and the two 1^{st} orders will not add up to 1 at every gap thickness.

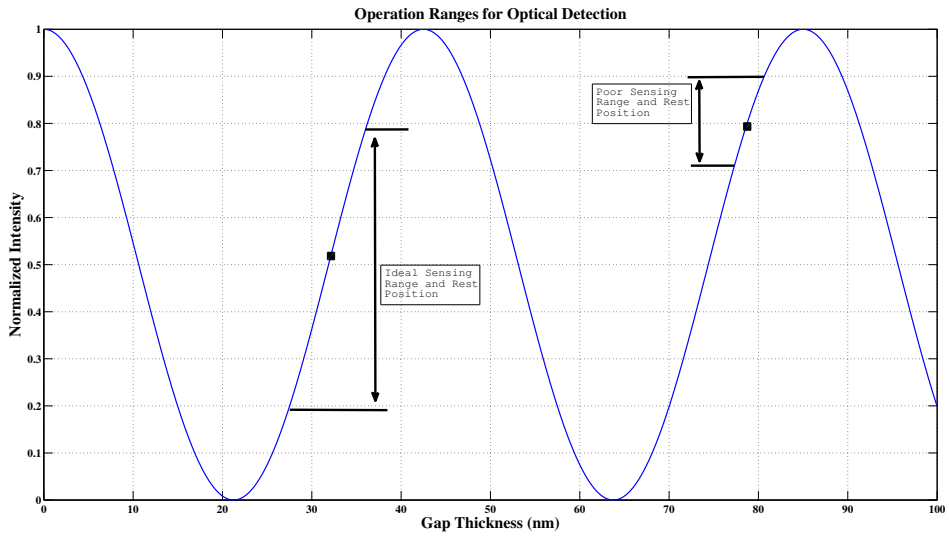

Figure 14: Plot of 0^{th} order intensity profile with operation ranges shown

Figure 14 shows the 0^{th} order and two possible operation points. The first is a good point since it is located on a flat region of the intensity curve and so behaves in a linear fashion. Also, at this point the angle of the profile is steep so a small deflection gives rise to a large swing in the measured intensity. The other point shown in Figure 14 is a poor operation point. This is because when the diaphragm is rested in this position the linear range is reduced by a large amount and the point is very close to a maximum, which means not only will the slope or sensitivity be reduced but unwanted nonlinearities can be introduced by the intensity profile not being linear.

The diffraction orders appear at set angles dependent on the spacing of the diffraction grating. The formula to determine this diffraction angle is shown in Equation 21.

$$\theta_n = \sin^{-1}\left(\frac{n\lambda}{d}\right) \tag{21}$$

Where, n is the diffraction order λ is the wavelength of the light source and d is the distance from the grating the light travels. Using this equation the diaphragm height

from the photodiode sensing plane was determined in order to properly position the optical sensing elements.

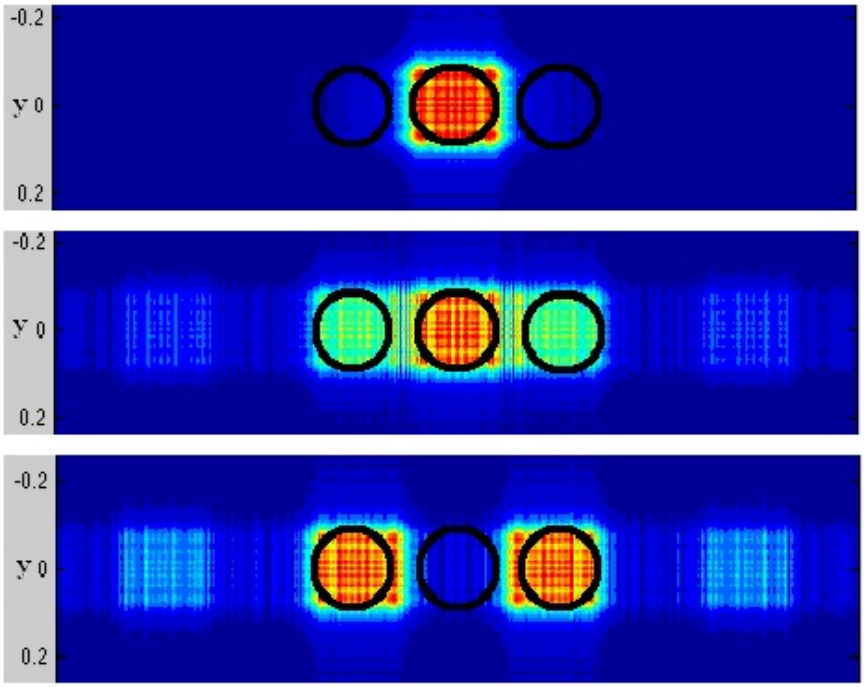

Figure 15: Beam profile of light at photodiode plane at 3 locations of the intensity curve [24]

In Figure 15 there are several images of the optical profiles for a light source at multiple points in the intensity profile. The top image shows when gap distance is at a point where the gap for the diaphragm is $m\lambda/2$ where m is any non negative integer. The bottom image is a point where the gap is $(2m+1)\lambda/4$, with m also a non negative integer. The center image is a point where the gap is in between the other two images so there is some intensity located in both orders.

As a final step to the transduction process for the microphone the light intensities are converted into electrical signals using photodiodes. These produce a current dependent on the intensity detected and are run into a trans impedance amplifier (TIA) to place a gain on the output and convert the current signal into a voltage output.

2.2 Bio-mimetic Microphone Components and Packaging

This section addresses the specific components and setups involved in packaging of the biomimetic microphone diaphragm and their key design features. This section also describes the packaging process and issues that can occur during its creation.

Some of the main challenges encountered when creating the microphone package was to first implement the device with the previous test setups. This involved having the device interface with a preexisting preamplifier tube, requiring the package to be mounted on a 12 pin header with a custom designed PCB to route the component signals to their respective pins. The package also needed to implement a lens array to improve the device's optical efficiency that required specific spacing from optical surfaces (e.g. VCSEL active area, photo-sensing planes, diffraction grating). The solution to this was to design and fabricate precision machined spacers with small thickness tolerances. Also, implementation of the lens array involved fine tuned alignment of the optical components, which was addressed by using a commercial pick and place setup. The last main packaging challenge was to correctly position the microphone diaphragm on a sensitive area of the diffraction grating. This was achieved with a custom placement setup and an active alignment process. All of these packaging challenge solutions are discussed in further detail throughout this section.

The order in which the individual components of the package are introduced in this section is in a bottom up fashion for the device. This is then followed with a discussion of the several setups used for packaging. Finally the section addresses the process flow for packaging of the directional optical microphone.

The packaging design was based off of previous work [26, 28, 37, 38], which implemented a similar biomimetic diaphragm. As mentioned previously, the packaging required the device to interface with a 12 pin preamplifier tuhe preamplifier tube for the package be that had a 8x8 mm area for the device. Figure 16 shows an exploded view of the packaging layout for the microphone diaphragm. The preamplifier tube

for the package to interface with is described in detail in Appendix A.

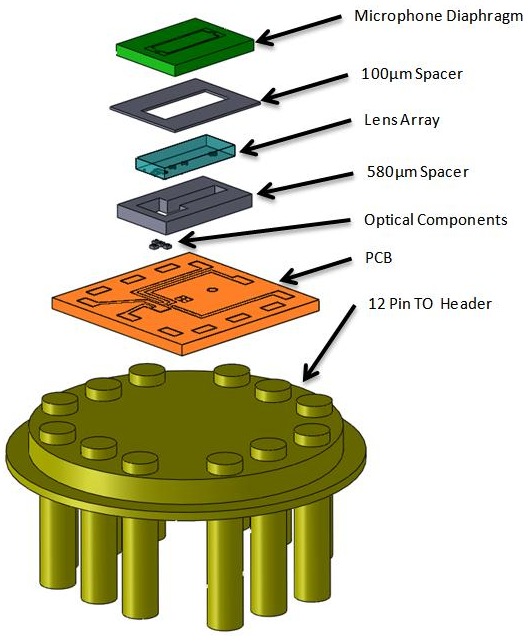

Figure 16: Exploded view of microphone package

The first component for packaging was the PCB used to route all of the electrical signals to and from the device. The PCB was created to fit in an 8 x 8 mm area so the completed device could be mounted on a 12 pin TO Header. The main design goal for the PCB was to route signals to and from the optical devices without interfering with the devices housing. Another aspect of the routing PCB was that it acts as a intermediary step for wire bonding. The reason why this was necessary was that the machine used for wire bonding does not have the vertical range to make a bond from the microphone diaphragm to the TO header. Thus a 1x0.5 mm pad was created for each pin to act as a intermediate bonding area to the TO header. The designed PCB overlaid on a TO header is shown in Figure 17 with Pin allocations shown in the preceding Table.

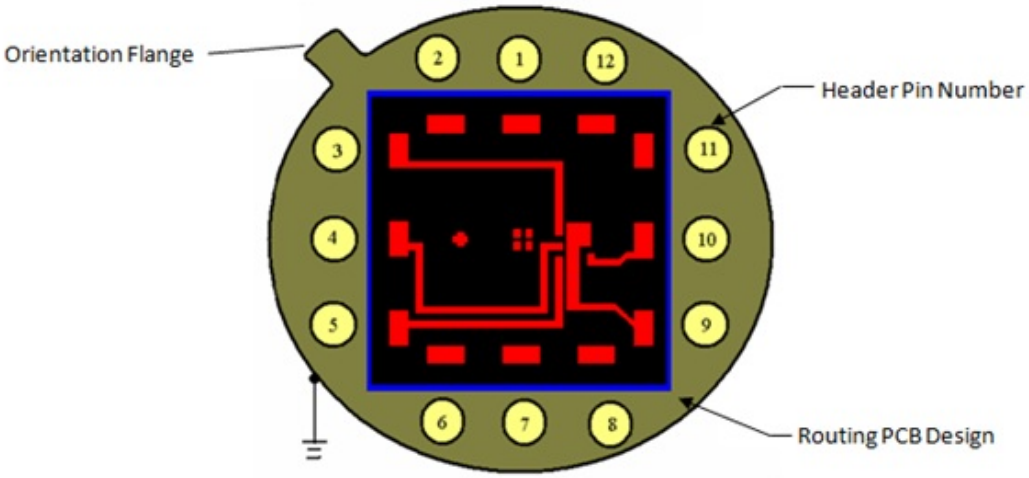

Figure 17: Routing PCB on a TO header with pin numbering

Table 3: TO header pin allocations

Pin Number	Description
1	N/A
2	Photodiode Output
3	Photodiode Output ($+1^{st}$)
4	Photodiode Output (0^{th})
5	Photodiode Output (-1^{st})
6	N/A
7	N/A ($V_{cc}+$)
8	Electrostatic Supply
9	Common Ground
10	VCSEL Power Supply
11	N/A ($V_{cc}-$)
12	Electrostatic Supply

Pins allocated N/A indicate that the pin was left floating; pins 7 and 11 are also

floating on the TO header but are assigned to be the supply voltage pins for the TIAs in the IO map. Pin 9 was where the optical elements are grounded to. Since the optical elements have grounding surfaces on the backside of the elements, the large area connected to the bond pad for pin 9 was for the placement of the optical elements. Pins 3,4, and 5 as shown in Table 3 are used to route the 3 photo diodes current outputs. The long areas connected to their bonding pads on the PCB are used to move the signal under the devices housing. Pin 10 also has a small area attached to its bond pad, like the previous areas discussed this serves to route the VCSELs power supply under the housing and to the VCSEL. The plus and 4 square geometry in the center of the PCB are to act as alignment features for the devices lens array.

The coherent source used for the device was a Vertical-cavity surface emitting laser (VCSEL) that is normally used for telecommunications. The component used for the microphone device was an 850 nm single mode VCSEL. The VCSEL vendor was Lasermate Group Inc. model number VCC-85AIG-IS. Chip size for the VCSEL was 270x270 μm with a 5-10 μm emitting area. The optical power for the VCSEL was rated for 2mW Gaussian beam with an operation voltage of 2.5V. The beam divergence for the device was listed as 8 deg ($1/e^2$ radius). The VCSEL device since used for data communications has the ability to be pulsed upwards of 3 GHz.

The photo sensing components chosen for the device was a GaAs photodiode for sensing 850 nm light. The parts were purchased from ULM photonic part number ULMPIN-04-TN-U0101U. The active area of the photodiode was 100 μm and had a responsively of 0.5 A/W. The size of the photodiode was 250 μm. Like the VCSEL element chosen the photodiode was for data communications and so was capable of detecting signals up to 4.25 GHz.

In order to get the correct spacing for the diaphragm to photodiode sensing plane, two spacers needed to be designed with tight tolerances. The first of which was a 580 μm spacer that was used to space a lens array that will be discussed later.

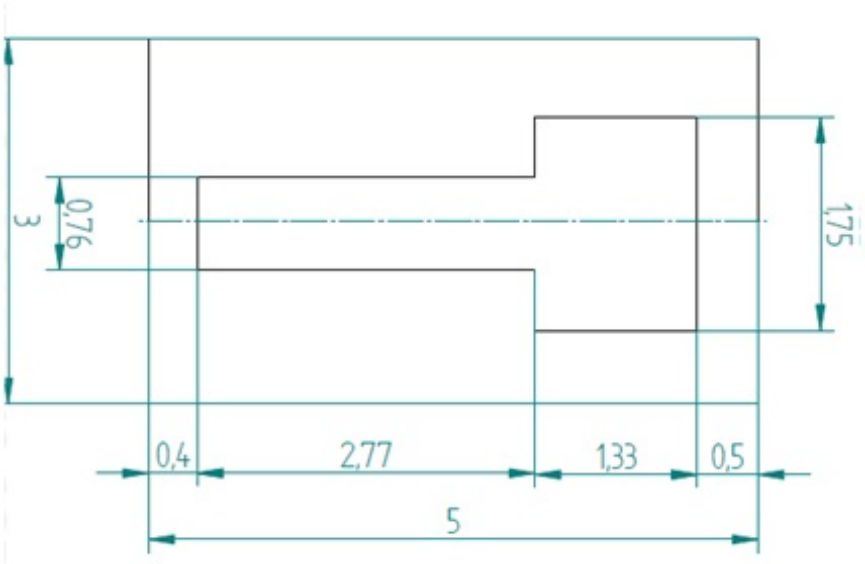

Figure 18: Drawing of 580 μm spacer with dimensions shown in mm

The stainless steel spacer has a thickness tolerance of 7 μm. The inner radii, although not shown in Figure 18 are approximately 0.45 mm this was due to the machining process for the part. The inside geometry was chosen to be a T-shape in order to reduce the cavity caused by the spacer while still allowing the alignment marks and optical elements to be viewed from above. Since the part was made out of stainless steel the spacer were coated with 3 μm of paralene this allowed the spacer to be insulated from the routing segments of the PCB.

One of the most critical components of the device was the lens array due to its tight tolerances this element dictated the dimensions of other components in the package e.g. the 580 μm spacer. The lens array was made out of 500 μm thick non reflective quartz. The optical profile of the design is shown in Figure 19

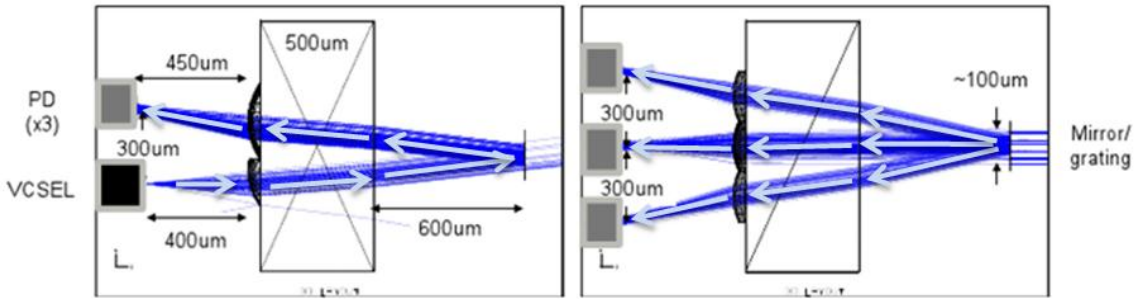

Figure 19: Optical beam pattern simulation of the lens array conducted by JenOptik [46]

The main design objective for this element was to improve the optical efficiency of the device, which was shown to be less than 1% efficient without any focusing element. This was mainly due to the divergence of the source along with other losses such as scattering of the light. In order to accomplish this task the lens had to first columnate the VCSEL light into a 30x40 μm beam and steer the beam at an angle to the diaphragms mirror 600 μm away. Then the lens would have to collect the diffracted light from the mirror and direct it into the three photodiodes for optical detection. The design for the lens was carried out by JenOptik and was to improve optical efficiency to around 50%.

Analysis of the tolerances for the lens were also given by JenOptik , which were as follows: with grating (Y direction) 0-10 μm shift, across grating (X direction) 10μm shift, height (Z direction) 25 μm shift. When these tolerances were not met the optical efficiency of the lenses would quickly drop to 20% optical efficiency [46]. The tolerances given are mostly dependent on VCSEL placement to the lens array. Despite this strict tolerance of the VCSEL to the lens array, placement tolerances for other components of the microphone package were increased. This was due to the reduced spotsize of the VCSEL light relative to the other package components. In particular, the 40 μm diameter spotsize had about a 30μm tolerance on the diffraction grating. The photodiodes, due to their large sensing area (100μm diameter), had

looser tolerances on placement as well, allowing for 30μm of shift from the device's optimal point.

In order for the beam to be steered correctly to the diffraction grating and back to the photo diodes it was important to have correct spacing from the lens surface to the mirror surface. This was done with the 100μm spacer. Due to the design of the lens, spacing from the back side of the lens to the diffraction grating needed to be 600 μm. Since the backside cavity of the diaphragm was 500 μm a 100 μm spacer needed to be fabricated in order to meet the design specifications for the lens array.

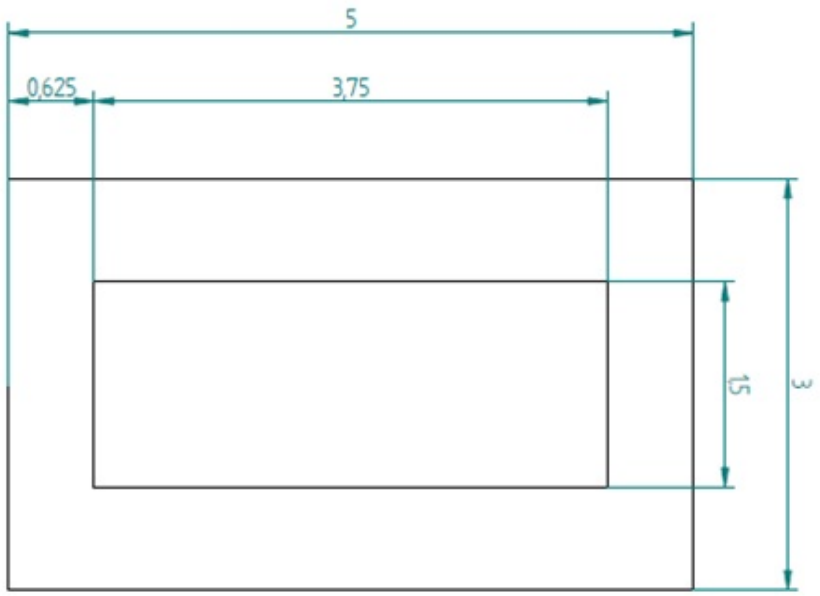

Figure 20: Drawing of 100 μm spacer with dimensions shown in mm

The stainless steel spacer designed was made out of the same material as the 580 μm spacer with the same thickness tolerance of 7 μm. The inside radii for the spacer was 0.2 mm. Since this spacer was placed between the lens array and the microphone diaphragm bulk material no insulation layer was applied to the spacer.

The design of the diaphragm was described in the first section of the chapter along with its detection scheme. The microphone diaphragms were all 4.6x2 mm (Outer Dimension) with a backside volume of 2.214mm^3. Located on the diaphragm there

are 3 areas for wire bonding. Two large gold mirrors that act as both reflecting surfaces and bonding areas for electrostatic actuation, and a 50 x100 μm polysilicon area in order to ground the moving diaphragm.

For packaging of the bio mimetic microphone optical components for the device require tight placement tolerances to help increase optical sensing efficiency. To aid with the optical placements the packaging process utilized a pick and place machine, which would help with the accuracy and repeatability of placing the optical components onto the PCB routing board. The pick and place machine currently being used in the packaging process was the FinePlacer Pico Ma designed by Fine Tech. This placer allows for fine tuned placement of a chip onto a substrate with up to 5 μm accuracy in X, Y and rotation (R) directions. In addition to this, the machine can apply a controlled force to the device being placed as well as apply heating to the substrate for Epoxy curing. Figure 21 shows an image of the same FinePlacer being used provided from Fine Tech's website.

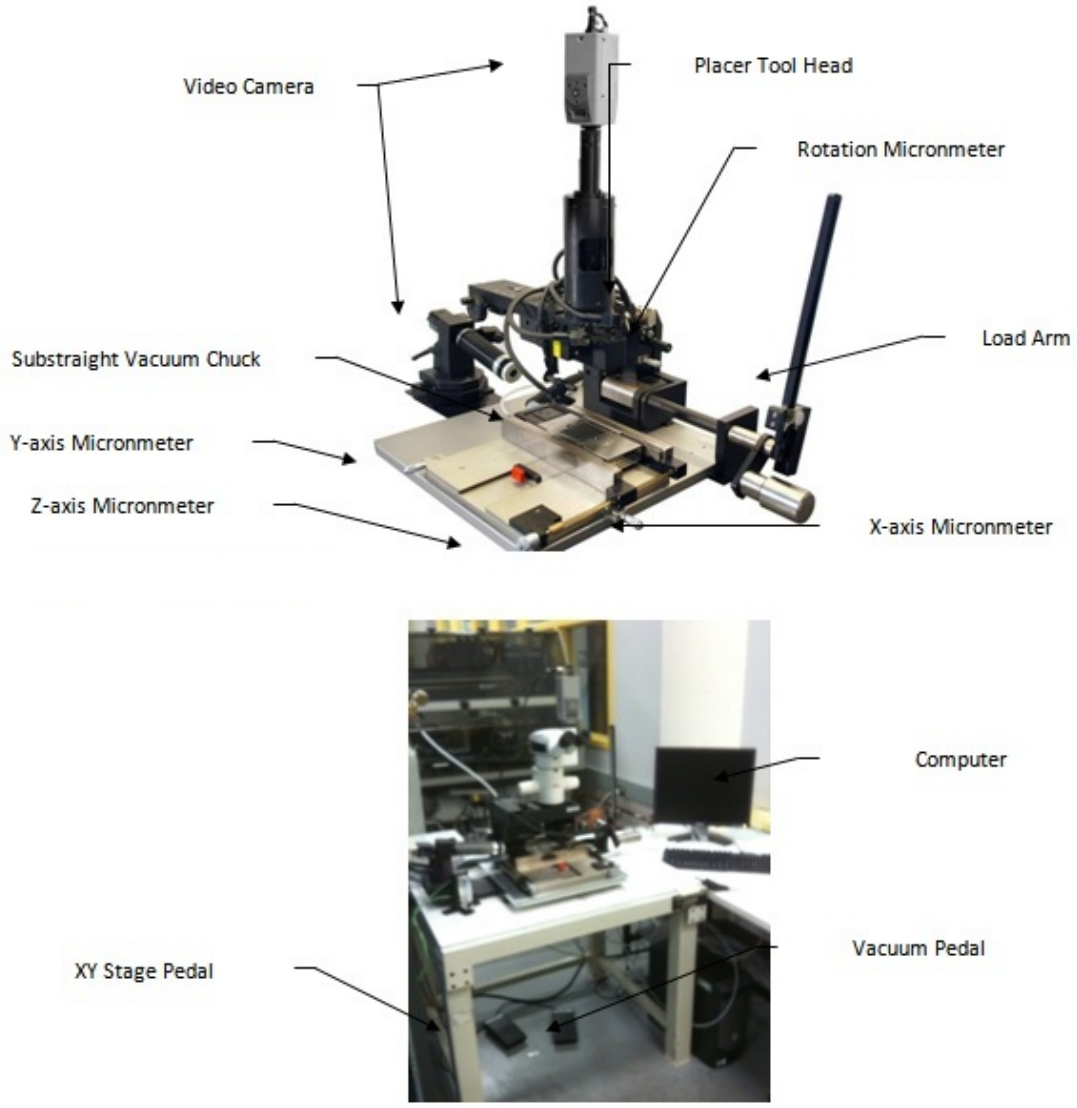

Figure 21: Image ofPackaging Research Center pick and place setup

The tool head used to place the optical components is shown in Figure 22. The tip of the tool head has an inverted pyramid design, this was to prevent the tool head from damaging the device features i.e. the photo sensing and photo emitting areas on the devices top face. This design also allows for the same tool head to be used on both the VCSEL and Photodiode devices that have slightly varying geometries. Some disadvantages to using this tool head was that the bottom of the device was used for alignment, which reduces accuracy, and excess epoxy sometimes clogged the

tool head. However, designing around these issues would result in a much pricier tool head roughly ten times more expensive.

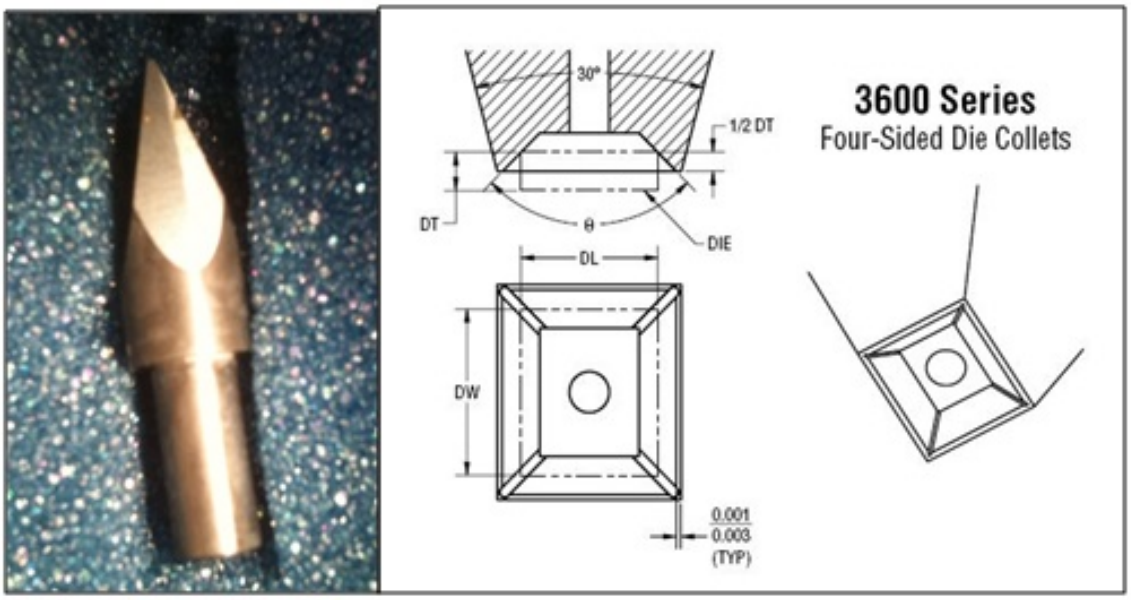

Figure 22: Tool head shown and the design of the inverted pyramid from Gaisers catalogue [2]

Another important setup was the alignment of the microphone diaphragm, which needed to be placed with similar accuracy as the optical elements were placed. To accomplish this, a placement setup that would allow for handling of the microphone diaphragm was constructed. Figure 23 is an image of the diaphragm placement setup. The setup places the microphone testing equipment that includes the IO box, preamp, and connector cable under a CCD camera. This allows for the microphone diaphragm to be aligned with the same electronics that was used to characterize the system offering more consistency to the process. A CCD camera attached to a microscope was required to view the light being emitted from the VCSEL since it can be harmful to eyes if looked directly upon. The preamp was secured to the microscope's stage with a rotation stage, which allows for more flexibility with the diaphragm placement. The diaphragm was picked up by a set of adjustable tweezers

attached to an XYZ stage that allowed for accurate placement. Finally a function generator was present to produce a sound signal with a speaker allowing for active alignment of the diaphragm using an oscilloscope.

Figure 23: Image of diaphragm placement setup

2.3 Packaging Procedure for the Bio-mimetic Microphone

The packaging started with preparing the routing PCB, displayed in Figure 24, this usually involved a QC inspection and the polishing of bonding surfaces to improve the success rate of the wire bonder (a micro ultrasonic welder).

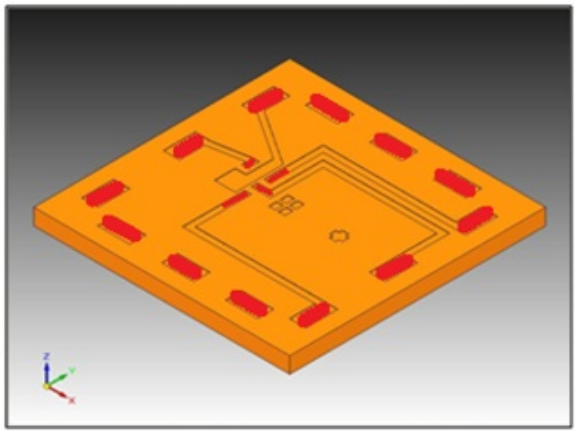

Figure 24: Schematic of PCB board with polished areas in red (bonding areas)

The VCSEL and 3 photo diode elements were aligned and placed with the Fine-Placer Pico Ma such that the elements were aligned in a 300 μm grid shown in Figure 25.

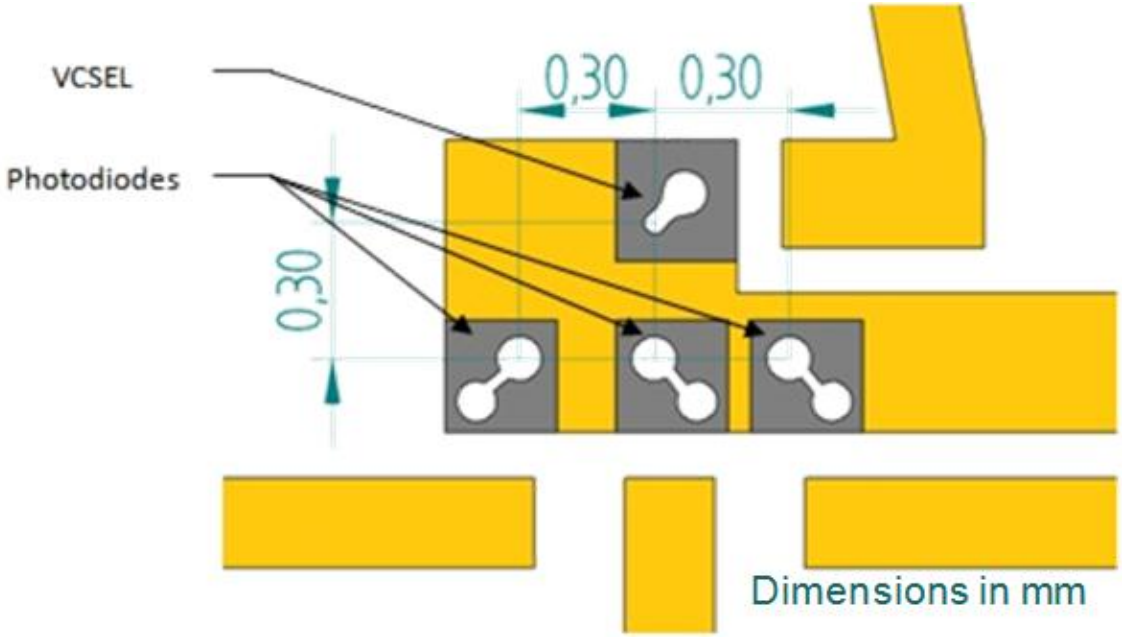

Figure 25: Schematic of optical element spacing for lens array on PCB

The orientation of the components had to be chosen such that bonding of the elements would not interfere with the optical path. Also, leaving enough room for

the pick and place tool head's perimeter, which would create a vacuum seal, played a role in the orientation of the components. The type of epoxy used to secure the devices and ground them electrically to the PCB board was a conductive thermal epoxy; specifically, STAYSTIK 141.

The FinePlacer Pico Ma aligned the optical components with a 0.5 N force to ensure that the surfaces were flat on the PCB. The VCSEL was placed first on the PCB board since the other components needed to be aligned with respect to this element. The alignment of the VCSEL to the PCB is displayed in Figure 26, where the VCSEL edges were placed flush to the edges of the ground pad area on the PCB.

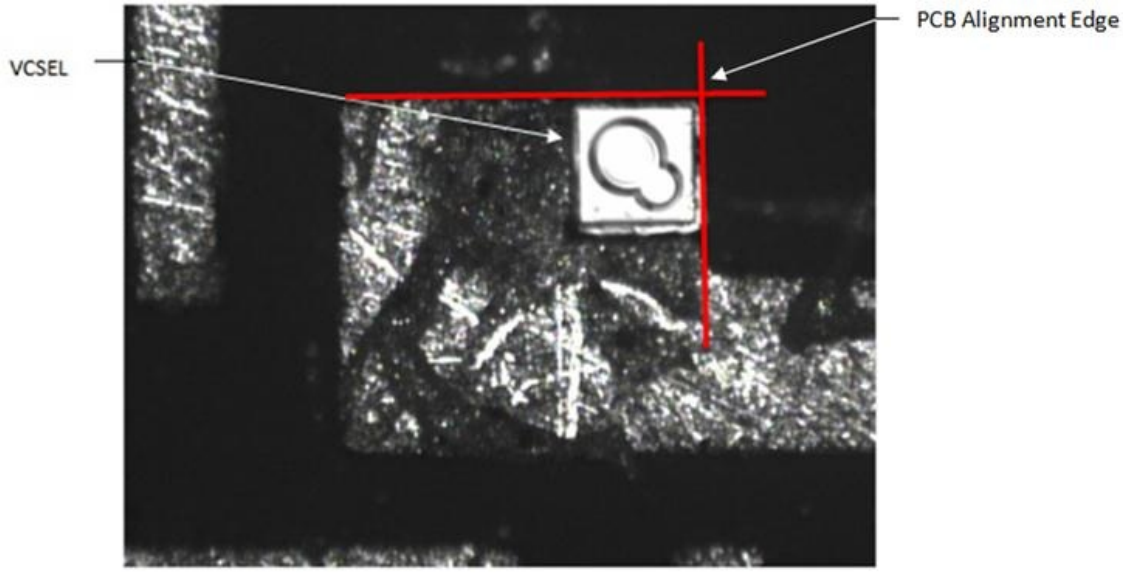

Figure 26: Image of VCSEL aligned on PCB top view of placed element

Once the VCSEL was placed then the other optical components i.e. the photodiodes could be placed with their 300 μm periodicity. Each had the center of their active areas aligned to the VCSEL's 5 μm diameter active area and then moved to their respective positions. Figure 27 shows the end result of the placement.

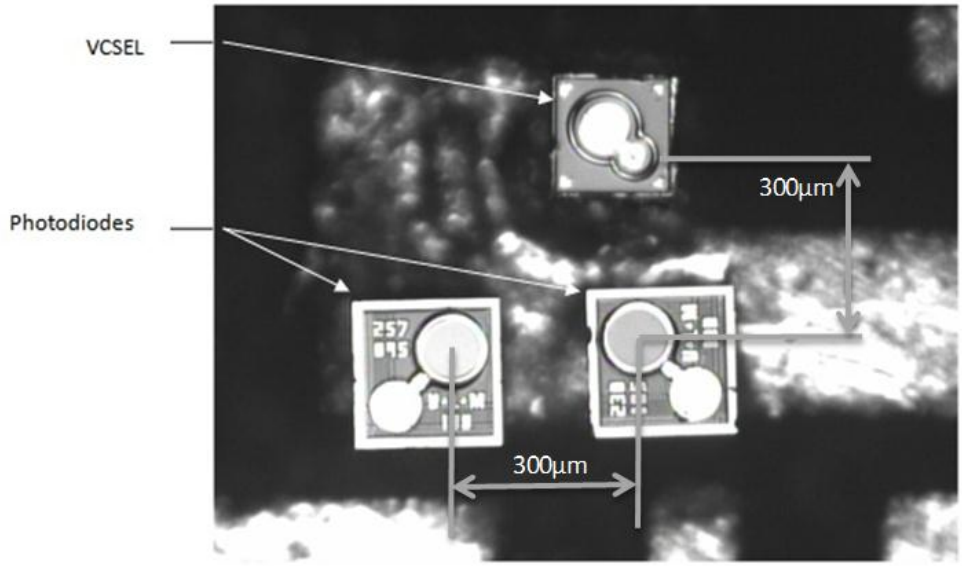

Figure 27: Photodiode placement on PCB with the FinePlacer Pico Ma

Since the Tool Head used had an inverted pyramid design as shown in Figure 22 only 2 photodiodes were placed using the FinePlacer Pico Ma as shown in Figure 27. The last photo diode was placed by hand under a stereo microscope. To ensure that the device was flat on the PCB a glass slide was used to align the last photodiode on the same plane as the others.

Once all the optical elements were aligned properly each element was wirebonded to their respective bonding areas, after which electrical connections and inspection of the elements were made. Figure 28 shows the wirebonds on the PCB as well as a CCD image of the finished components.

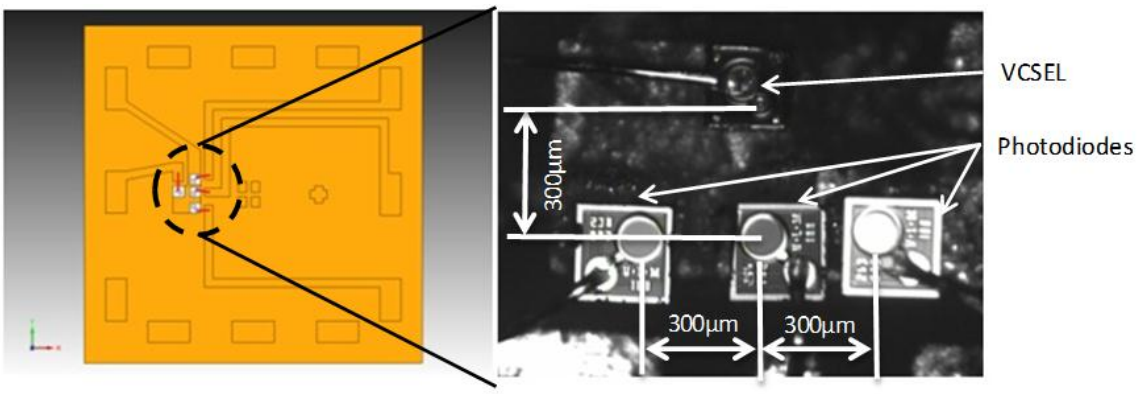

Figure 28: Packaged optical components: wire bonding schematic with conections in red (Left),a CCD image of a completed setup (Right)

Once the optical elements were properly placed and inspected for functionality the 580 μm spacer was then placed onto the PCB. The alignment of the spacer was done by hand and was aligned as shown in Figure 29. UV light cured epoxy was used to seal the spacer to the PCB and to make sure it would not move during the rest of the packaging process. The spacer after it had been fixed with epoxy was then tested to make sure it did not create a short circuit with any of the routing paths on the PCB.

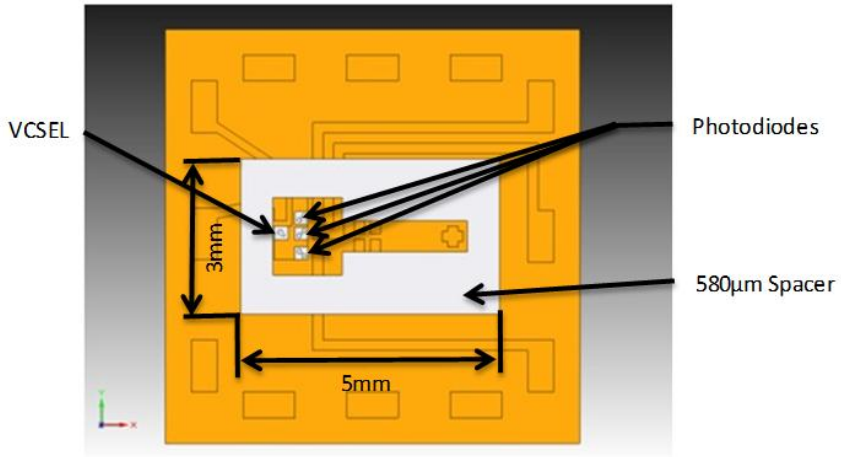

Figure 29: 580 μm spacer placement and orientation on PCB

With the spacer in place the lens array could be aligned to the package. Figure

30 shows the spacing of the lens array as well as the photodiodes' and VCSEL's alignment to them. Due to the tight tolerances as mentioned above in the discussion of the lens design the FinePlacer Pico Ma was employed to do this task.

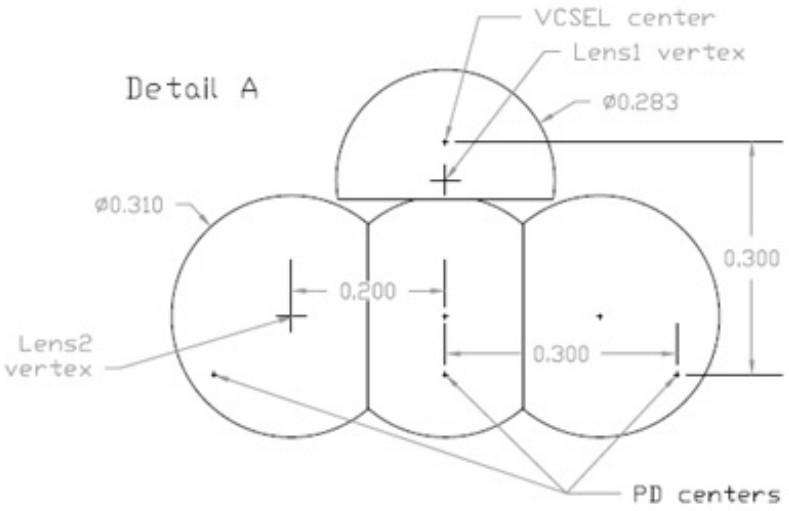

Figure 30: Alignment of optical elements on lens array [40]

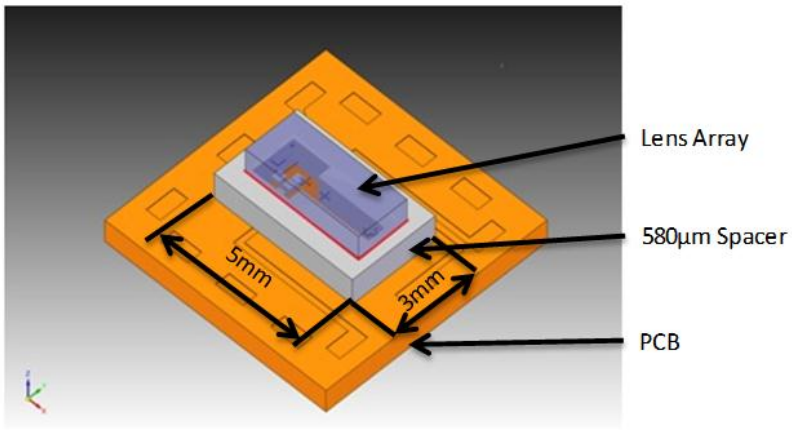

Figure 31: 580 μm spacer with lens array placed

Figure 31 is a schematic of the placed lens array element with UV epoxy seal to the 580 μm spacer. With the lens array positioned onto the package with proper spacing, the PCB was placed onto a TO header and wirebonded and the optical alignment was checked to make sure the light was correctly captured by the lens array.

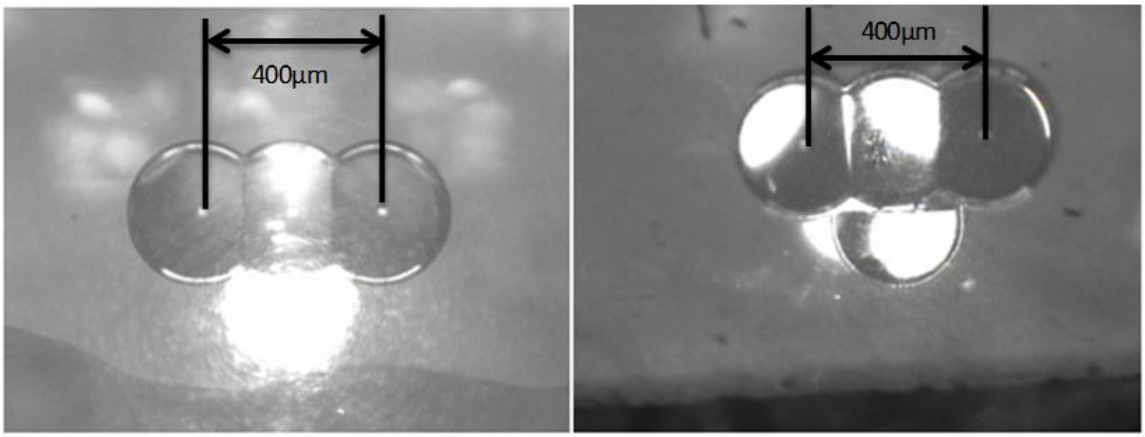

Figure 32: Alignment of lens array: an aligned lens array (Left), a misaligned lens array (Right)

Figure 32 shows on the left a device with a properly aligned lens array, whereas the right image is a misaligned element which misplaces the VCSEL light. The main objective for the 100 μm spacer alignment was to place the spacers such that a full seal could be applied around the spacer and lens array while not blocking the optical path of the device. The piece was assembled by hand on top of the lens array. Epoxy was applied to the corners of the spacer in order to hold it in place until a full seal was applied. Figure 33 shows the orientation and placement of the 100 μm spacer.

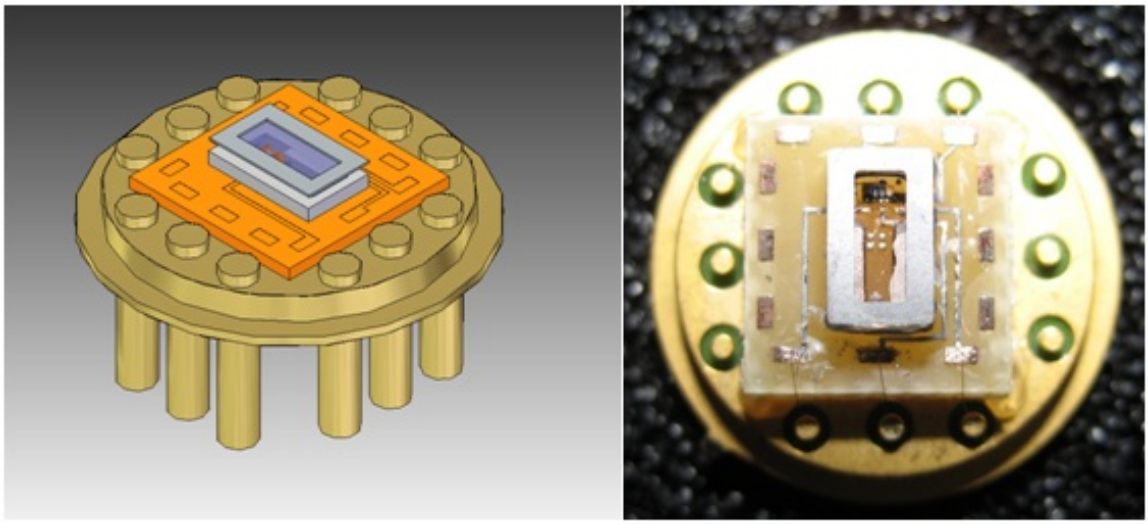

Figure 33: Package with 100 μm spacer attached:a trimetric view schematic (Left), an image of a device (Right)

After alignment the four corners with epoxy are cured to secure the spacer in place. Then more UV light cured epoxy was applied and cured between the 580 and 100 μm spacer to form a full seal around the lens array. Figure 34 shows a cross sectioned view of the device with red indicating the region that was filled with epoxy.

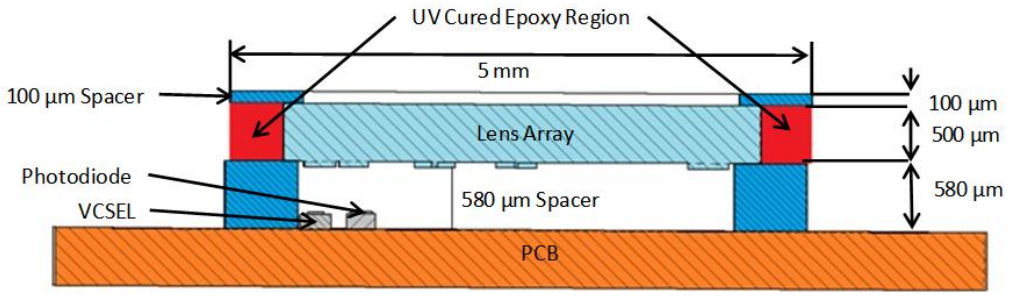

Figure 34: Cross section view of device with epoxy filled region labeled

Once the 100 μm spacer was secured to the package the diaphragm was aligned to the package. The setup described in the previous section was used to align the microphone diaphragm after placement of the 100 μm spacer. The diaphragm was placed into the XYZ stage and was adjusted until the VCSEL light was aligned with

the reflective gold mirror at a proper height (a couple μm above the 100 μm spacer) and rotation. From this position a sound source was applied to the system making the diaphragm vibrate. Each of the order outputs were monitored with an oscilloscope the diaphragm was then adjusted in the horizontal plane until acceptable outputs were found. A properly aligned diaphragm is shown in Figure 35.

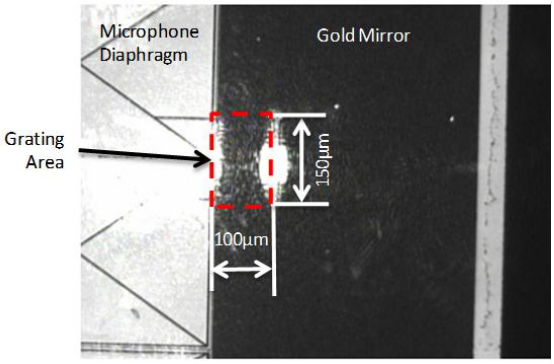

Figure 35: Light on mirror during alignment (device w754-1505)

Once the diaphragm was in an acceptable position the diaphragm was fixed using UV cured epoxy. Additionally, a layer of epoxy was used to act as shielding for the wires that would be attached to the diaphragm for electrostatic alignment. Figure 36 shows a cross section view of the completed package with epoxy regions indicated in red.

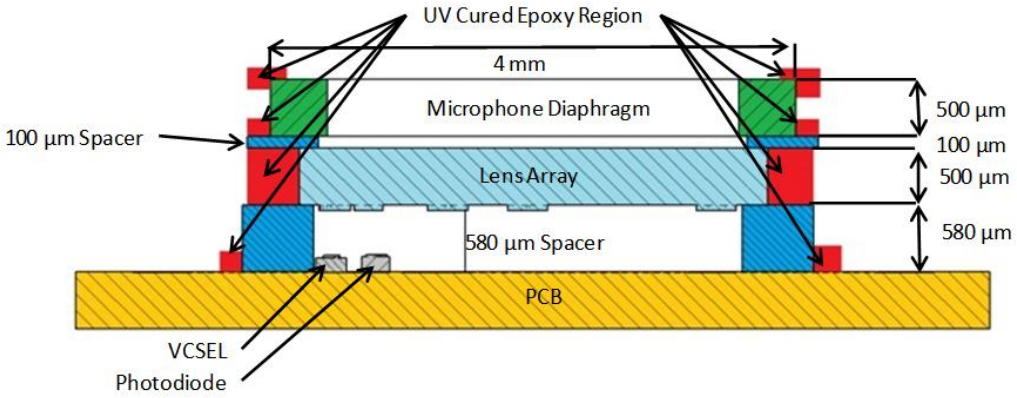

Figure 36: Cross-section view of device with epoxy regions highlighted in red

With the diaphragm fully attached, the device can be used for acoustic sensing; however, since electrostatic biasing was used to position the diaphragm to an optimal sensing point, electrical connections were made to the diaphragm as a final step. The electrostatic ports would also serve to apply feedback to the device, which was shown in a later chapter. The two gold mirrors on the diaphragm would be supplied the electrostatic voltages, while the diaphragm was grounded.

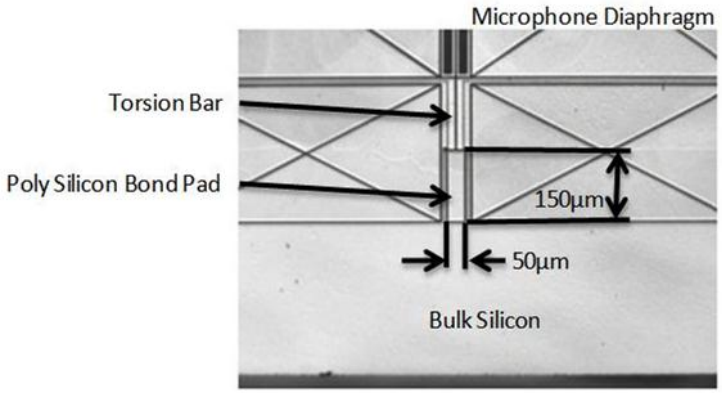

Figure 37: Image of polysilicon bond pad on diaphragm

The bulk silicon and 10 μm oxide layer act as a shielding in addition to the epoxy layer applied to the diaphragms edge. Figure 38 shows the finished package with electrostatic actuation with a schematic of all the wirebonds present on the package exterior.

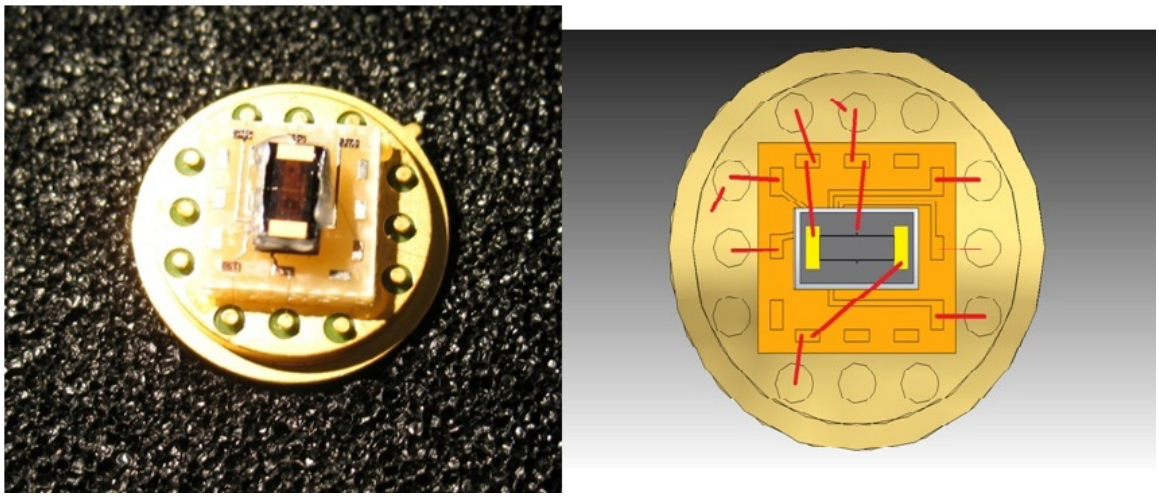

Figure 38: Finished microphone package: image of device (Left), schematic of wire-bonds on package (Right)

2.4 Integration of the package into a BTE Hearing Aid

One of the main objectives for the bio inspired directional optical microphone was that it would be integrated with a hearing aid in order to improve speech audibility in noisy surroundings. For proof of concept, a SLA BTE hearing aid was designed so a directional hearing aid could be mounted to it and used in the field. Figure 39 shows the current commercial design for reference.

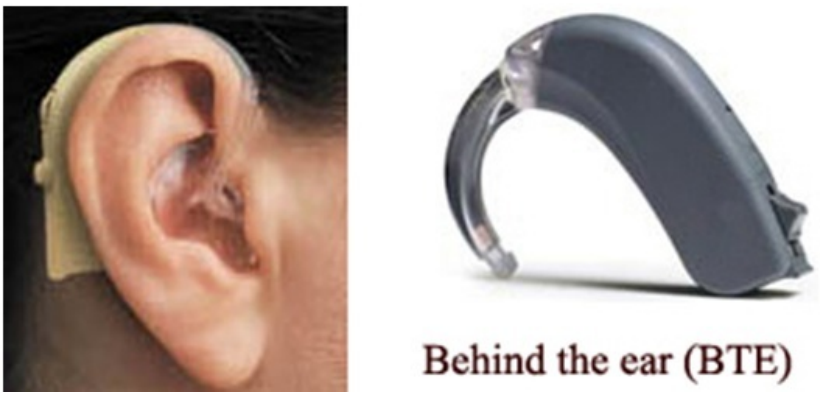

Figure 39: Commercial BTE hearing aid [1, 50]

Figure 40 was the proposed SLA design for the directional microphone developed

by SUNY Binghamton.

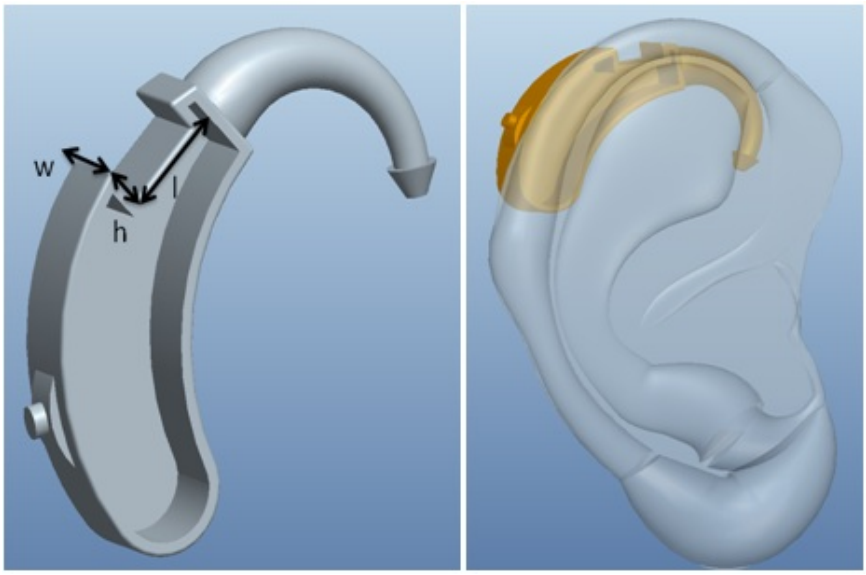

Figure 40: 3D model of SUNY Binghamton BTE hearing aid design [22]

As seen in Figure 40, the design was meant to be placed at the top of the ear such that the microphone is parallel with the ground when the person is standing upright. This basic design was then used as a guide to make a PCB for this hearing aid.

The PCB was designed with a few key features in mind. The first was to serve as a routing and alignment board like in previous designs so that it would connect to an IO preamp tube via coaxial cables. This would entail creating several bonding areas for wire bonding and nodes to connect the coaxial cables. Another design consideration was to make the package narrow making the width (w in Figure 40) of the SLA at most 6mm. The final design consideration was to create a socket in the SLA design such that the completed PCB microphone package would act as a cartridge for the hearing aid, allowing for greater ease when replacing a microphone diaphragm. A schematic of a packaged microphone cartridge is shown in Figure 41.

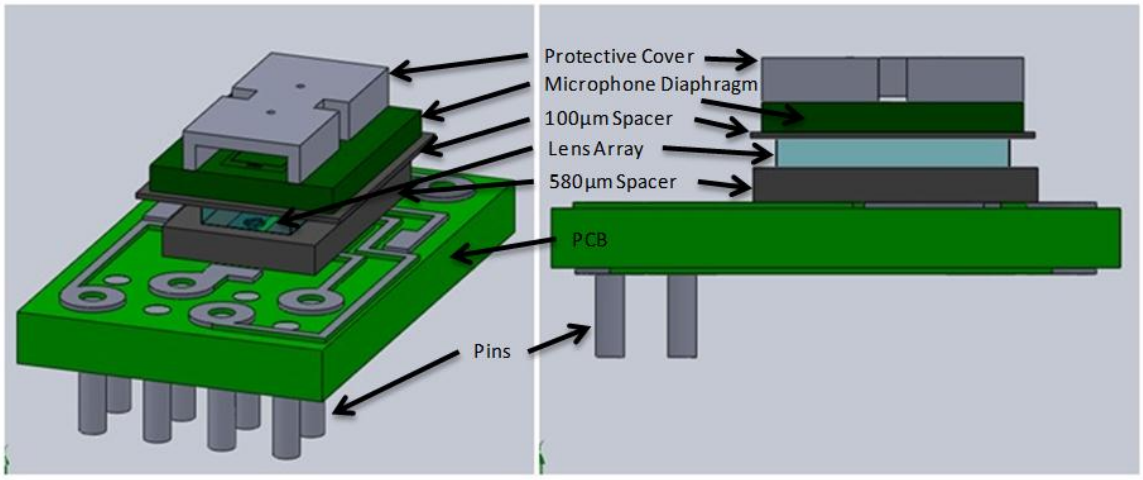

Figure 41: Schematic of microphone cartridge for BTE design

The microphone cartridge is shown in Figure 41 on top of the diaphragm was a protective cover designed by SUNY Binghamton that serves to protect the diaphragm from breaking while being used.

The PCB design covers a 6 x 10 mm area with 8 pin connections. The pins are in a 2x4 array with 1.27mm pitch in both x and y directions. This periodicity was chosen so the pins would fit into a standard 8 pin dip connector.

The pins shown in Figure 41 are planned to be soldered to the PCB. This was an initial step before any other packaging was done to ensure that other parts of the package were not damaged during the soldering process. This added step then requires the PCB to have a temporary holder in order to hold the PCB for other packaging processes such as pick and place and wire bonding. The added height should not be an issue to these steps as the movement stages can be adjusted by several millimeters.

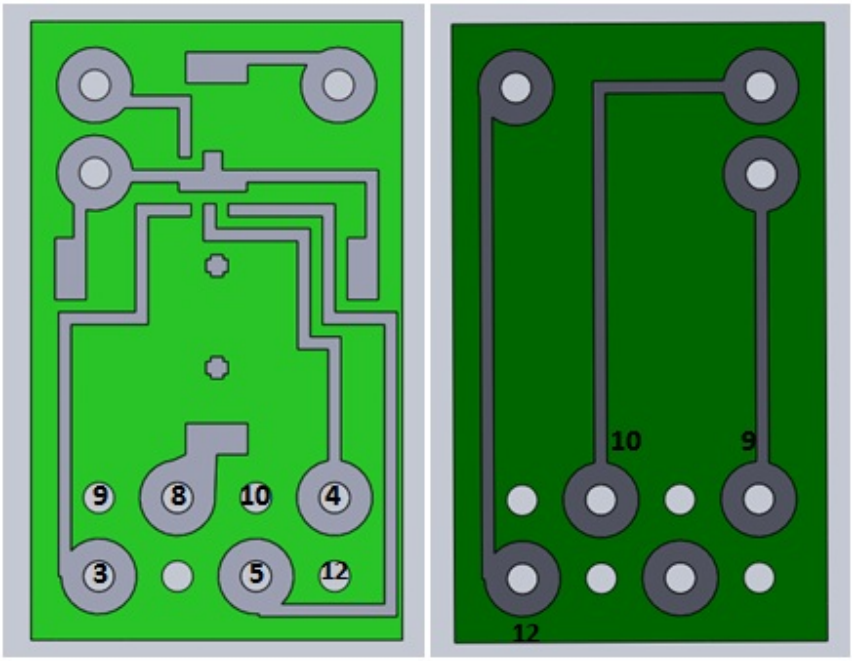

Figure 42: Front and back view of new 6x10mm PCB design

The PCB design is shown in Figure 42. To reduce the size and keep to the 0.2mm minimum feature size that the PCB Company requires a dual layer needed to be constructed. The microphone was assembled over the top layer which contains two alignment markings for the lens array. Alignment of the microphone package was the same as previous designs on this PCB. Due to limited space, routing was made to the most available pin position. Pins are numbered in Figure 42. These routing positions correspond to previous pin allocations on the 12pin TO header shown in the Table 3.

The final package for the BTE haring aid is shown in Figure 43. The inside of the hearing aid shell was used to route wires from the socket with microphone cartridge through a hole in the bottom of the hearing aid SLA to a preamp and IO routing box. To avoid capacitance issues of those wires coaxial cables was used.

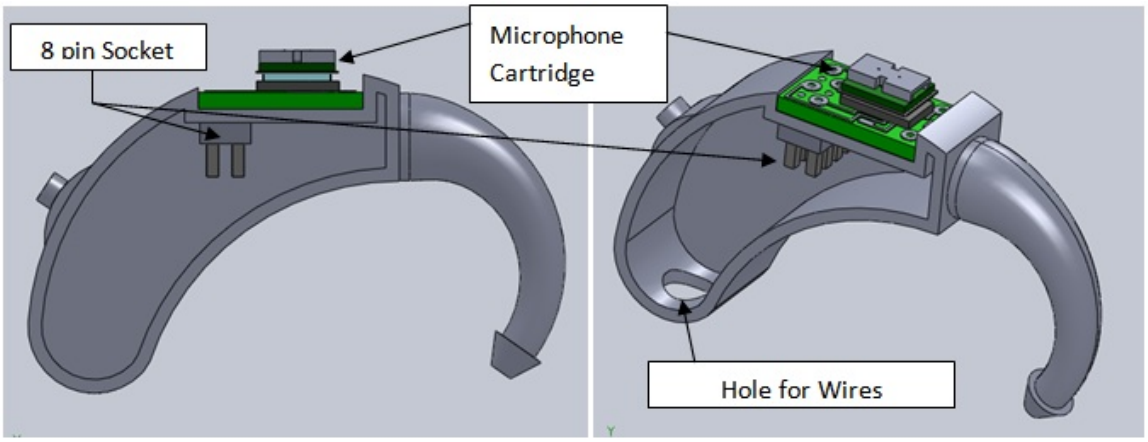

Figure 43: Fully assembled package for BTE hearing aid with directional microphone

Using a similar procedure to the TO Header setup described in the previous section several of these devices were created along with an IO cable to integrate the new package into the current setups. Images of these completed devices are shown in Figure 44.

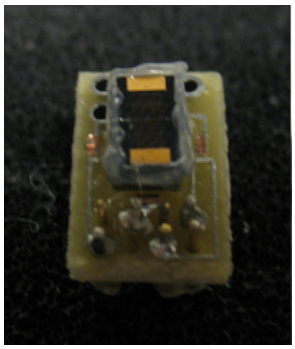

Figure 44: Completed fully assembled package for BTE hearing aid with directional microphone

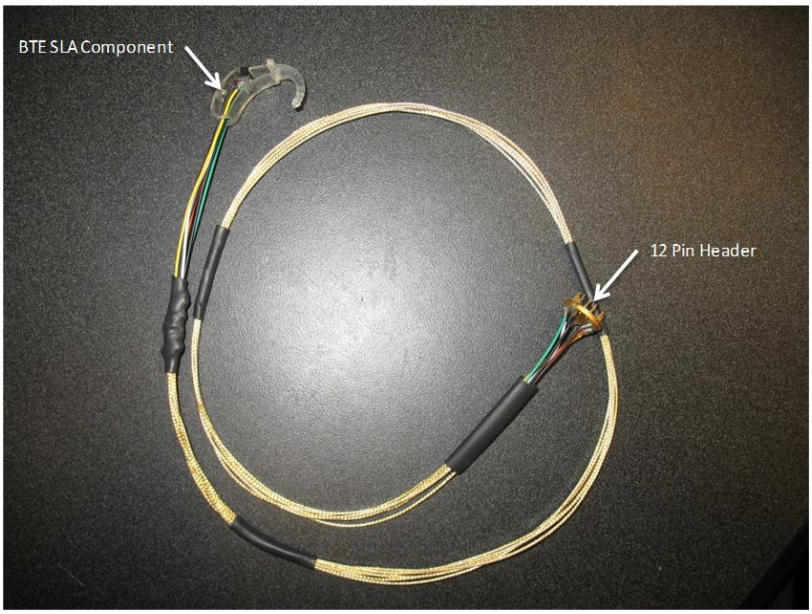

Figure 45: Image of the BTE IO cable with SLA

For the remainder of the analysis, the test results reflect the TO header package. While data was collected for these devices and the results were similar to that of the TO Header package, the TO Header results are more accurate in the characterization for the microphone diaphragm, specifically the directivity pattern, because of the package's symmetric design.

CHAPTER III

CHARACTERIZATION OF THE DIRECTIONAL OPTICAL MICROPHONE

This chapter will first address the theoretical modeling of the microphone; specifically, the first two dominant dynamic modes of the diaphragm. The chapter will then go into noise analysis of the microphone. Once the microphone has been properly described, the chapter will discuss the test procedures and results in characterizing the microphone device acoustics, noise, directivity and optical curve.

3.1 Acoustic Sensitivity

3.1.1 Theory

It was shown in Section 2.1 that the microphone was able to detect pressure gradient due to its ability to sense rotational displacement of the diaphragm. It has also been shown that the diaphragm of the microphone operates in two distinct modes within the audible frequency range. These modes are shown in Figure 46, the first mode of operation is the desired mode where the diaphragm behaves like a see-saw with a rocking type behavior. The second mode occurs at higher frequencies, and causes the diaphragm to act in a flapping motion. In this mode the two halves of the diaphragm start to move in phase. This was undesirable since the diaphragm in this mode is like a conventional omnidirectional microphone with poor directivity patterns.

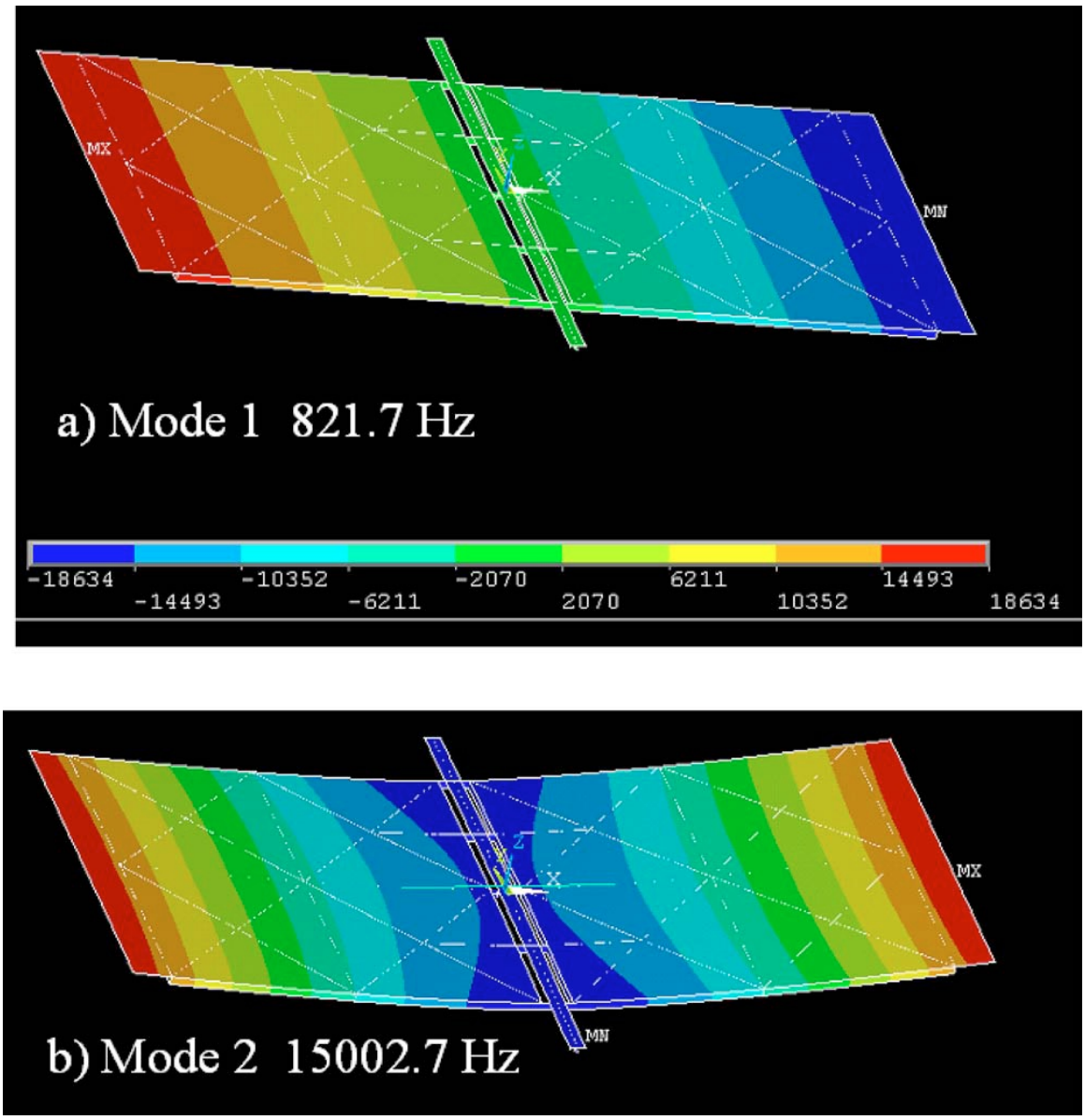

Figure 46: ANSYS simulation showing the two resonant modes of the diaphragm a) rocking see-saw mode b) flapping mode [37]

Each mode of the diaphragm can be decoupled and analyzed individually in order to produce several lumped-parameter models. [37] When operating in its first mode, the diaphragm can be simplified into a simple torsional spring mass damper system. Effects from the backside cavity can affect this system mainly causing some change to the system's spring and damping coefficients. With this in mind, a simple force

balance of the first resonant mode will yield the following differential equation.

$$I\ddot{\theta} + c_t\dot{\theta} + k_y\theta = M(t) \tag{22}$$

$$\ddot{\theta} + 2\omega_{\theta 0}\zeta_\theta\dot{\theta} + \omega_{\theta 0}^2\theta = M(t)/I \tag{23}$$

Here I is the mass moment of inertia for the diaphragm, c_t and k_y is the damping and torsional spring constant respectively. M(t) represents any external moment that was applied to the diaphragm. In the second equation the moment of inertia was divided out of the left side of the equation. The constants $\omega_{\theta 0}$ and ζ_θ are the resonant frequency and damping ratio of the diaphragm. The diaphragm was designed to have a 1^{st} mode resonant frequency either at 250Hz or 500Hz.

As shown earlier in Equation 18 the moment is a function of pressure gradient, as such the first resonate mode was the mode of interest for the device. The other order caused distortion in the pressure gradient observed. Squaring the differential equations shown in Equation 22, and converting it into the frequency domain will yield the following power spectral density profile.

$$S_{\theta\theta}(\omega) = \frac{S_{MM}(\omega)/I^2}{(\omega_{\theta 0}^2 - \omega^2)^2 + (2\omega_{\theta 0}\zeta_\theta\omega)^2} \tag{24}$$

Here S_{MM} is the power spectral density of the external forces, and ω is the independent frequency variable.

The other mode also behaves like a spring mass damper system. The main difference between the two, as shown by Figure 46, was the spring behaves like a linear spring instead of a torsional one. Despite this difference, a similar approach can still be used to produce the following differential equation for the 2nd order mode.

$$m\ddot{X} + c\dot{X} + kX = F(t) \tag{25}$$

$$\ddot{X} + 2\omega_{X0}\zeta_X\dot{X} + \omega_{X0}^2X = F(t)/m \tag{26}$$

In Equation 22, m represents the mass of the diaphragm c and k are damping and spring constants, the ω_{X0} and ζ_X terms are the resonant frequency for the 2nd mode and damping ratio respectively. Also, this mode was affected by the force exerted on the diaphragm instead of the moment indicated by the function F(t). Power spectral density function of the second mode is shown in Equation 24.

$$S_{XX}(\omega) = \frac{S_{FF}(\omega)/m^2}{(\omega_{X0}^2 - \omega^2)^2 + (2\omega_{X0}\zeta_X\omega)^2} \tag{27}$$

The S_{FF} is the power spectral density of the force input which can be contributed by a number of sources e.g. pressure, electrostatic, and thermal noise. As mentioned before the analysis described was assuming that the two modes to be decoupled. In actuality, the two modes are coupled through the detection method, since the microphone senses is the total displacement of the diaphragm at one of its ends. Thus, the two modes are coupled via the measurement method in the following form.

$$Y = (L/2)S_{\theta\theta}(\omega) + S_{XX}(\omega) \tag{28}$$

Y in Equation 28 represents the motion of the diaphragm as observed by the interferometric sensing scheme. In addition to the dynamics of the diaphragm other effects that alter the shape of the power spectrum are a result of noise sources. This was from three main sources, the first was a process noise, or thermo noise, which had a flat frequency response described by Equation 29.

$$S_T = \frac{K_B T c}{\pi} \tag{29}$$

Equation 29 is the power spectral density for the noise contributed by thermal vibrations. K_B is the Boltzman's constant, T is temperature, and c is a damping constant dependent on the diaphragm dynamics. The other sources for noise were from sensor noise that occurred when the final signal was recorded. This can be either

from electronic noise located in the preamp and acquisition equipment, or from the photodiode. The noise from the photodiode is more commonly known as shot noise, resulting from the P-N junction used for photo detection.

$$V_{Shot} = R_{amp}\sqrt{2\frac{V_{DC}Q_e}{R_{amp}}}; \tag{30}$$

Where R_{amp} is the resistor on the current amplifier, V_{DC} is the DC level of the output signal and Q_e is the charge of an electron, specifically 1.6×10^{-19} C.

3.1.2 Results

The microphone was characterized with a chirp signal that sweeps the frequency range of interest. The test was conducted in the anechoic chamber, a sound proof enclosure, which dampens sound waves from around 50Hz to 20 kHz. The general test setup for microphone characterization is shown in Figure 47.

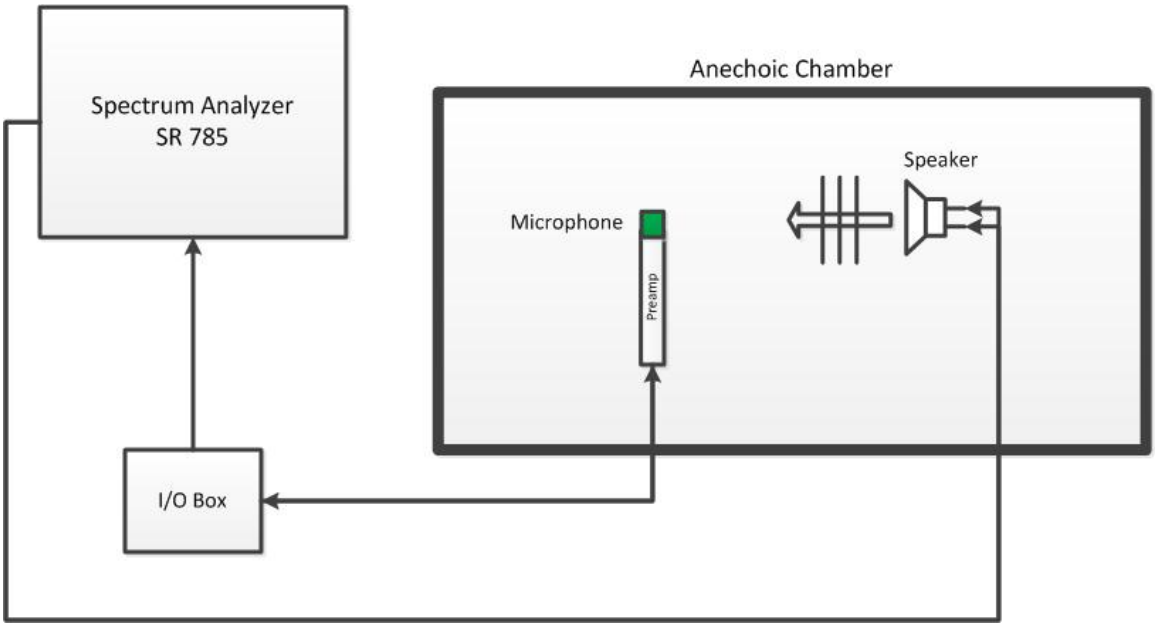

Figure 47: Characterization setup

The microphone was compared to a Larson Davis 2541 0.5" free field microphone, which was calibrated each time with a Larson Davis Cal250, a calibration pistophone

that outputs a 114 dB SPL sinusoid at 250 Hz. The general procedure for the characterization was as follows. After setup, the Larson Davis (LD) microphone was first calibrated to ensure accurate pressure measurements are recorded. The microphone device was then set to an optimal sensing point with electrostatic biasing. The next step was to record the noise level of the microphone device. A measured power spectrum of device w754-0602 is shown in Figure 48.

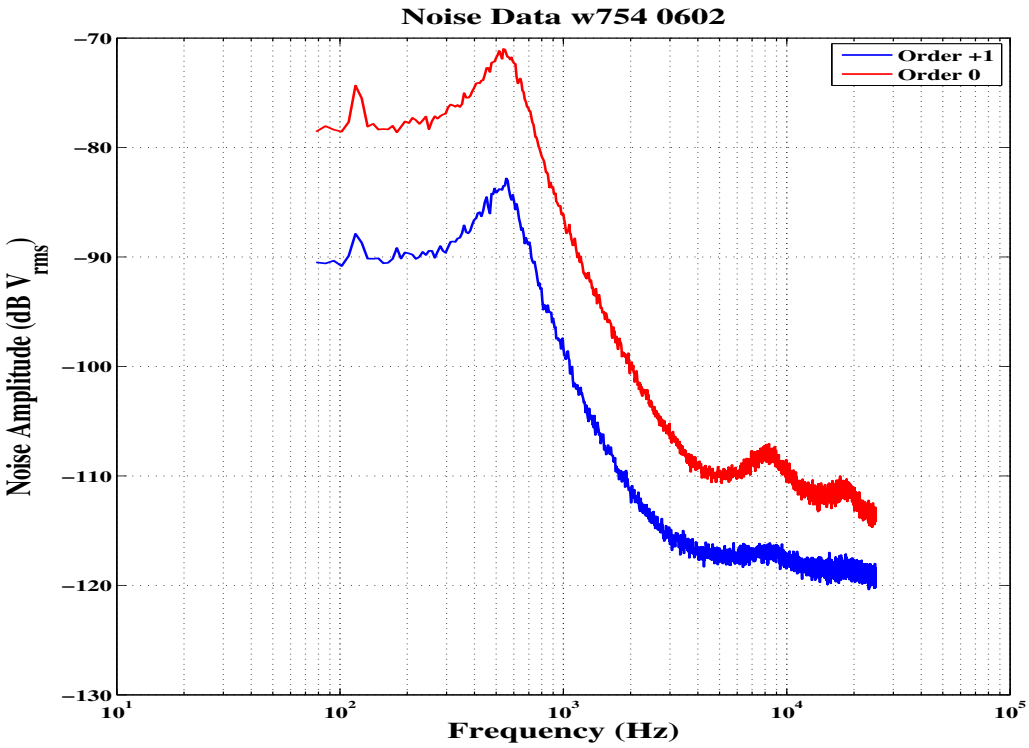

Figure 48: Measured noise profile of microphone device

The resonant frequency of the device at first mode of operation was around 500 Hz. The second mode can be apparent at higher frequencies. For this device the second mode seems to appear around 8.5 kHz, as seen by the second peak in the noise profile. Once the noise recording for the device was measured a chirp signal was played through a loudspeaker and the spectrum was recorded again with the pressure wave present. The LD microphone was also used to record the pressure input to

the device. Using the calibration information obtained earlier, the recorded signal from the LD microphone was converted into a pressure reading which was divided by the chirp signal recording to get the sensitivity profile of the device in dB(re: V_{RMS}/Pa_{RMS}).

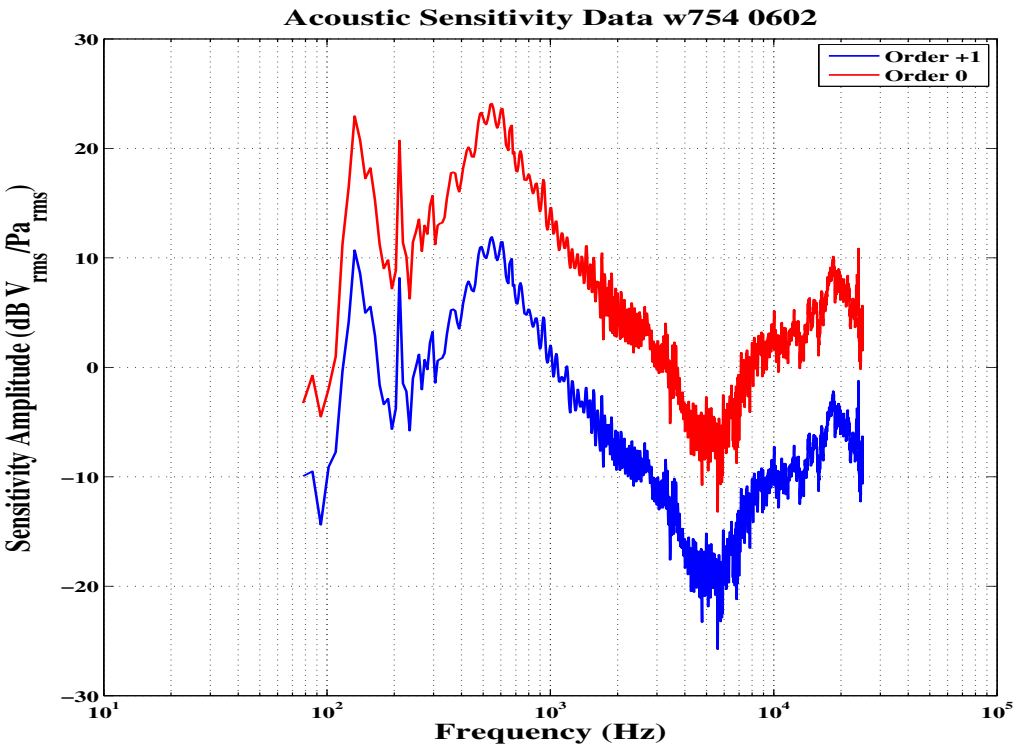

Figure 49: Sensitivity profile of the microphone device

Figure 49 shows the sensitivity profile for the particular microphone device. Some notable aspects of the profile are that, because of the detection of pressure gradient the profile has a 20 dB/decade slope increase over at the 1^{st} mode operation frequency range. Around 5 kHz, a combination of the second mode of the diaphragm and the electronic noise floor starts to dominate the signal and the sensitivity curve increases again. This increase however can be misleading, since some of the signal was a result of noise acting as measured signal. Once the sensitivity profile was obtained this was divided by the noise profile of the device obtained earlier shown in Figure 48. The

resulting profile is the acoustic noise profile of the diaphragm shown in Figure 50.

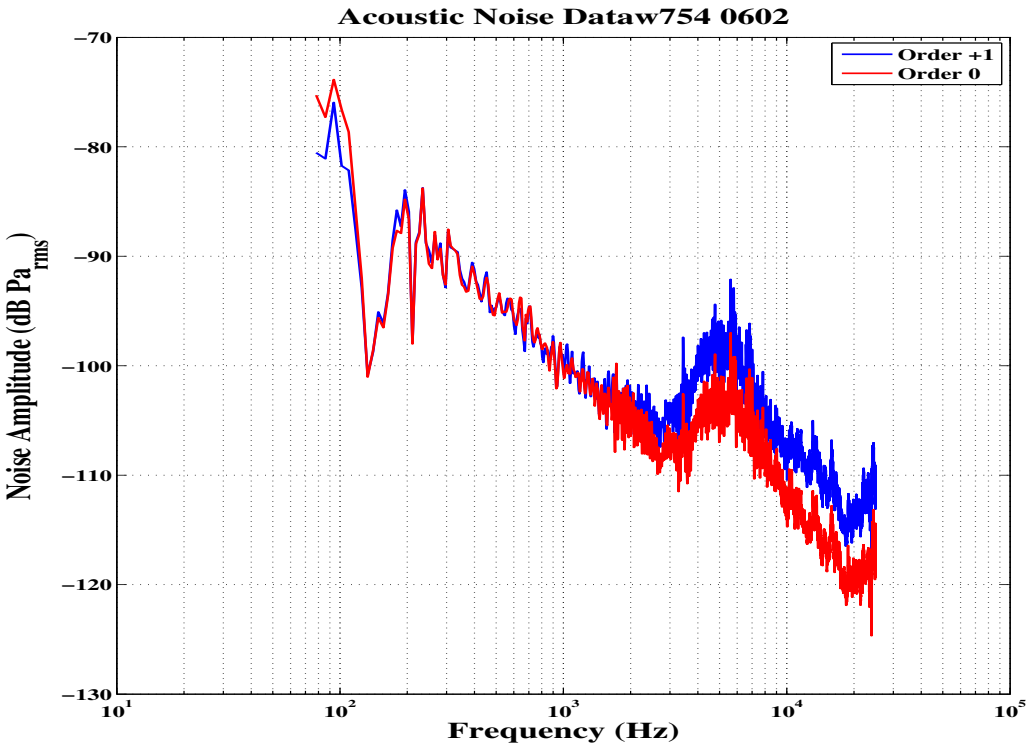

Figure 50: Acoustic noise profile of the microphone device

Figure 50 shows the acoustic noise profile measured for the same microphone. When the microphone was operating in its first mode the noise was detected on a 20 dB/decade slope due to the differentiation of the noise. After 2 kHz the acoustic noise profile starts to get distorted by the second mode of operation of the diaphragm. Preceding the second resonance the noise profile decays at a rate of 40 dB/decade until the electronic noise floor was hit. For this particular device shown in Figures 49 and 50, the noise floor started to dominate around 20 kHz.

With the acoustic profile defined, an A-weighting was placed on the spectrum shown in Figure 50 the area under the spectrum was then integrated to achieve the dBA SPL level of the microphone. This particular device shown in Figures 48 - 50 had a noise level of 30.6 dBA SPL for the 0th diffraction order, and 33.5 dBA SPL

for the 1st diffraction order of the device. For the 0th order there was a 6 dBA SPL improvement over previous designs of the biomimetic microphone. The theoretical noise level that was calculated for his particular diaphragm was at 30.5 dBA SPL. This shows that very little performance was lost due to packaging of the microphone diaphragm. In addition to this, the 30.6 dBA SPL noise level was significantly lower than other commercial directional microphones that have typical noise levels around 45 dBA SPL. The 15 dBA SPL drop in noise level correlates to a 5.6 times reduction in noise level from current directional microphone technology. Meaning, the device successfully was able to not only extend the operation frequency range of a directional microphone, but significantly improve on its noise level as well.

3.2 Optical Profile Measurements

3.2.1 Theory

In order to better understand how the devices operate with bias it was important to be able to characterize the optical response of the device. Figure 13 shows an ideal optical curve with respect to gap displacement of the parallel plate capacitor. The gap displacement was proportional to the force electro statically applied to the capacitor. The formula for applied voltage to force applied is shown in Equation 31.

$$F_{es} = \frac{\epsilon A}{2} \frac{V^2}{(g_0 - \Delta g)^2} \tag{31}$$

Here V is the applied voltage, g_0 is the initial gap of the gap capacitor and Δg is the perturbation of the diaphragm from this initial point. Due to the small angle approximation in conjunction with the snap down voltage phenomenon mentioned earlier, it can be assumed that $1 > g_0 >> \Delta g$. Since bias only deals with the DC behavior of the device it can also be assumed that the device operates only in the first resonant mode and the diaphragm transient behavior had no effect on the bias. Using this assumption the following moment balance can be assumed on the system.

$$(F_{Port1} - F_{Port2})\frac{L}{2} = k_\theta \theta \tag{32}$$

This moment balance equation was based off the following schematic in Figure 51.

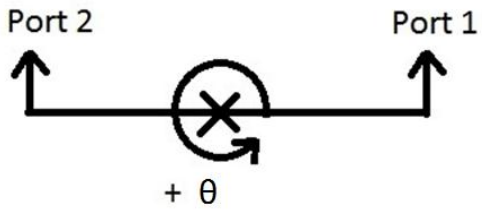

Figure 51: Schematic of moment balance equation

The arrows in Figure 51 represent the positive direction of each component. Considering that $\Delta g = 2\theta/L$ and expanding the force terms in Equation 32 gives a resulting equation relating the change in gap displacement to the input voltage. Furthermore, considering the previous assumption that $1 > g_0 >> \Delta g$ any term that has Δg with a power greater than 2 can be considered negligible. Thus the expansion of Equation 32 yields the following form.

$$1 = \frac{\epsilon A}{2}\left(\frac{V_{Port2}^2 - V_{Port1}^2}{k_\theta g_0 \Delta g}\right) \tag{33}$$

The resulting Equation 33 shows a hyperbolic relationship between the gap and electrostatic voltage. Since the microphone output was directly proportional to the gap it can be inferred that the output of the diaphragm will follow a similar hyperbolic relationship to the input voltages.

3.2.2 Results

In order to characterize the optical profile for the microphone device the electrostatic bias was swept from no bias to 10 V or snap down if that occurred sooner. The test was run with an Agilent E3631A Triple DC Power Supply connected via GPIB to

MATLAB which controlled the supplys voltage levels. The data was measured with a Tektronix TDS2004B scope that was also connected to MATLAB for data retrieval. The test swept port 8 in a quadratic fashion up to that ports single bias snap down voltage, after which bias to port 12 was stepped in a quadratic fashion for another sweep of port 8. At each data point the device was allowed 2 seconds to settle after which the oscilloscope would average 2500 data points and transmit the result to the computer for recording. Altogether for each run 10,000 data points were collected over the course of 6.7 hrs. Figure 52 displays the results for device w754-2305.

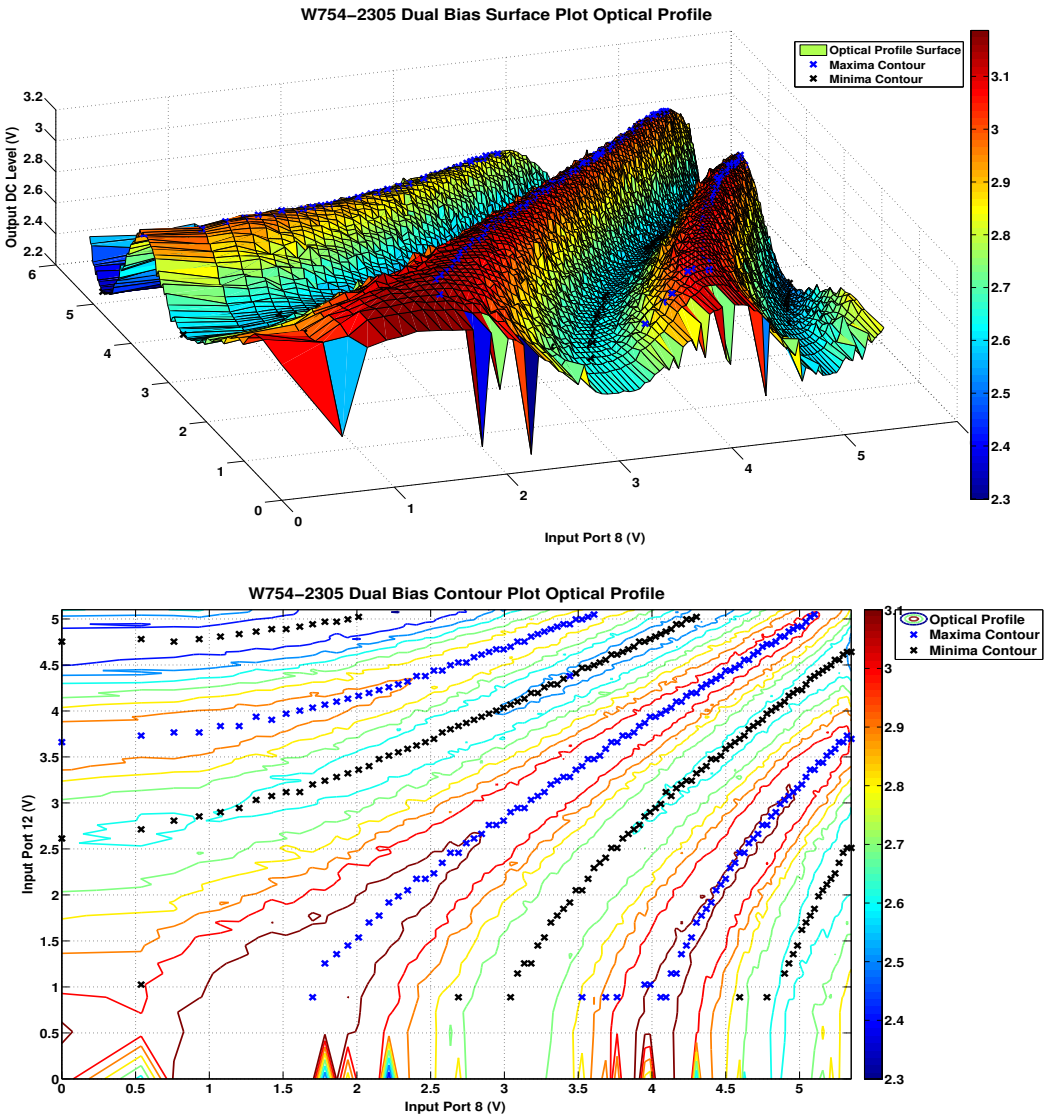

Figure 52: Dual bias optical profile

Figure 52 shows the hyperbolic structure of the optical curve. Also shown are the max and min points on the contour graph. Because one port causes positive displacement while the other port creates negative displacement the trends of these points indicate the combination of the two biases that allow for the same displacement of the sensing end of the microphone. Plotting Figure 52 with respect to the input voltages squared linearizes the results as shown in Figure 53.

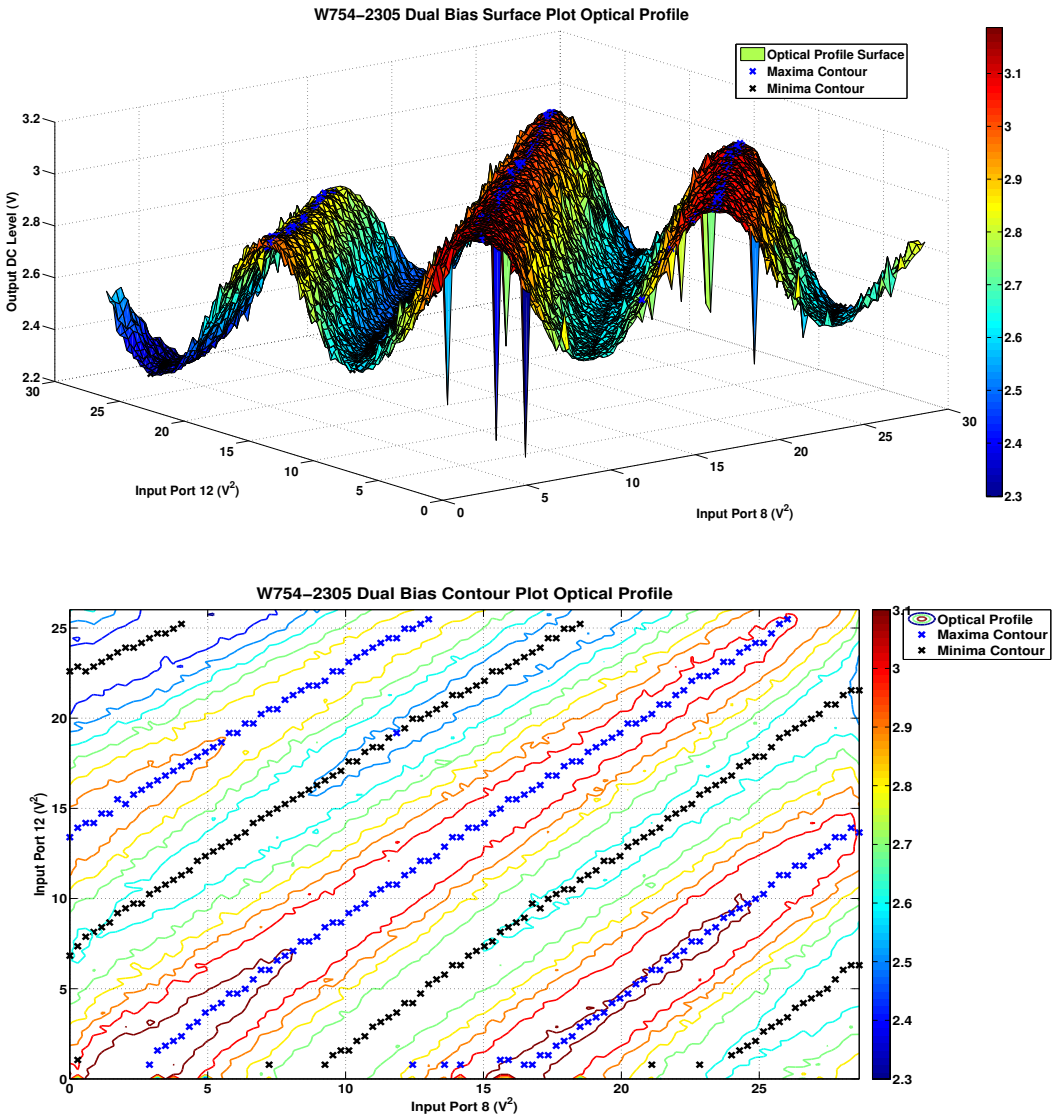

Figure 53: Dual bias optical profile with inputs squared

The results shown in firgure 53 are the linear results of the biasing. With the linearization any section of the curve down either axis results in the optical profile talked about in Figure 13. The max min lines that showed the hyperbolic relationship mentioned in Equation 33 are not linear lines. The lines are expected to have a slope of 1. The reason why they do not show this was due to asymmetries between the two electrostatic ports. The offset of the curves was related to the initial gap of the sensing side of the diaphragm.

3.3 Directivity Measurements

3.3.1 Theory

The goal for the microphone was to produce a microphone with a directional pattern that reduces noise in certain directions. Thus a figure eight pattern was desired for frequencies spanning the audible frequency range. The main concept behind the figure eight directional pattern is a result of the differential detection of the pressure gradient, in that when a pressure wave is approaching the diaphragm in its most sensitive direction the wave is sensed by the diaphragm as a longitudinal wave. As the incident angle of the pressure wave is rotated from this sensitive position the wave starts to have a transverse component causing the phase delay between the two halves of the diaphragm to be shorter than the norm. When the pressure wave is perpendicular to the diaphragm the wave is seen as entirely transverse, thus no pressure gradient was observed and only translational motion of the diaphragm was measured. To quantify the figure eight pattern and give a measure of directivity to the diaphragm, the directivity index was used.

$$DI = 10\log_{10}\left(\frac{4\pi|p_{ax}|^2}{2\sum_{m=1}^{2\pi/\Delta\theta}|p(\theta_m)|^2\Delta\theta}\right) \tag{34}$$

Equation 34 shows a finite way of calculating the directivity index, p_{ax} is the axial pressure measured (incident angle 0 degrees), this value should be the largest value in the directivity measurements and serves as a normalization factor. Also, as Equation 34 indicates, the directivity index calculation is independent of the external pressure wave's frequency.

3.3.2 Results

The directivity test setup is shown in Figures 54 and 55 . The microphone was attached to a rotation stage controlled by a Newport EPS300 controller. The fixture

holding onto the microphone was shielded by insulation to dampen reflections coming from the fixture.

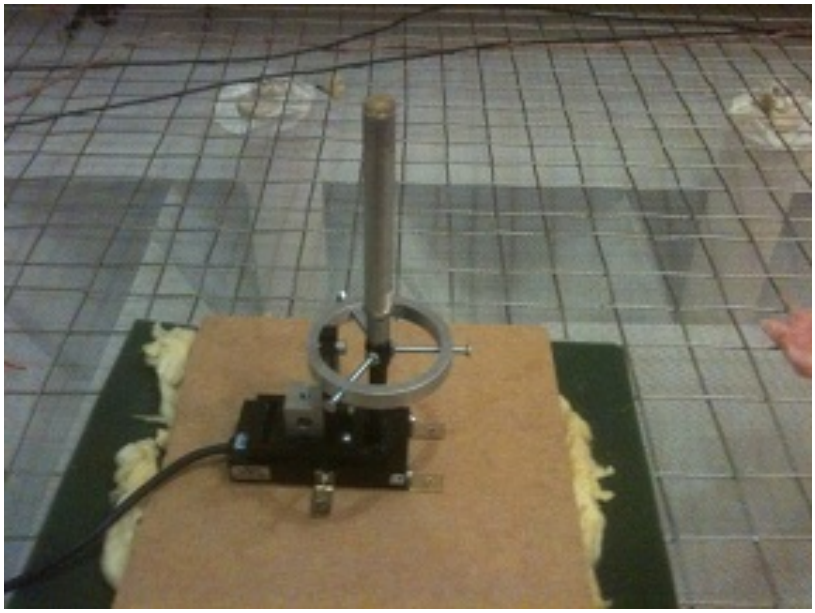

Figure 54: Directivity test setup without sheilding

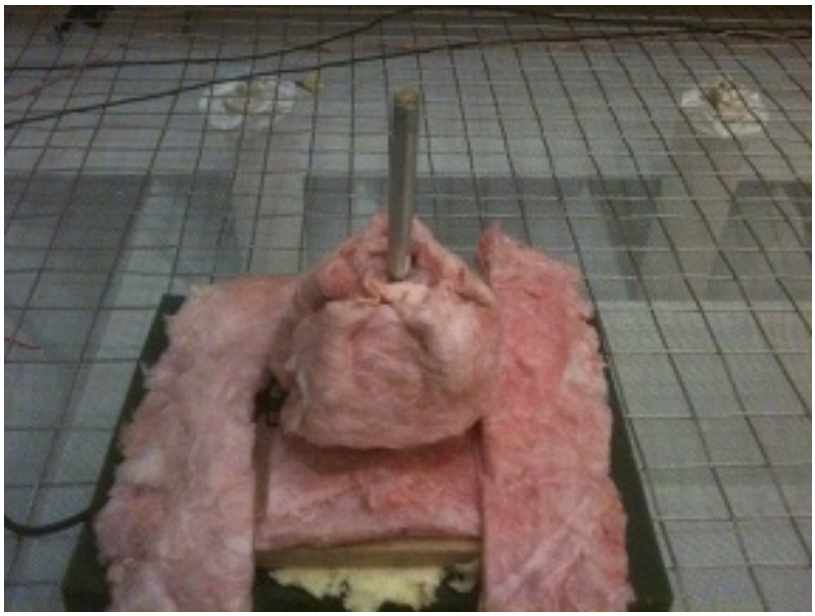

Figure 55: Directivity test setup with sheilding

The directivity setup shown in Figures 54 and 55 were placed in the anechoic

chamber to reduce reflective surfaces that would affect the directivity pattern. Once the setup was in place the test was performed by sending a tone burst at different frequencies to the microphone, a middle section of that tone burst was recorded by a sound card, this was so the transient behavior of the diaphragm would not affect the recordings. The rotation stage was moved 360 degrees in 3 degree increments at the end of which the directivity pattern was plotted and the directivity index was calculated using Equation 34.

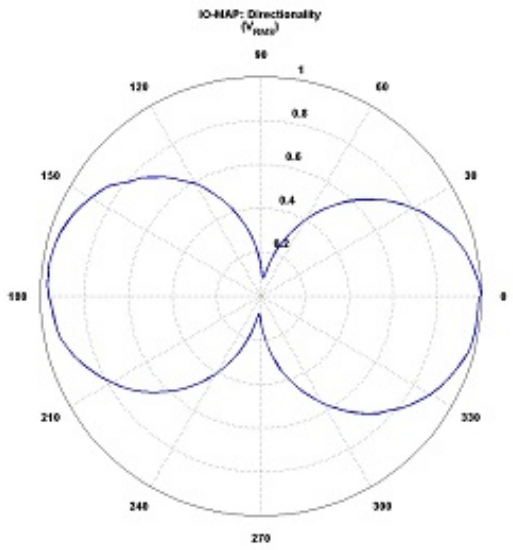

Figure 56: Directivity profile at 500Hz

Figure 56, shows the directivity pattern at 500 Hz, the device's first resonant mode. When the first mode was dominating the output signal, the directivity index was relatively constant. For 500Hz a directivity index was calculated to be at 5.3717 dB(re:arb). At 90 degrees there should be a null in the directivity pattern; however, because of the second mode, some signal was still detected, which was why the pattern never goes to zero at a perpendicular orientation.

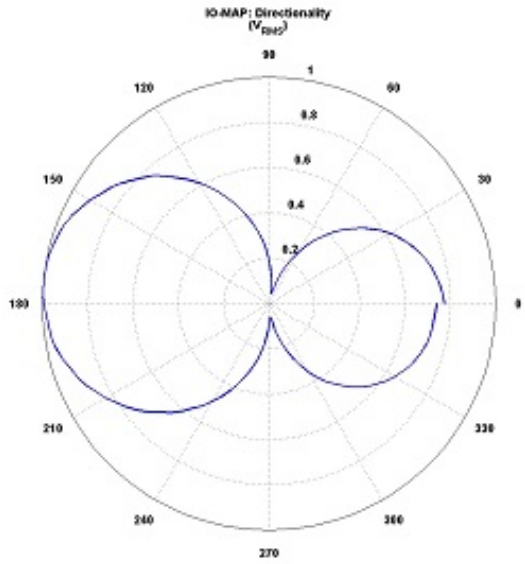

Figure 57: Directivity profile at 3 kHz

Figure 57, shows the directivity pattern at 3 kHz. At this frequency another pattern starts to emerge. This shows some asymmetry in the diaphragm appearing when the first and second mode are both present in the signal. Even though directivity still exists and was fairly high for this measurement, 5.3681 dB(re:arb), the profile was not desired because of the distortions due to the second mode coming into effect. The physical interpretation of the asymmetric pattern was that for one side of the diaphragm the diaphragm displacement due to the pressure wave will add both the second and first mode responses together. The other side of the diaphragm the translational motion of the diaphragm will subtract with the torsional motion diminishing the detected signal.

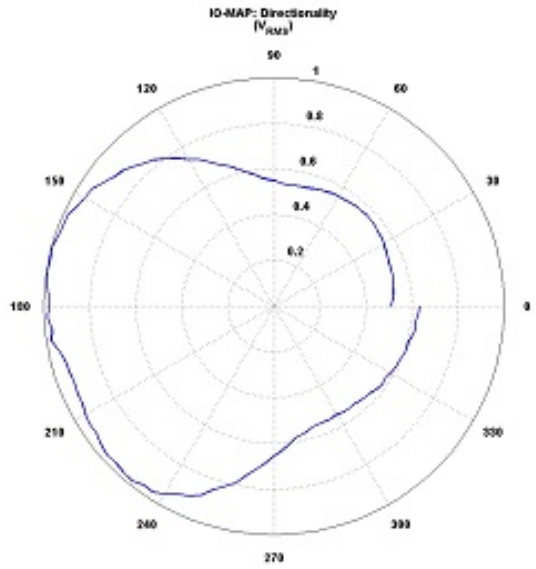

Figure 58: Directivity profile at 9 kHz

Figure 58 displays the directivity pattern of the device measured at 9 kHz. The directivity index measured was 3.4854 dB(re:arb), which was significantly less than the previous measurements. The reason for this was that the second mode of the diaphragm was now dominating the measurement. Thus the directivity pattern was more circular like an omnidirectional microphone. It should be mentioned though that the first mode was somewhat present in the signal as can be seen by the asymmetry of the profile.

CHAPTER IV

PULSED VCSEL OPERATION

One of the main objectives for this directional microphone was to eventually implement the diaphragm on a hearing aid device. In order to accomplish this task power consumption must be addressed in order to ensure that the lifetime of the working device will be sufficient for real world applications. Currently, most of the power consumption of the device was due to the continuous operation of the VCSEL, which requires 12mW of power to operate. To reduce the power requirement for this component a pulsing operation for this element was proposed. This would effectively reduce the intensity of the VCSEL light without affecting the beam profile of the VCSEL. The following chapter will delve into the power optimization via pulsing in particular addressing the limits of the technique due to tradeoffs in signal to noise ratio (SNR).

4.1 Sampling Theory

Through pulsing operation lower power consumption for the VCSEL can be achieved. While this was a desirable result the new mode of operation for the measurements acts as a discretizing process that introduces new issues to the microphone. The main two components of this are harmonic generation of the signal at multiples of the sampling frequency and aliasing that can now occur with higher order frequencies. While more sophisticated pulses can be applied to the device, a simple pulse train like the one shown in Figure 59 was used to determine the benefits of this power optimization technique.

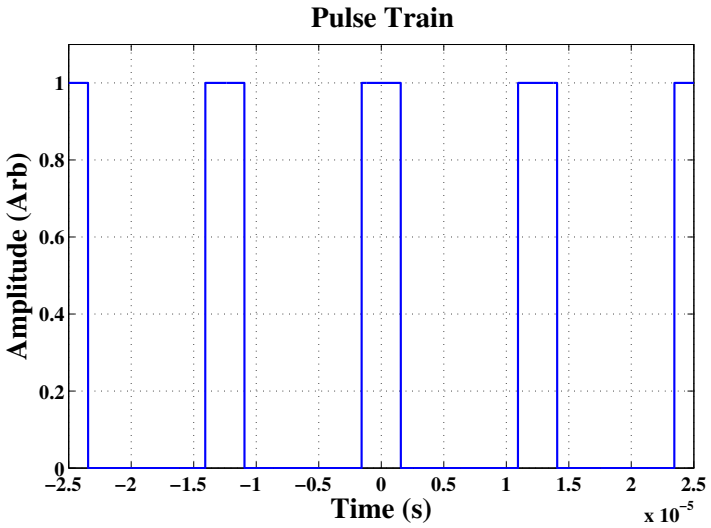

Figure 59: Time plot of a 40kHz pulse train with 25% duty cycle

The VCSEL was a Gaussian laser, whose intensity can be calculated with the following expression.

$$I(r,h) = \frac{2P_{avg}}{\pi w(h)^2} \exp\left(\frac{-2r^2}{w(h)^2}\right) \tag{35}$$

In equation 35 the intensity is characterized by r, the radial distance from the enter axis of the emitting aperture and h, the distance along the central axis w(h) is defined as follows.

$$w(h) = w_0\sqrt{1 + (h/h_r)^2} \tag{36}$$

This defines the effective width of the beam profile where the boundary of the laser is defined by $1/e^2$ of the max intensity located along the beam's center axis. The variable h_r is the Reighlay length of the VCSEL, and w_0 is the diameter of e active area on the VCSEL, acting as the initial width. Equation 35 also shows a dependence on the power used to drive the VCSEL, denoted by P_{avg} , which can be defined as the time average of the power. As such the pulsed intensity of the VCSEL light was dependent with the time average supply power for one sampling period

shown by Equation 37.

$$P_{avg} = \frac{1}{T} \int_0^T P(t)dt \tag{37}$$

Here, T is the period of one pulse or sample period P(t) is the driving power function for the VCSEL element. During pulsing operation the function P(t) is a simple pulse train going from 0 W to the 12 mW of power needed to activate the VCSEL. Solving equation 37 for a pulse train will lead to P_{avg}=Pτ, where P is the 12mW needed to drive the VCSEL, and τ is the duty cycle of the pulse train.

As mentioned before, the pulsing operation acts as a sampling switch for the measurement. As such, the signal detected was discretized to a sampling rate the same as the pulsing frequency causing the time signal to be convoluted with a pulse train. The convolution that occurs can better be understood in the frequency domain which simplifies the analysis to a multiplication of two frequency spectrums, specifically the microphone's and the pulse train's. The half frequency spectrum of the microphone diaphragm was shown in the characterization chapter, Figure 48 is the specific spectrum that is being referred to. The spectrum is called a half spectrum since the full spectrum is symmetric for negative frequencies. The spectrum for the pulse train can be described by its Fourier series. For simplicity, the Fourier will be looked at in its trigonometric form, which is as follows.

$$\begin{aligned} a_0 &= \frac{1}{T} \int_{-T/2}^{T/2} x(t)dt \\ a_n &= \frac{2}{T} \int_{-T/2}^{T/2} x(t) \cos\left(\frac{2\pi tn}{T}\right) dt \\ b_n &= \frac{-2}{T} \int_{-T/2}^{T/2} x(t) \sin\left(\frac{2\pi tn}{T}\right) dt \end{aligned} \tag{38}$$

Equations 38 through 38 break up the Fourier series equation into its components, a_0 can be seen as a DC term, a_n is all even components of the series, and b_n are all of the odd components. Since the pulse train is a symmetric function only even components will exist in the series, thus b_n is always zero. Solving the other two equations then will yield the Fourier series for a pulse train as shown in Equations 39 and 39.

$$\begin{aligned} a_0 &= I\tau \\ a_n &= 2I\frac{\sin(n\pi\tau)}{n\pi} \end{aligned} \tag{39}$$

In Equations 39 and 39, I is the intensity of the light coming from the VCSEL and τ is once again the duty cycle of the pulse train. For a duty cycle of 25% the Fourier coefficients are as shown in Figure 60.

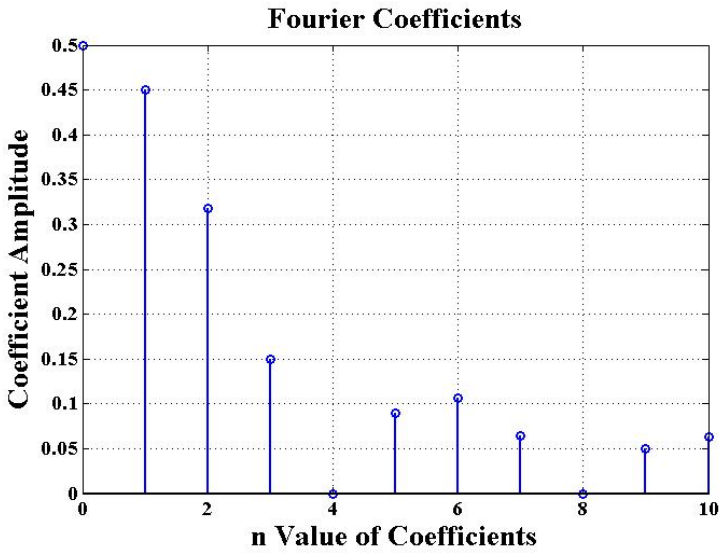

Figure 60: Fourier coefficents of a pulse train with 25% duty cycle

Each coefficient shown occurs at a multiple of the pulse train's fundamental frequency, i.e. the frequency that the microphone is being pulsed at. This frequency spectrum will then be multiplied to the full frequency spectrum of the microphone.

As a result, a repetition or harmonics are produced at every multiple of the sampling frequency of the device. Additionally if the fundamental frequency of the pulse train isn't large enough when multiplied together parts of the microphone spectrum could overlap and cause an increase in signal. This fictitious signal that can be produced is a phenomenon commonly referred to as aliasing, where high frequencies located in the full spectrum are detected as lower frequencies. The point where this phenomenon starts to occur is at half the sampling frequency, known as the Nyquist frequency. In terms of signal reconstruction it is the minimum number of samples that need to be taken within one cycle in order to reconstruct a sine wave. For audio applications this frequency is typically 44.1 kHz making the aliasing frequency at 22.05 kHz just above the audible frequency range. As an additional precaution devices usually have a low pass filter to act as an anti aliasing measure for the device. It is also possible to leave the harmonics and use them to strengthen the measured signal of the device.

The pulsing operation of the device leads to a discretization of the microphone signal. Since the microphone's impulse responce is essentially being convoluted with a pulse train the dynamic equations describing the microphone system will be altered. This low power operation of the device leads its analysis into discretization. Currently digital methods are not being used on the device but future designs may implement these techniques. For digitalization of a signal two operations need to occur. The first is sampling of the continuous signal, which can be handled by the pulsing operation. The other operation is quantization of the signal. Quantization is defined as taking a large set of values and confining it into a smaller set. In terms of digital signal processing the quantization is determined by the number of bits that is chosen to characterize the signal. The bit resolution for a digital converter can be described as follows.

$$LSB = \frac{V_{cc}}{2^{N-1}} \tag{40}$$

Here LSB stands for least significant bit, which is equivalent to the resolution. V_{cc} is the voltage range being investigated, and N is the number of bits being assigned to the signal. As a result the more bits chosen the finer the resolution will be. For common Audio applications the number of bits that signals are typically quantized by is 16 or 32 bits giving a resolution of 30.518e-6 and 0.4657e-9 resolution respectively for a V_{cc} of 1V.

4.2 Signal to Noise Ratio vs Duty Cycle

In the previous section the first harmonic was dependent on a_0, which was directly proportional to the duty cycle that the device was being pulsed at, which was also proportional to the power being consumed by the device. As such, the signal detected also decreased with duty cycle. Although the signal is decreasing the signal to noise ratio (SNR) can be maintained. The main reason for this was due to the fact that while the signal getting detected was getting diminished with reasonable duty cycles the noise profiles are still dominated by thermo-mechanical noise. While dominated by this noise the signal detected was representative of the moving dynamics of the microphone diaphragm. When the duty cycle drops to lower levels the noise level of the device starts to be dominated by the electronic noise since this component of the noise was not dependent on the intensity level of the optical components. When the signal's spectrum was no longer dominated by the thermo-mechanical noise a drop in SNR can be expected. The rate of decay was somewhat linear since the signal was still decreasing by the duty cycle of the pulse train. A reason why the decay was not completely linear was that the electronic noise floor was not constant and will decay due to shot noise levels being dependent on the light intensity. This however will still be less than the thermo-mechanical decay and so the trend was still present. Finally there was an even sharper drop off in SNR when the pulse was too short and was limited by the receive electronics of the microphone.

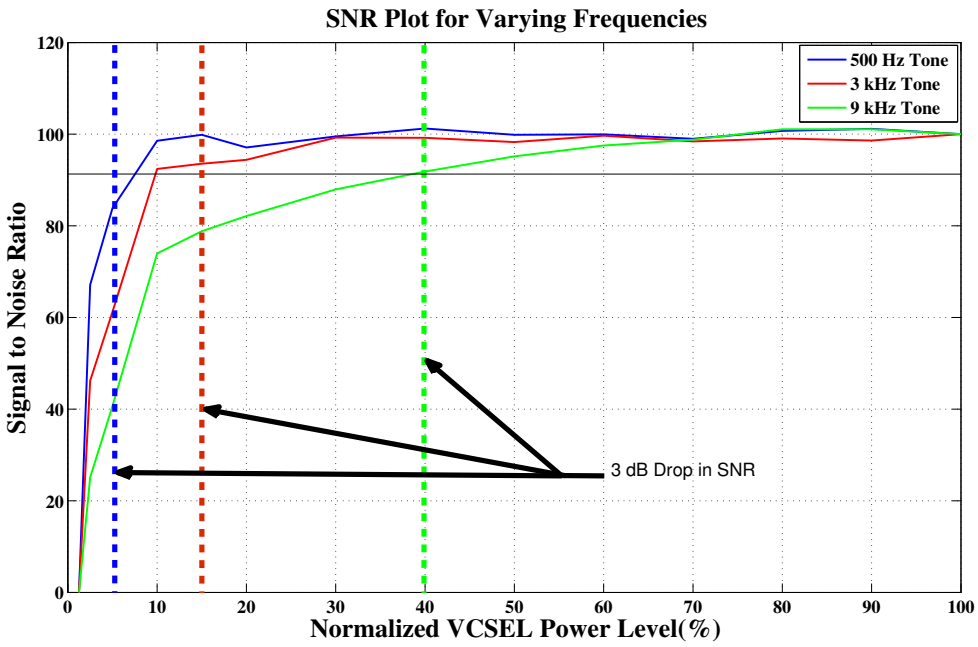

Figure 61: SNR plot versus power consumption level of VCSEL

Figure 61 shows the SNR trends for several frequencies at different duty cycles of pulsing operation, the power level was a time average of the power used to drive the VCSEL. Since the frequency spectrum of the device was not flat across the audible frequency range each frequency will have a different duty cycle where the SNR will start to decay. Looking at the 9 kHz signal the three trends described earlier are apparent. From the continuous 2mW operation to a pulse of 80% duty cycle or 9.6mW power operation the SNR was constant and was dominated by thermo- mechanical noise. After that, till about 10% duty cycle i.e. 1.2mW the noise was dominated by electronic noise and the SNR decays. The final curve was apparent at power levels below 1.2 mW, where the VCSEL pulse was shorter than the rise time of the VCSEL so the signal drops off quickly from this point. A time recording of the pulse signal at 50% duty cycle is shown in Figure 62.

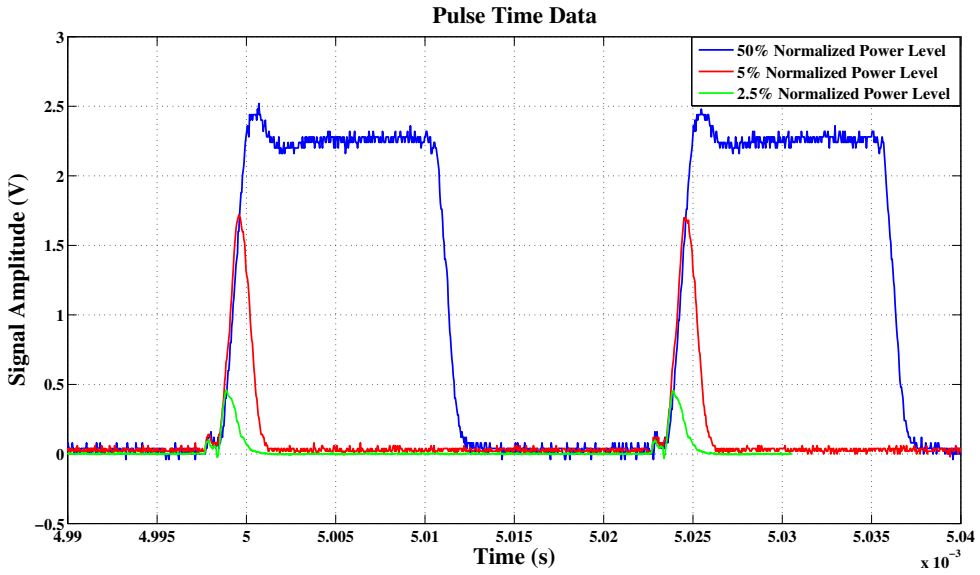

Figure 62: Time data of VCSEL pulse at 50% duty cycle

Figure 62 shows the VCSEL and photodiode responses add a transient component to the recorded signal. This was caused by the preamplifier for the microphone having a cutoff frequency to help initally filter high frequency noise values. The transient behavior of the switching adds some unwanted narrow band noise components to the spectrum as well as decrease the SNR when the time pulse of the VCSEL drops below the rise time of the VCSEL pulse around 10% duty cycle or 3μs. Figure 63 shows several spectrums taken at different duty cycles and the range where thermo-mechanical noise was dominating the signal.

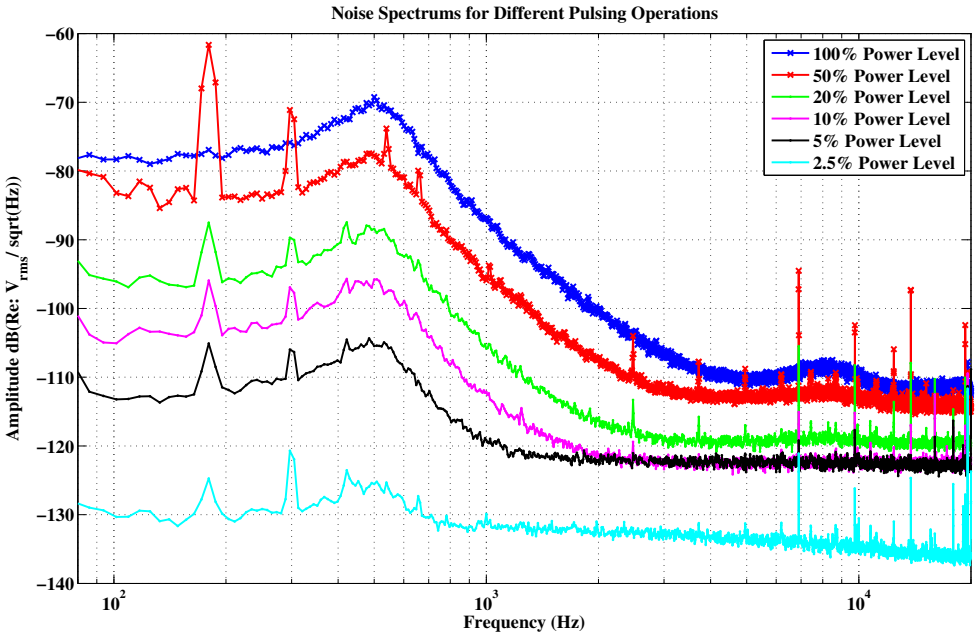

Figure 63: Microphone's noise spectrum with varying power levels

As shown in Figure 63 the boundary lines for the thermo-mechanical noise range is reduced with duty cycle, as described in the theory. The rate of this range decrease was dependent on the slope of the frequency spectrum. So, for flat portions of the curve the noise level crash into the noise floor was almost instantaneous. For attenuation parts of the spectrum, which occur after the resonant peaks, which decay at 20dB/decade so for every 20 decibels of signal loss the thermo-mechanical range's boundary line will move inward by a decade in this attenuation region.

As a result of this, it can be seen that the limiting factor of the pulsing operation was the actual noise of the device having an electronic noise floor. So by looking at the dBA SPL level of the device pulsing limitation can be inferred. This was because when being pulsed at reasonable duty cycles the dBA SPL values will rise with decreasing duty cycle linearly; however, once enough of the spectrum has fallen beneath the noise floor the noise will spike indicating that the device was no longer acting under thermo-mechanical influence. Figure 64 shows the recorded dBA SPL

values at varying duty cycles.

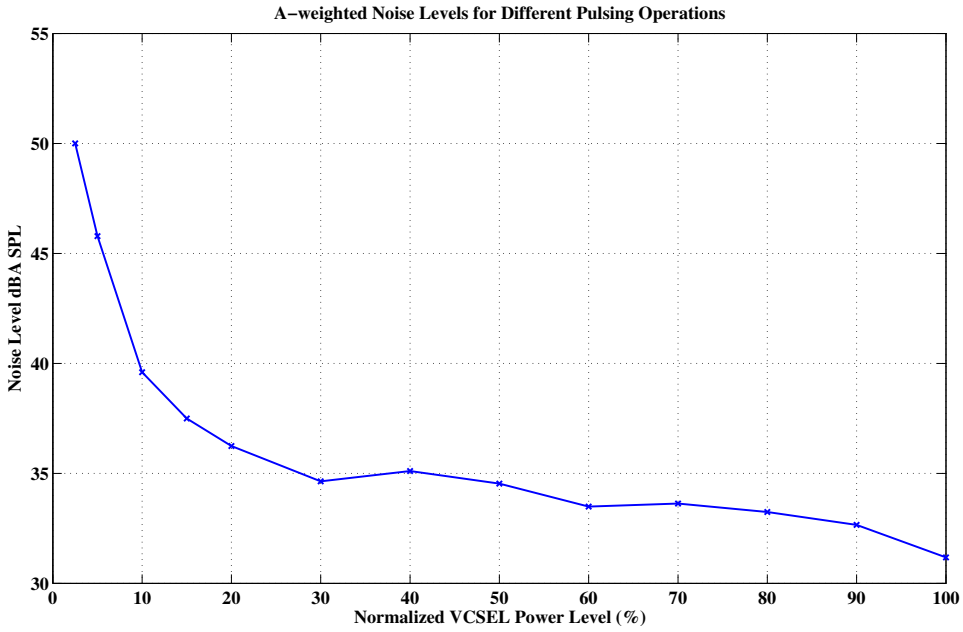

Figure 64: Microphone's dBA SPL values with varying power levels

From Figre 64, it can be shown that pulsing with as low as 20% duty cycle, i.e. 2.4 mW operation power level, can be achieved with acceptable performance loss. Meaning the power consumption of the device can be reduced to 1/5 of its original value.

CHAPTER V

CONTROL METHODS FOR THE MICROPHONE

This chapter will introduce several methods for optimizing the response of the microphone diaphragm and attempt to improve both the directionality and signal of the microphone. The chapter will also go into modeling the nonlinear behavior of the device, which was used to help facilitate designing the controllers used in this analysis. The actual control of the diaphragm is non-ideal since issues such as observability and nonlinearities exist in the system making it increasingly difficult to sense and control. Taking everything into account the following strategies have been introduced to help improve the microphone diaphragm. The model used for the control theory is the same model mentioned in the characterization chapter.

5.1 Simulation of the Microphone Response

To help in the microphone design process a complete model of the microphone was developed through SIMULINK. The following will go through the development of that model and how it compares to experimental data collected on completed devices. There are three main components that were considered when creating the model, which were the inputs, microphone diaphragm, and sensing components. The inputs can be described in the following. The SIMULINK blocks are shown in Appendix B.

The inputs contain the transduction method of the device for both the electrical and acoustic domains. The main focus for these blocks was to rotate the states of the inputs into force and moment relationships such that they could be used with the state space model derived earlier. The electrostatic force is described by Equation 31 discussed in chapter 3. The force of a pressure field on the diaphragm is simply the pressure level multiplied by the area of the diaphragm. The moment exerted on the

diaphragm due to a pressure field was described by Equation 18. It is in this equation where the derivative term of the dynamics appears.

The dynamics of the microphone diaphragm were described in Chapter 3 discussing the characterization of the microphone. As mentioned before the microphone diaphragm was decoupled into two modes of operation. The first mode was a rocking type mode that was actuated solely by moments applied to the diaphragm. The second mode was the in phase flapping mode of the diaphragm, which was actuated by the net force acting on the diaphragm. This dynamic model was represented in a state space model, which follows the standard form.

$$\dot{X}(t) = A_{system}X(t) + B_{system}U(t) \tag{41}$$

$$Y(t) = C_{system}X(t) \tag{42}$$

The states chosen to represent the system were the rotation of the diaphragm, its translational displacement, and the time derivative of the two. This choice of states lead to a fourth order system matrix defined as follows.

$$A_{system} = \begin{pmatrix} 0 & 1 & 0 & 0 \\ -\omega_\theta^2 & -2\zeta_\theta\omega_\theta & 0 & 0 \\ 0 & 0 & 0 & 1 \\ 0 & 0 & -\omega_x^2 & -2\zeta_x\omega_x \end{pmatrix} \tag{43}$$

Where ω corresponds to the natural frequency of each mode and ζ is the mode's damping ratio. The 2x2 matrices on the diagonal are a canonical form of a second order spring mass damper system. Since the two systems are decoupled through the moment and force applied on the diaphragm the off diagonal 2x2 matrices are zero. The inputs for the system were chosen to be moment and force, although this was not the true actuation method of the diaphragm it was a natural choice for defining the system. The input matrix for the system was chosen as follows.

$$B_{system} = \begin{pmatrix} 0 & 0 \\ 1/I_{yy} & 0 \\ 0 & 0 \\ 0 & 1/m \end{pmatrix} \tag{44}$$

The input is a multi input system where the first input is the moment exerted on the diaphragm and the second is the force. The moment is divided by the diaphragm's moment of inertia (I_{yy}) and the force is divided by the mass (m) this is derived from the moment and force balance equations governing the diaphragm's dynamics. The final matrix to describe the linearized dynamics of the microphone diaphragm is the measurement matrix C_{system} it is in this part of the equation where the two modes of the system are coupled together to get the gap displacement output of the system.

$$C_{system} = \begin{pmatrix} L/2 & 0 & c_1 & c_2 \\ -L/2 & 0 & c_1 & c_2 \end{pmatrix} \tag{45}$$

The measurement matrix for the system will give two outputs, the first will be the sensing side gap displacement and the second would be the displacement on the side that is not being measured by the device. The $c_{1\&2}$ represent the diaphragm motion due to the second mode. Given the assumptions made previously, the linear model would give c_1 as 1 and c_2 as 0; however, to match both the device sensitivity spectrum and directivity pattern an antiresonant mode needed to be introduced to the system. This can be viewed as a correction factor for the zero dynamics caused by the diaphragm having internal loading. With this, the system was then implemented into SIMULINK with block algebra. The system block diagram is shown in Figure 65.

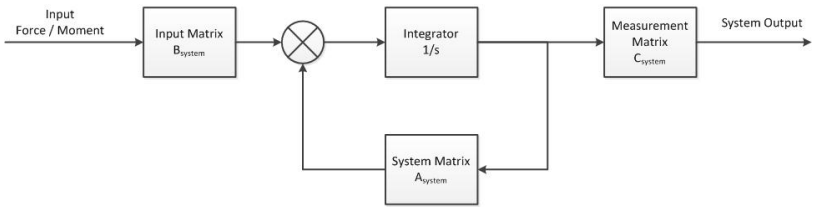

Figure 65: Block diagram of the state space model

The final part of the model that was addressed was to introduce the nonlinear sensing of the gap displacement. This was done by introducing the optical transfer function (OTF) into the system. The equation for the optical transfer function is shown in Equation 46.

$$OTF = A_{preamp}\nu \sin\left(\frac{2\pi}{\lambda}\Delta g\right) \tag{46}$$

Here, λ is the wavelength of the VCSEL light, A_{preamp} is the gain of the preamplifier tube, and ν is the optical efficiency of the device, which would include losses due to light leaking from the lens array and the detection efficiency of the photo diode. The overall model is shown in Figure 66.

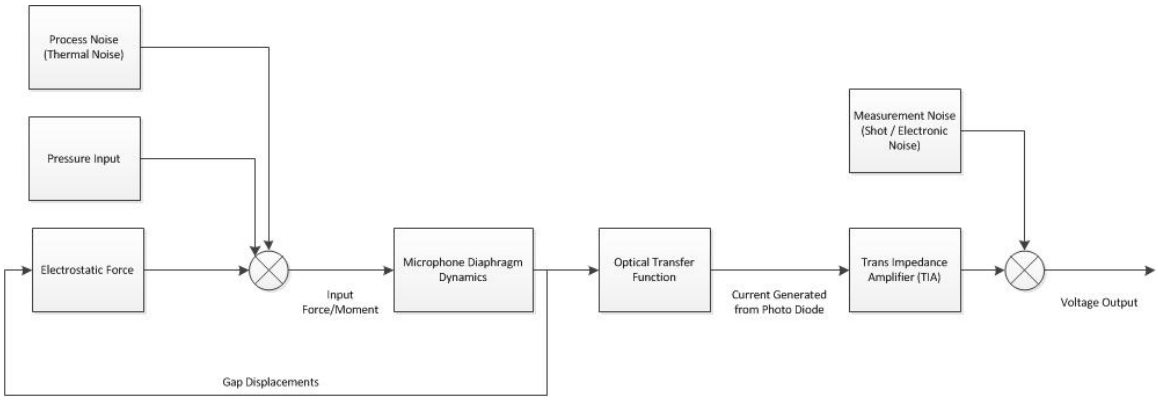

Figure 66: System block diagram

The system shows the overall relationship of the different components that were described earlier. What the overall model also shows is the introduction of the different noise sources into the system. The first noise source is thermal noise, or process

noise, which is caused by Brownian motion of air molecules on the air, and so it is added to the inputs of the plant model. The second source of noise occurs after the optical transfer function, this is representative of the system's measurement noise. This includes disturbances such as electrical disturbances as well as measurement noise like shot noise. Figure 66 also shows the feedback relationship of the gaps to the electrostatic forces that cause the instability known as the pull-in effect. The resonant frequencies and the damping of the different modes were chosen to be similar to the working devices, specifically the model was made to replicate the dynamic response of w754-0602, which had a low noise level and displayed a clear second resonance. The sensitivity spectrum of the simulation is shown in Figure 67.

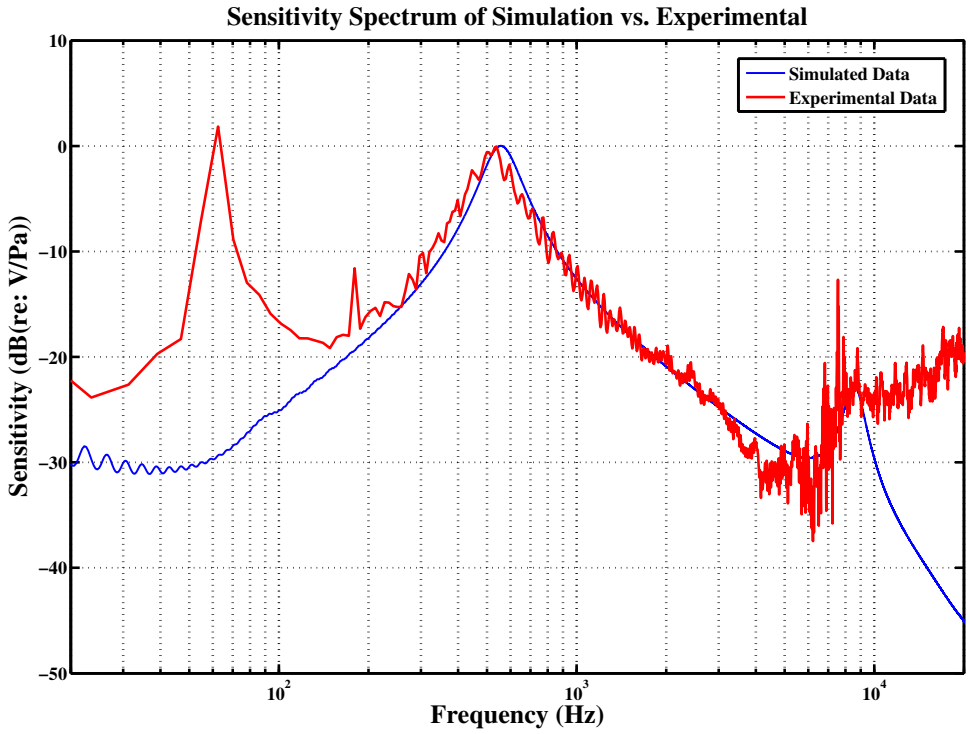

Figure 67: Sensitivity spectrum of simulation and experimental data

The simulation as shown in Figure 67 was very similar to the experimental data.

One discrepancy in the spectrum was that there was a 60Hz signal in the experimental data; this was due to an electromagnetic coupling effect occurring with a power line somewhere in the setup. Since the source could not be located the 60Hz signal persisted throughout the testing of the device. Another notable difference was at frequencies above 10 kHz the experimental data doesn't attenuate like in the simulation. This was due to the signal being dominated by measurement noise. The model also was able to include directionality patterns, which was critical in later analysis that looked into control strategies affecting directionality patterns. Several of the directionality patterns are shown in Figures 73 -75 overlaid with measured data on the devices.

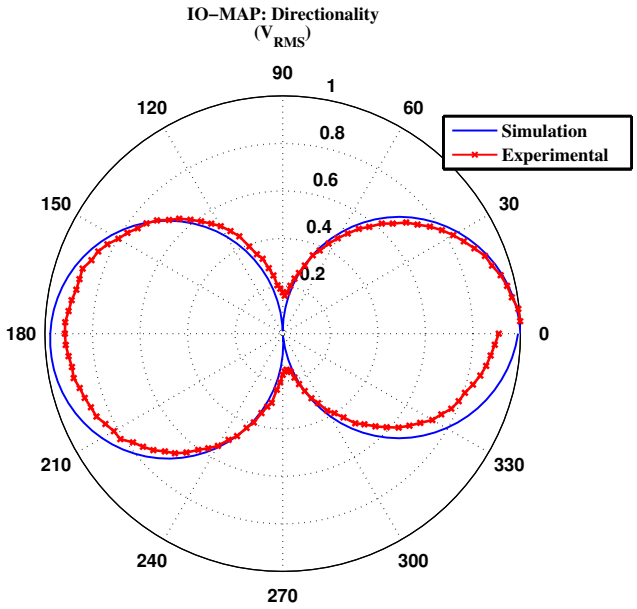

Figure 68: Directivity pattern of device with a 500Hz tone

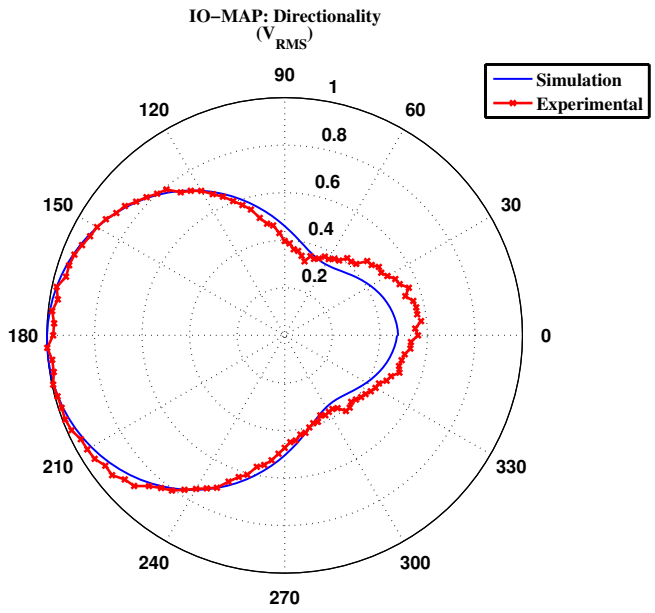

Figure 69: Directivity pattern of device with a 5000Hz tone

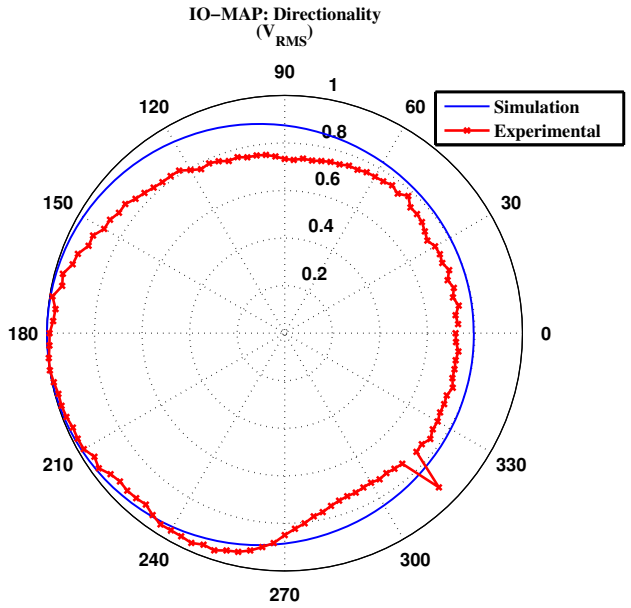

Figure 70: Directivity pattern of device with a 9000Hz tone

As seen in Figures 73 -75, the model was able to predict the asymmetry in the

directivity profiles due to the influence of the second mode on gap displacement. Furthermore the simulation allows for voltage feedback to the system in the form of a PID control. Other types of controllers can also be implemented into the model but are not shown in this analysis.

5.2 Dual Feedback Control

It has been suggested that to improve the response of the microphone a simple controller should be implemented to both improve the sensitivity profile of the device and cause the microphone to become more directional. The following analysis looks into this suggestion by applying PID control and observing the results of the system.

The control tries to accomplish two objectives. The first was to shape the impulse response of the diaphragm; the second was to improve the directionality. Since the diaphragms output can be seen as a convolution of the pressure field and the diaphragm's impulse response changing the impulse response will change how the diaphragm senses a pressure input. The different components of the PID controller will affect the spectrum of the device in several ways. The first component is the proportional controller. This component scales the systems outputs and then feeds it back into the system. The result of which is the resonant frequency of the device will shift to a higher frequency, giving the control a stiffening effect. The next component of the control is the integration part of the PID this is less influential to the system's spectrum since it deals with the steady state behavior of the system or DC components, which are typically outside the interested frequency range of the device. The effects of integral control are addressed in the next section for bias control, since the operation point of the diaphragm was more dependent on the steady state behavior of the diaphragm.

The final component is the derivative component of the control. By utilizing derivative feedback, the system is referenced to its velocity; specifically, the velocity

of the sensing side is set to be stationary. The result of this type of control dampens the impulse response of the microphone, which would reduce overshoot and stop oscillatory behavior present in the diaphragms impulse response. The response of the microphone to the different control inputs are shown in Figure 71.

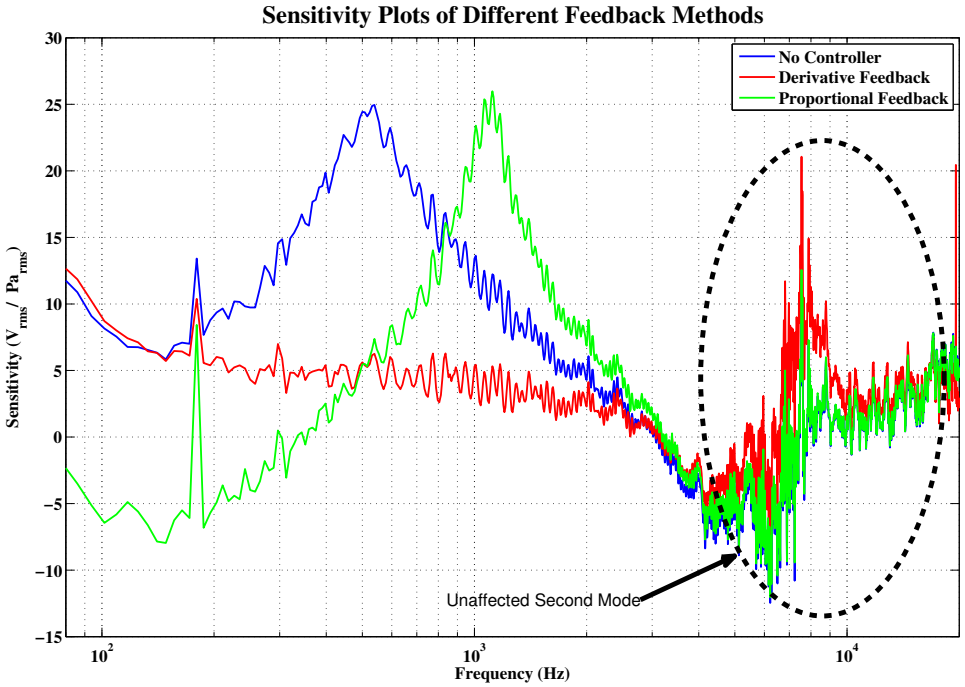

Figure 71: Measured spectrum with proportional and derivative control

For the control inputs shown in Figure 71 have the maximum amount of gains placed on the device, leading to a large resonance shift for the proportional controlled device and a large over damped response for the derivative case. Combining the two components will lead to a response somewhere in between these two cases. Another note about Figure 71 was that after 5kHz the spectrum remains relatively unaffected by the control inputs. It was in this region where the stiffer second mode of the diaphragm and noise are the dominate feature of the signal as such control inputs have little to no effect in this frequency range.

Since the resonant frequency of the first mode was already at an ideal value,

derivative feedback effects were of more interest to control the diaphragm. It was considered that the best operation point then for the controller was to dampen the response to where the response was critically damped. The reasoning was that if the control had insufficient gains the system will remain under damped and so will exhibit ringing behavior in the recorded signal. When gains are too high the system becomes over damped, this will stop oscillatory behavior in the impulse response, but will start to cause the system to have a slower response time since the over damping would increase the settling time of the impulse response.

The derivative control was introduced into the microphone system in a number of different ways to see if there was any affect on the system frequency spectrum. The results of which are displayed in Figure 72.

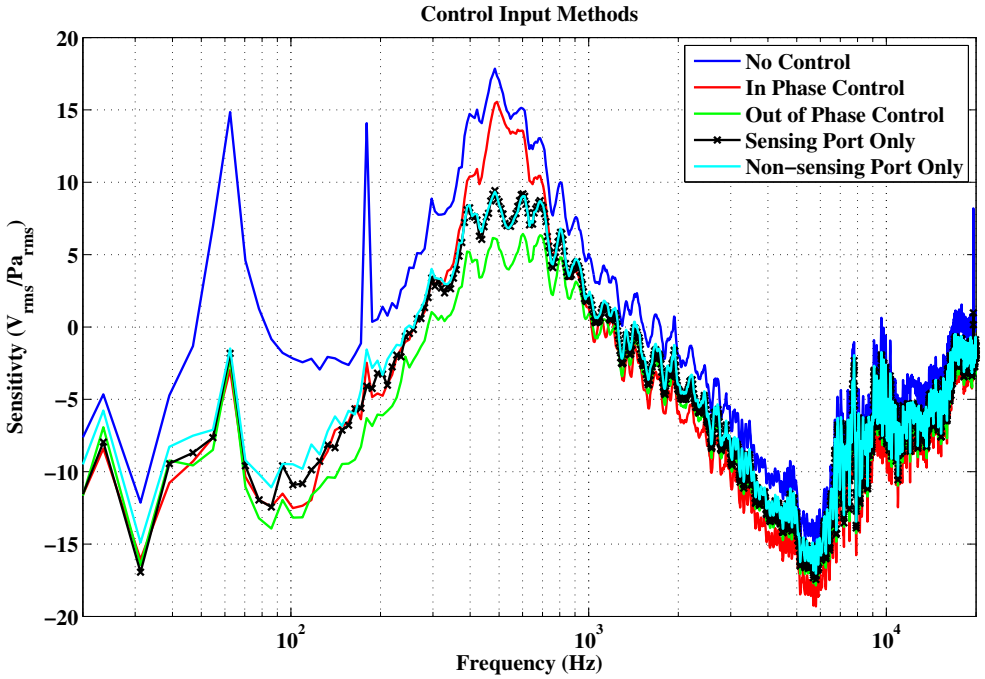

Figure 72: Spectrums with varying methods of control inputs

The gains used for the above results were much lower than the ones shown in the previous spectrum, this was to try and bring the system close to critical damping.

The influence of the control on the spectrum was apparent for the out of phase and single sided control inputs; however, when the signal was applied to both sides in phase there was little difference in the spectrum. The hope of differing the way the control was introduced to the system would help the system response by overcoming the second mode; however it is clear from Figure 72 that the part of the spectrum dominated by this mode was affected very little by the different input methods. This was once again due to the fact that the stiffness of the second mode was relatively large, and so applied forces have little effect on the displacement of the diaphragm.

The changes of the microphones directivity were also looked at for the different control cases. The directivity pattern of the device was governed by the interaction of the two modes. To improve directionality a larger separation of the two mode's amplitudes needs to be achieved. It has already been shown that the two modes of operation are decoupled one being influenced by moments and the other by forces on the diaphragm. Thus the controller should either try and suppress the second mode or enhance the first. Since the proposed control needs to be in negative feedback in order to ensure stability; enhancing the first mode would not be possible. So the control should attempt to suppress the second mode. Both the proportional and derivative controllers were looked at to alter the directivity pattern for the device. The results of the varying controllers on the system's directionality are displayed in the following, Figures 73-75 . The two controllers had the same gains as the ones used in Figure 71.

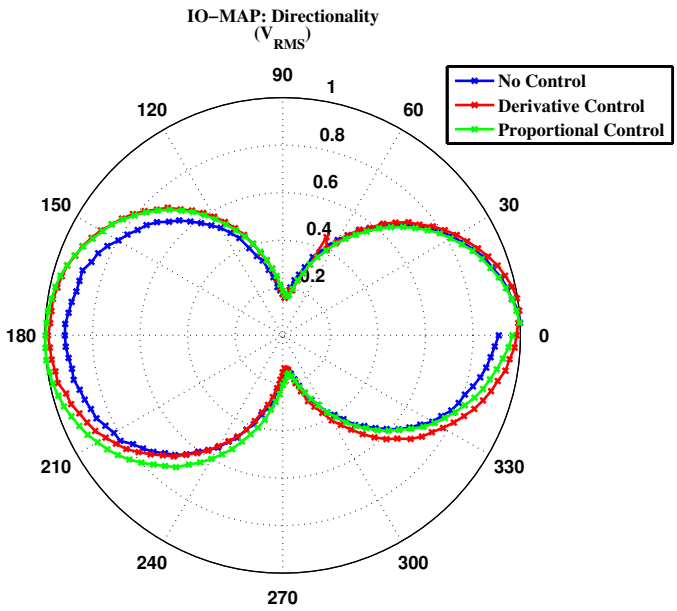

Figure 73: Directivity pattern of device with a 500Hz tone with different control schemes

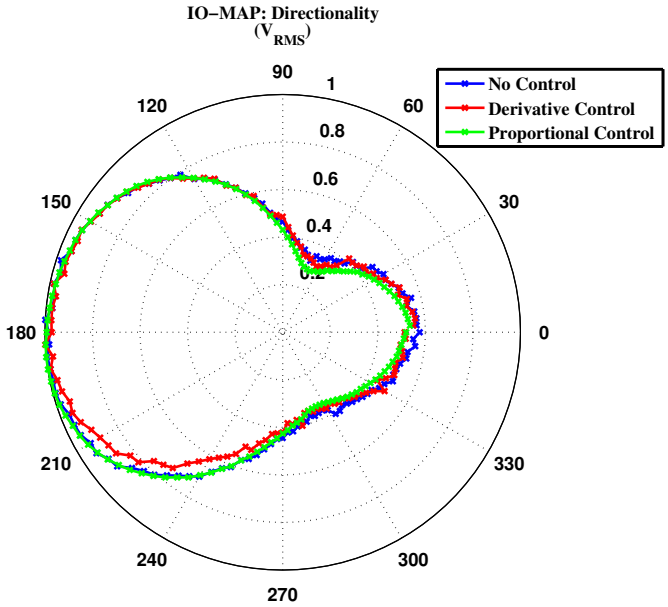

Figure 74: Directivity pattern of device with a 5 kHz tone with different control schemes

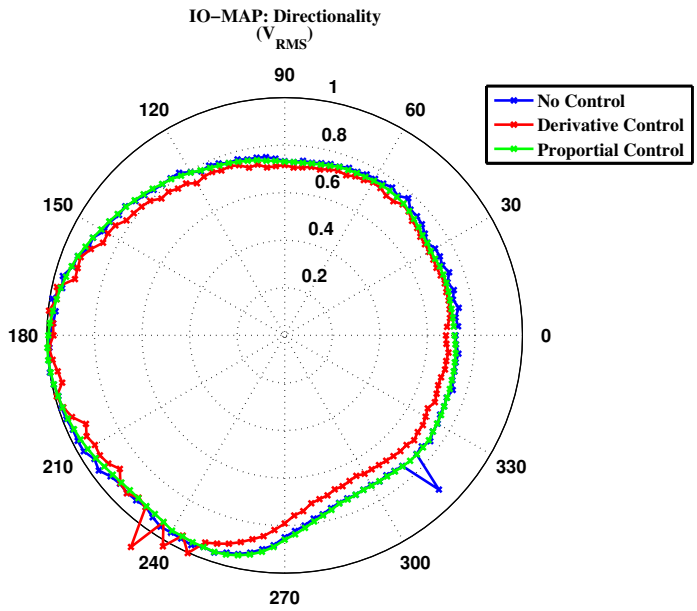

Figure 75: Directivity pattern of device with a 9 kHz tone with different control schemes

As one can see there was little to no change in the directivity patterns of the microphone diaphragm due to the control input. This would indicate that the control does not sufficiently mask or suppress the second mode of the diaphragm.

It was suggested to apply a symmetric input to the system to only affect the second mode. This however did not work well since, the need to bias the diaphragm evenly makes it difficult to operate the device on a more sensitive optical region due to the larger voltages required. Figure 53 is a clear example of how much voltage was required to bias the device evenly, as indicated by the dotted linear lines in the contour plot. The problem was made worse by the feed forward effect of the electrostatic inputs, where even if the gains were achieved the system would be marginally stable. Meaning a perturbation from the equilibrium forcing will cause the diaphragm to snap down since the voltage level will be higher than the voltage level for the rotation mode of the diaphragm.

Other PID controller strategies were tried using the SIMULINK model discussed in the previous section. What was found was that despite being able to influence the impulse response of the system, the directivity either remained unchanged or worsened under the new gains. While it still may be possible to improve directionality with a control input, the control law necessary to do so would have to be more sophisticated than just a simple PID feedback loop, which in turn would more than likely require full state feedback of the system. In addition more sophisticated controllers are discouraged for hearing applications since time delay for the device was critical. [47]

Another issue that will still be present even with ideal damping would be the distortion of the pressure field due to the derivation of the input signal. This issue can be addressed in two different approaches. The first was to over dampen the system to limit the distortion, the advantage being it was a simple way to address the issue. The other way would be to introduce a notch filter that would cancel out the distortion of the signal due to the diaphragm dynamics. This was ideal, since the total system would be a flat frequency response; however, inverting the dynamics was non-trivial and robustness is a major concern for the system.

5.3 Bias Control

5.3.1 Controller Description

For proper operation of the device it was important to be able to control the gap displacement of the diaphragm so the device operates in a linear region of the optical sensing curve as shown in Figure 14 . If the device does not operate in this region then harmonics are generated due to the nonlinearities presented in the optical curve. Furthermore, since the signal's sensing origin was not in the center of the sine curve it was more likely to exhibit clipping when sensing a pressure field. It was for all these reasons why biasing was a major concern for the devices.

It was found during the testing of the microphone diaphragms that some of the

devices exhibited charging effects. This meant that the devices were not able to be properly biased since after a certain amount of time the charge between the grounded diaphragm and the electro statically charged gold mirrors would be lost, and the microphones point of operation would shift. To address this issue, a control design was proposed to compensate for this drift in DC bias.

The controller that was proposed was made up of four different components. The first of which was a low pass filter with cutoff frequency around 20Hz. The main purpose of this component was to only look at the DC components of the signal being recorded. Since it was infeasible to continuously have to sweep the optical curve during operation it was assumed that by holding the DC part of the signal at a constant value it would also keep the device at an optimal sensing point. The filter chosen was a simple Butterworth filter; however, because the diaphragm mechanically differentiates any input pressure signal a first order filter would not have worked for the system. Thus a Butterworth filter with a order higher than 1 was chosen, for the design a 6th order filter was used; however, any order filter above 2 would have been sufficient for the microphone system.

The design of the filter was first to choose the six poles of the circuit transfer function with natural frequency of 20Hz, the desired cutoff frequency of the low pass filter. In the s-domain these poles are chosen to be equal distant over the left half of a circle with radius equal to the natural frequency and centered on the origin. To implement this transfer function in a circuit a Sallen-Key lot pass filter circuit was chosen, which acts as a second order Butterworth filter. The circuit diagram is shown below in Figure 76.

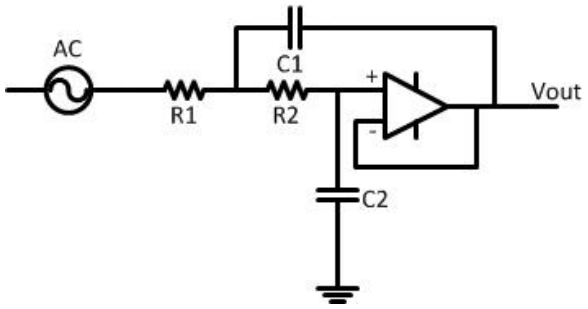

Figure 76: Circuit schematic of Sallen-Key low pass filter

The transfer function of the circuit can be calculated as seen below.

$$H(s) = \frac{1}{1 + C_2(R_1 + R_2)s + C_1C_2R_1R_2s^2} \tag{47}$$

To make the calculation of the poles easier both resistors were chosen to be the same value, which was 1MΩ. The resulting capacitance values used for the bias controller are shown in the following table.

Table 4: Sallen-Key low pass butterworth filter capacitor values

Stage	C_1	C_2
1	8.2431 nF	7.6905 nF
2	11.2598 nF	5.6298 nF
3	30.7651 nF	2.0605 nF

Each stage represents another Sallen-Key circuit, because the filter design was a sixth order filter there are 3 circuits in series.

The next component of the controller was a difference circuit. The main purpose for this was to compare the DC component of the signal to a reference value and output the error signal for the controller. Once the error signal was outputted it was fed into the next circuit, which was a leaky integrator. The integrator was to add a certain amount of memory into the system this was so the corrective control input wouldl not dissipate after error goes to zero. The cutoff frequency chosen for the

integrative circuit was at 0.1Hz and the gain for the output was initially chosen as 1 although quicker settling times can be achieved if larger gains are used. The last circuit was a non inverting summing circuit, which added the new corrective input to the DC bias supplied initially to the diaphragm. The total circuit schematic is shown in Figure 77 with each component identified.

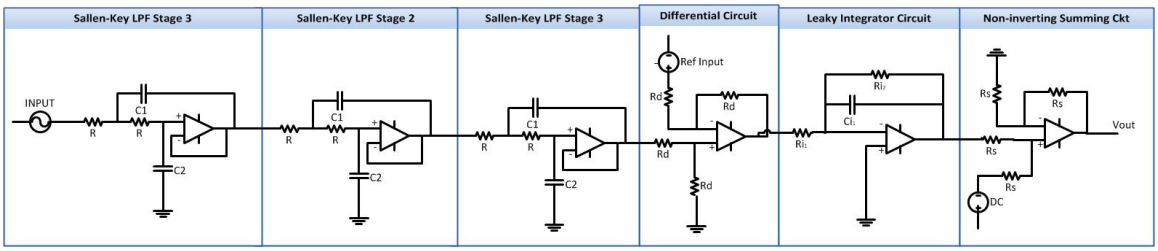

Figure 77: Circuit schematic of bias control

5.3.2 Results

The circuit shown above was assembled onto a bread board and tested on a working device that was known to exhibit the charging behavior. The output behavior of the device was recorded for 15 minutes measuring a constant tone at the device's natural frequency. Time data was taken from the device once every 30 seconds. Figures 78 and 79 that follow show the average voltage value recorded over that fifteen minutes along with 3 time instances during the recording one at the start of the test, one at the conclusion and an intermediary point halfway through the test run. All recordings were triggered with the tone source and were not altered during the test, to preserve the phase relationship of the signal due to charging.

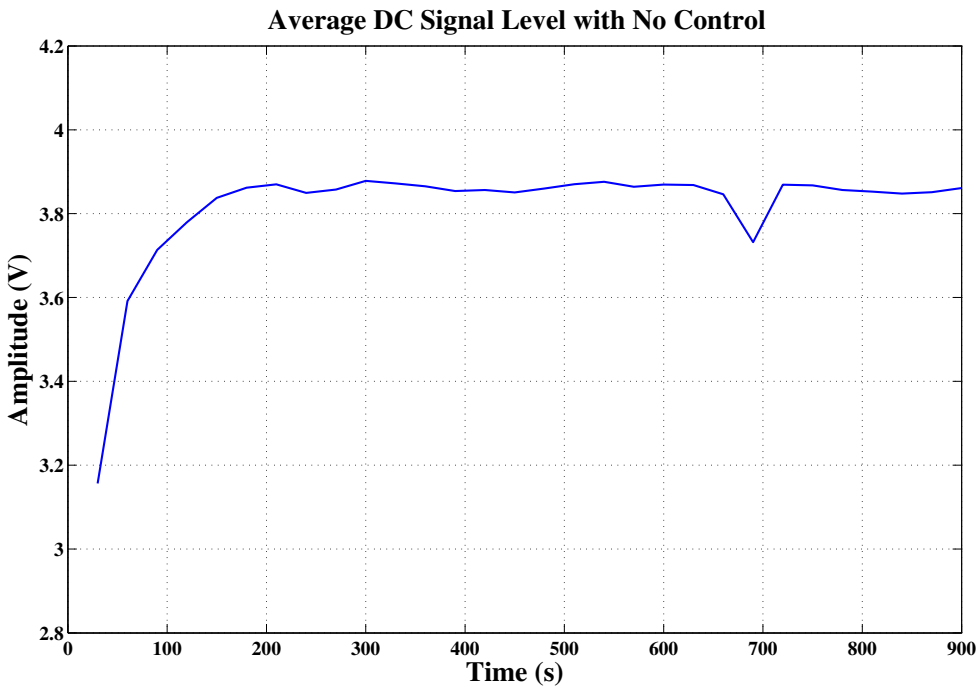

Figure 78: Average voltage output for device with no control

Figure 78 illustrates the charging effects on the microphone diaphragm. While the average value appears to level off at around 200 seconds, the optical curve was still shifting as shown by the change in signals in Figure 79.

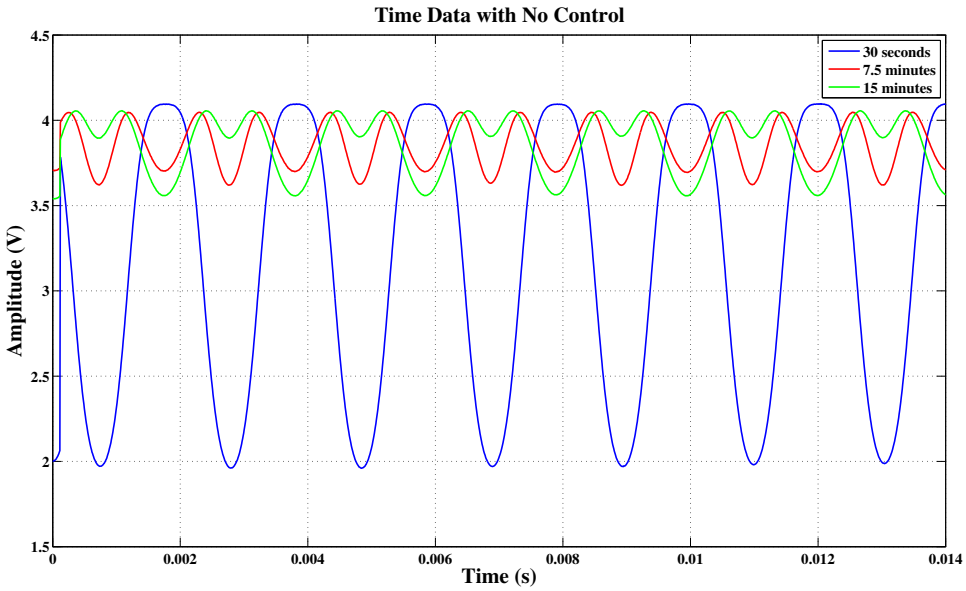

Figure 79: Time data of device with no control

Figure 79 also indicates that the sensing region for the device has shifted to a new part of the optical curve during the charging, this is shown by the time inversion of the detected sine wave. After the run was conducted the device was allowed to discharge and then retested with the bias control active. The bias was chosen such that the sensing region of the optical curve had a positive slope, this was to ensure that the control remained in negative feedback. If a negative sloping part of the optical curve was chosen then the control input would be out of phase and in positive feedback. Also the sine wave used to excite the diaphragm was chosen such that the optical curve was fully saturate. This was done in order to place the controller in a worst case scenario where the change in error can shift drastically due to clipping of the signal on the optical curve, the result of which are shown in Figures 80 and 81.

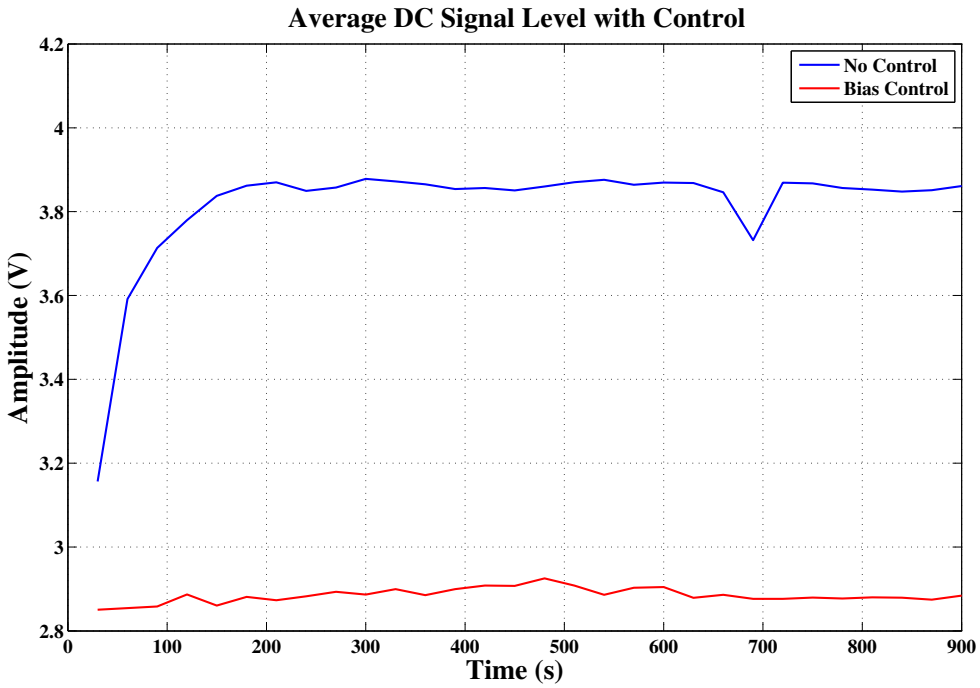

Figure 80: Average voltage output for device with bias control

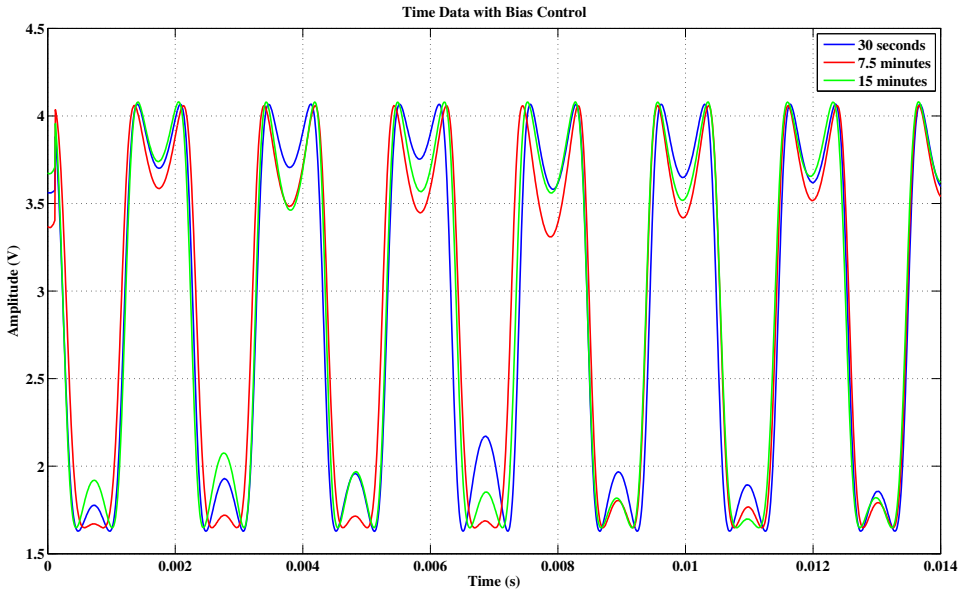

Figure 81: Time data of device with bias control

The results show that by keeping the average at a relatively constant level during the microphone's operation the sensing point of the optical curve can also be maintained. Furthermore it can be said that the control effectively compensates for the effects of charging on the bias point, as seen in Figure 80 with a factor of 8 reduction in bias drift durring the 15 minute operation of the device. In addition, the control has a slow response relative to the interested frequency range and so can be used without affecting the microphone's transient behavior in measuring the pressure fields. Therefore the proposed controller can be used as an "Outer Loop" controller in conjunction with other control methods meant to alter the dynamics of the microphone diaphragm.

CHAPTER VI

CONCLUSION

This thesis introduced the new design of the bio mimetic optical directional microphone. Two packaging methods were also introduced to implement this new design. The first was an adaptation to previous work, where position tolerances were improved and a new optical element was introduced to improve the optical efficiency of the device. The second package that was designed was a practical implementation of the device to be used as a behind the ear hearing aid. This device also contained the new optical lens array and featured a SLA model of the BTE commercial package.

The finished packages were then characterized via several tests to find out key parameters of the devices. The results showed that the new design with optical lens array was able to improve the optical efficiency of the device from under 1% efficiency to upwards of the photodiodes collecting 50% of the 2mW emitted from the VCSEL source, which lead to a significant improvement in the signal strength of the devices. Also what was found in the characterization was that the new noise levels of the device were also improved. One device showed noise levels of 30.6 dBA SPL with proper biasing, which was not only close to the theoretical noise limit calculated for that device, but showed a vast improvement ($>$ 6 dBA SPL) of the noise level when compared to previous designs and commercial directional microphones. Also recorded was the device's optical profile with the presence of dual biasing. The results of which showed the sinusoidal behavior of the optical sensing curve and the hyperbolic relationship of the inputs to the diaphragms gap displacement. A final characterization test that was conducted for the devices was a directivity test. At the conclusion of this analysis what that the microphone was indeed directional up to

5kHz but exhibited asymmetry in the directivity pattern around 3kHz, as the second mode started to dominate the detected signal. At 9 kHz where second resonance was the microphone was essentially omni directional, but still asymmetric.

The thesis also discussed a power saving operation of the device. This was achieved through driving the VCSEL source with a pulse train at varying duty cycles. The results from the study showed that SNR at a certain frequency can be preserved so long as the thermal mechanical noise was still dominating the noise spectrum of the device. Furthermore, dBA SPL noise levels were able to be kept to an acceptable level till around 20% duty cycle, meaning the device could operate with the VCSEL drawing one fifth of its original power without much degradation in the detected signal.

Finally the thesis concluded by looking at control strategies that could be used to improve the operation of the device. This chapter first discussed a full model simulation of the microphone package which allowed for estimation into both the microphone's spectrum and directional characteristics. The thesis then divulges into looking at how feedback control alters the directivity profile of the device and makes the conclusion that improvement of the directionality was not feasible with classical control methods. Then a bias controller was discussed, which when implemented on a working device was shown to hold the bias point constant despite being influenced by charging effects. A reduction in bias drift of a factor of 8 was shown to be possible during a 15 minute period using the bias control.

Some suggestions for the future improvement for the device would be first to re-design the diaphragm to push the first resonance to a higher frequency; this would in turn also make shift the second resonance above the interested frequency range. One potential downside to this approach is a loss in detection of lower frequency sound sources. Another characterization method that also needs to be looked into

is the spectrum change when the BTE device is on a person's head, since the device would then be exposed to a reflective surface. In addition to this a protective cover would need to be implemented onto the device and its effects on the system recorded. Another packaging issue that should be conducted is analysis on the effects of thermal cycling of the device. Since the VCSEL heats up over long periods of operation the package temperature can vary significantly, this over time can shift the alignments of the components. Finally the control and filtering of the microphone should be addressed in more depth, such as looking at nonlinear methods to improve the directionality of the device.

APPENDIX A

IO MAP PREAMPLIFIER TUBE

Figure 82: IO Map preamplifier tube with connection ports shown

The image shown above is the input output (IO) map preamplifier tube that the microphone packages interface with. There are two main purposes for the tube, the first was routing the signals going to and from the device's 12 pin connection to the LIMO cable, which was connected to the proper voltage supplies and measurement equipment. The second purpose was to house the trans impedance amplifier (TIA) circuitry. The reason why this circuitry needed to be housed in the IO map tube was to reduce noise due to parasitic capacitance. It does this by amplifying the detected signal before noise from connecting wires adds to it. The following image is the schematic of the circuitry used to amplify the photodiode current from the device.

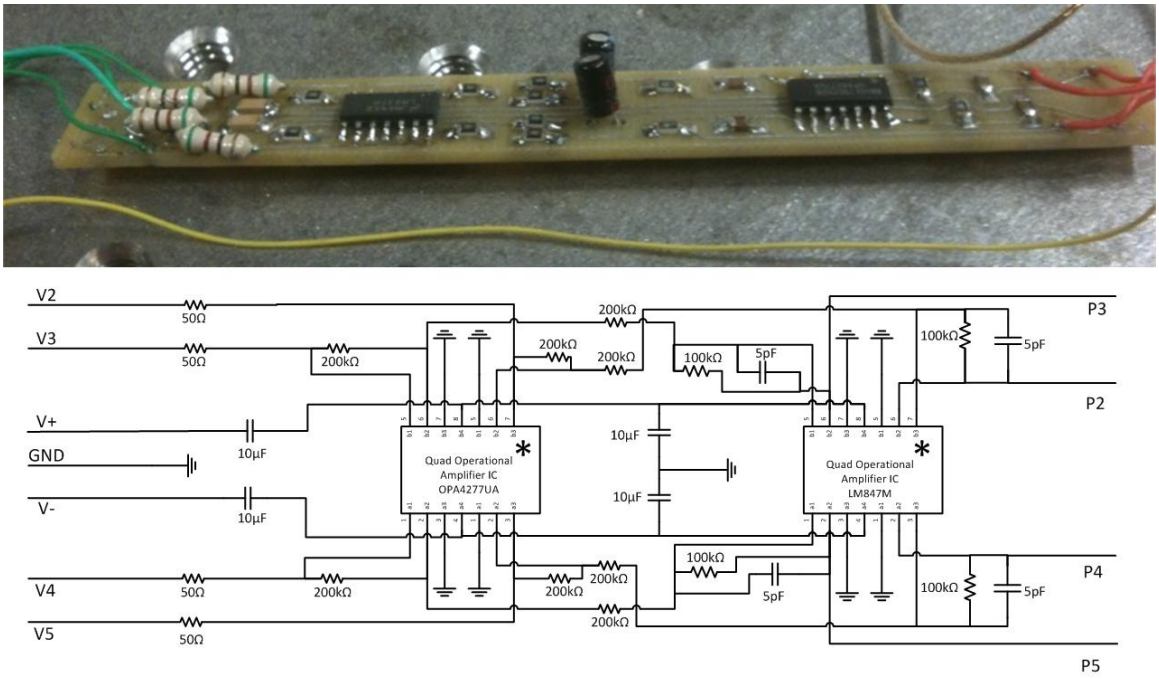

Figure 83: Transimpedance circuit housed in the IO map

This circuit serves to amplify the photodiode current output by a prescribed gain and convert it into a voltage value. P2 through 5 represents the pins on the TO Header of the device, and contains the incoming photodiode current. V2 through V5 is the voltage output of those pins after the signal goes through the TIA circuit. V+/- are the supply voltages to the amplifiers and GND is the ground wire. In this study the gains chosen for the amplifier was 100k; however, work done previously to this used a 200k gain [26, 28, 37, 38]. The reduction in gains was necessary to avoid saturation of the amplifiers due to the increased optical efficiency of the devices producing higher current outputs.

The tube was comprised of two quad operational amplifiers. The first amplifier that the incoming signal sees was the TIA circuit, which has a cutoff frequency for amplifying around 300kHz. The second operational amplifier was an inverter circuit so the device produces a positive voltage value since the TIA circuit is an inverting amplifier. Other pin connections to the device, such as VCSEL power supply and

the two electrostatic ports were routed through the tube via coaxial cable to their respective pins.

APPENDIX B

SIMULINK MODEL OF MICROPHONE

The derivation of this block diagram was based off the theory discussed in Chapter 5, Section 1. The overall model which is shown in Figure 84.

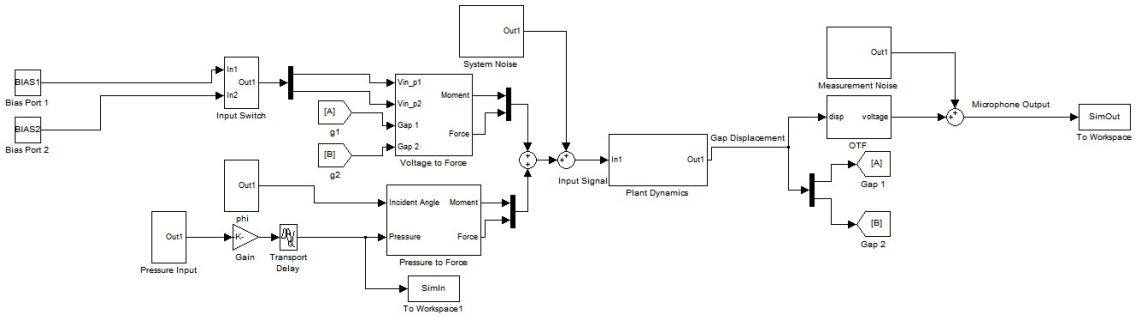

Figure 84: Block diagram of the microphone package

Goto and From blocks were used to keep the model from having too many crossing wires, e.g. the gaps used these blocks to feed the gap displacement back into the electrostatic force submodel. The total model was made up of several submodels depending on a different component or transduction method the microphone uses to get gap displacement. Figure 66 shows a clear representation of those submodels and what they represent in the physical system. The noise for those models was considered to be white and Gaussian due to their large broad band behavior and zero mean average.

The plant dynamics are a state space representation of the dynamical model discussed in Chapter 3, Section 1. The state space block representation is given in more detail with figure 65, which has the system matrices defined above it. The SIMULINK model was similar and is shown in Figure 85.

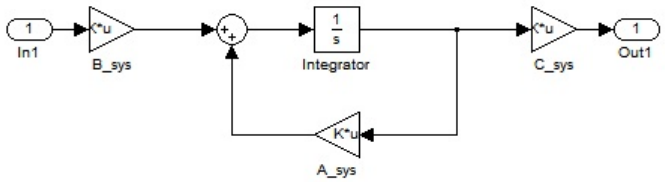

Figure 85: State space block diagram (plant dynamics submodel in Figure 84)

The electrostatic force was modeled such that any voltage input would give back a force and moment value exerted on the pivot of the microphone diaphragm. Figure 84 shows an open loop representation of the system with only biasing; however, feedback can be added with the biases to affect the system. Block representation of Electrostatic forces are shown in Figure 86.

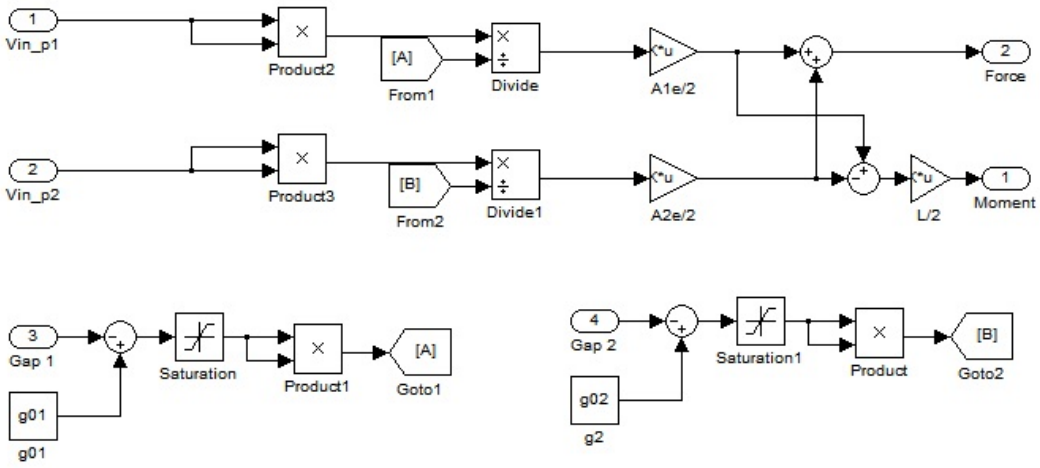

Figure 86: Block diagram of the electrostatic force

The block first squares the input voltages as well as the gap displacements. Then it divides these two quantities and multiplies the result by a constant. At this point the voltage input was a force value. The forces are then added together to output the net force acting on the diaphragm. The moment was calculated by taking the differences

in the force values and then multiplying by one half the length, the moment arm of the force on the diaphragm. The saturation blocks in the diagrams simulate if the gaps were to collapse due to a strong electrostatic force causing the two electrodes in the parallel plate assumption to stick together.

The reason why the system was modeled with moments and force instead of pressure and electrostatics was because of the unique nature of the device to derive the pressure input. The submodel of Pressure to Force allows the pressure to be derived and feed into the system such that the electrostatic and pressure models could use the same dynamic model. The pressure sub model is shown in Figure 87.

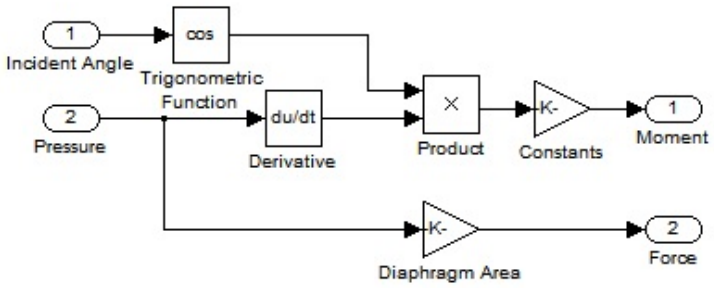

Figure 87: Block diagram of the pressure inputs

The above figure a cosine function was added to the block diagram to capture the directivity response of the diaphragm to pressure. The constants that are then multiplied to the moment are contained in equation 18. The remaining sub models were very simplistic so their block representation isn't shown. The optical transfer function submodels was created with a gain block ($2\pi/\lambda$) and a sine trig function block. The TIA was just a gain block that would contain the amplifier gain of 100k the value used in the package, and the nu term as a normalizing factor for losses that could not be characterized as well e.g. photodiode efficiency.

APPENDIX C

SIMULATION M-CODE

The following code will set all the parameters used in the model and then run the simulation.

```
close all
clear all
set(0,'defaultfigurewindowstyle','docked')

%% Settings
NOISE_TEMP = 0; % Temp Noise (0:off 1:on)
NOISE_ELEC = 0; % Electronic Noise (0:off 1:on)
Sampling = 0; % Turn Sampling On and Off
DIRECTIONALITY = 1; % Directionality (Incident angle sweep on or off)
phi    = 0; % incident angle (Only used if Directionality is off)
inc    = 3; % angle increments
Control = 0; % Control on or off
ProportionalGain = 0; % Gain for Proportional Control
DerivativeGain = 1e-5; % Gain for Derivative Control
IntegralGain = 0; % Gain for Integral Control
InputGain = .1; % Amplitude of Input Pressure Signal
INPUT = 3; % Select Input ports (1: Port 1 2: Port 2 3: Both)
PressureInput = 2; % Pressure Input (1:Chirp 2:Tone 3: Off)
ToneFreq = 500; % Tone Freq in Hz
BIAS1 = 0; % Bias Voltage port 1
BIAS2 = 0; % Bias Voltage port 2
ts = (44.1e3)^-1; % Simulation sample time
t_f = .1*124; % Final Simulation Time
```

```
%% System Variables
Kb = 1.38e-23;assignin('base','Kb', Kb); % Boltzman's Constant
m = 8e-8;assignin('base','m', m); % equivalent mass
L = 2.2e-3;assignin('base','L', L);  % Length of the diaphram
width = 1e-3;assignin('base','width', width); % width of the microphone
Iyy = 1.25e-14;assignin('base','Iyy', Iyy); % Rotation Moment of Inertia
Ia = width*L^3/12;assignin('base','Ia', Ia); % Area Moment of Inertia

c_t = 1.75e-11*.75;assignin('base','c_t', c_t); % dampening 1st order
c_x = 0.0019*.7;assignin('base','c_x', c_x); % dampening 2nd order
k_t   = 1.53e-7;assignin('base','k_t', k_t); % Spring Constant 1st order
k_x   = 240.5358;assignin('base','k_x', k_x);% Spring Constant 2nd order

c0    = 340.29;assignin('base','c0', c0); % speed of sound wave [m/s]
lambda= 850e-9;assignin('base','lambda', lambda); %laser wavelength

Vac = 2;assignin('base','Vac', Vac); % Saturation AC level of diaphragm
Vdc = 4;assignin('base','Vdc', Vdc); % DC level of device
% Area of grating
A_grating = 100e-6*150e-6;assignin('base','A_grating', A_grating);
% permitivity of free space
e_v = 8.85418782e-12;assignin('base','e_v', e_v);
g01 = 10e-6;assignin('base','g02', g01); % Inital Gap Port 1
g02 = 10e-6;assignin('base','g01', g02); % Inital Gap Port 2
Nu_Opt =.0001*1/3;assignin('base','Nu_Opt', Nu_Opt); %Normalizing Optics
PreAmp = 100e3;assignin('base','PreAmp', PreAmp);  % Preamplifier Gain

%% Noise Levels
% Thermal Noise at 1st mode
Sn_T1 = Kb*293*7.389e-12/pi;assignin('base','Sn_T1', Sn_T1);
% Thermal Noise at 2nd mode
Sn_T2 = Kb*293*0.0019126*1e-13/pi;assignin('base','Sn_T2', Sn_T2);
```

```
% Electronic Noise Floor
Sn_E = 10^(-114/20);assignin('base','Sn_E', Sn_E);

%% System State Space Dynamics
% System Matrix
A = [ 0          1          0          0          ;...
     -k_t/Iyy    -c_t/Iyy   0          0          ;...
      0          0          0          1          ;...
      0          0          -k_x/m     -c_x/m     ];
% Input Matrix
B = [0 1/Iyy 0 0;0 0 0 1/m]';
% Measurement Matrix
C = [ L/2 0  .25 1e-5;-L/2 0 .25 1e-5];
% Feed Through Matrix (Usually Zero for many Dynamic Systems)
D = [0 0;0 0];
% Creates a formatted state space object
SYS_Continous = ss(A,B,C,D);
% discretizes the dynamics to sampling ts
SYS_Discrete  = c2d(SYS_Continous,ts);

% Chose whether system is discrete or continous in SIMULINK model
switch(Sampling)
    case 1
        A_sys=SYS_Discrete.A;
        B_sys=SYS_Discrete.B;
        C_sys=SYS_Discrete.C;
    otherwise
        A_sys=SYS_Continous.A;
        B_sys=SYS_Continous.B;
        C_sys=SYS_Continous.C;
        Sampling =0;
end
```

```
89 % Feed Resulting System Matricies to the Workspace
   assignin('base','A_sys', A_sys);
91 assignin('base','B_sys', B_sys);
   assignin('base','C_sys', C_sys);
93 %Run Simulation via SIMULINK
   sim('SimModel');
```

REFERENCES

[1] http://www.capehearingaids.co.za/Hearing%20Aid%20Types.htm.

[2] "Eutectic die collets 3600 & 3700 series." http://www.gaisertool.com/products/other/die-1.pdf. Gaiser Tool Company Catalogue.

[3] "Lasermate." http://www.lasermate.com/VCC85A1G-IS.html.

[4] "L.d. ref600." http://www.larsondavis.com/docs/REF600_500Datasheet.pdf.

[5] "Wave interference." http://lindahuang-sph3u.blogspot.com/2011/01/wave-interference.html.

[6] "Program of the twenty-third meeting of the acoustical society of america," vol. 12, pp. 461–476, Acoustical Society of America, January 1941.

[7] "Program of the twenty-eighth meeting of the acoustical society of america," vol. 15, pp. 76–81, Acoustical Society of America, May 1943.

[8] *Microphone Handbook*, vol. 1. Naerum, Denmark: Bruel and Kjaer, 1996.

[9] "Engineering acoustics: Silicon sensors," pp. 997–999, Acoustical Society of America, March 1999.

[10] "Equipment specs." http://www.enme.umd.edu/vibnoise/vib_Web/EquipmentSpecs.html, March 2002. Vibration & Noise Control Laboratory University of Maryland Mechanical Engineering Department.

[11] "Michelson interferometer: electromagnetic radiation." http://www.britannica.com/EBchecked/topic/380060/Michelson-interferometer, 2006. Encyclopedia Britannica Inc.

[12] Ambardar, A., *Analog and Digital Signal Processing Second Edition*. 1999.

[13] Bao, M. and Yang, H., "Squeexe film air damping in mems," *Science Direct*.

[14] Bicen, B., "Micromachined diffraction based optical microphones and intensity probes with electrostatic force feedback," phd thesis, Georgia Institute of Technology, August 2010.

[15] Bilaniuk, N., "Optical microphone transduction techniques," *Applied Acoustics*, vol. 50, pp. 35–63, August 1996.

[16] Bouwstra, S., Storgaard-Larsen, T., Scheeper, P., Gullov, J. O., Bay, J., Mullenborg, M., and Rombach, P., "Silicon microphones - a danish perspective," *Journal of Micromechanics and Microengineering*, vol. 8, pp. 64–68, January 1998.

[17] Cord, M., Surr, R., Walden, B., and Olson, L., "Performance of directional microphone hearing aids in everyday life," *Journal of the American Academy of Audiology*, vol. 13, pp. 295–307, June 2002.

[18] de Bre, H.-E., "The microflown: an acoustic particle velocity sensor," vol. 31, no. 3.

[19] deBre, H.-E., Leussink, P., Korthorst, T., Jansen, H., Lammerink, T., and Elwenspoek, M., "The μ-flown,a novel device measuring aoustical flows," *The 8th International Conference on Solid-state Sensors and Actuators*, vol. 118, pp. 536–539, 1995.

[20] deBree, H.-E., Raangs, R., and Druyvesteyn, E., "Sound intensity measurements with the microflown sensor," *The 33rd International Congress and Exposition on Noise Control Engineering*, pp. 1–11, August 2004.

[21] Dragsten, P., Webb, W., Paton, J., and Capranica, R., "Auditory membrane vibrations: Measurements at sub-angstrom levels by optical heterodyne spectroscopy," *JSTOR*, vol. 185, pp. 55–57, July 1974.

[22] Ecock, J. and Smith, M., "Ppt for levent." Internal Report, July 2011.

[23] Franklin, G., Powell, D., and Emami-Naeini, A., *Feedback Contolof Dynamic Systems, Fifth Edition*. 2006.

[24] Garcia, C., "Packaging and characterization of mems optical microphones," masters thesis, Georgia Institute of Technology, December 2007.

[25] Gayford, M., *Microphone Engineering Handbook*. Focl Press, 1994.

[26] Hall, N. A., Bicen, B., Jeelani, M., Lee, W., Qureshi, S., Degertekin, F., and Okandan, M., "Micromachined microphones with diffraction-based optical displacement detection," *Journal of Acoustical Society of America*, vol. 118, November 2005.

[27] Hall, N. A. and Degertekin, F. L., "Auditory membrane vibrations: Measurements at sub-angstrom levels by optical heterodyne spectroscopy," *Applied Physics Letters*, vol. 80, pp. 3859–3861, May 2002.

[28] Hall, N. A., Okandan, M., Littrell, R., Bicen, B., and Degertekin, F., "Micromachined optical microphone structures with low thermal-mechanical noise levels," *Journal of Acoustical Society of America*, vol. 122, pp. 2031–2037, October 2007.

[29] Jacobsen, F. and de Bree, H.-E., "Measurement of sound intensity: p-u probes versus p-p probes," *The Journal of the Acoustical Society of America*, vol. 118, p. 1510, 2005.

[30] Jacobsen, F. and deBree, H.-E., "A comparison of two different sound intensity measurement principles," *Journal of the Acoustical Society of America*.

[31] Jost, B. and Stec, J., "Refractive fiber optic microphones with ambient acoustic noise-canceling capabilities," *Journal of the Acoustical Society of America*, vol. 98, pp. 1612–1617, September 1995.

[32] Kadirbel, K., Taylor, R., Horowitz, S., Hunt, L., and Sheplak, M., "Design and characterization of mems optical microphone for aeroacoustic measurement," pp. 1–10, January 2004.

[33] Kinsler, L., Frey, A., Coppens, A., and Sanders, J., *Fundamentals of Acoustics, Fourth Edition*. 2012.

[34] Kochkin, S., "Marke trak iii identifies key factors in determining consumer satisfaction," *The Hearing Journal*.

[35] Kuk, F., Ludvigsen, C., and Paludan-Miller, C., "Improving hearing aid performance in noise: Challenges and strategies," *The Hearing Journal*, vol. 55, pp. 34–46, April 2002.

[36] Manalis, S., Minne, S., Atalar, A., and Quate, C., "High-speed atomic force microscopy using an intergrated actuator and optical level detection," *Review of Scientific Instruments*, vol. 67, pp. 3294–3297, Setember 1996.

[37] Miles, R., Q.Su, Cui, W., Shetye, M., Degertekin, F., Bicen, B., and Garcia, C., "A low-noise differential microphone inspired by the ears of the parasitoid fl ormia ochracea," *Journal of Acoustical Society of America*, vol. 125, pp. 2013–2026, Febuary 2009.

[38] Miles, R., Robert, D., and Hoy, R., "Mechanically coupled ears for directional hearing in the parasitoid fly ormia ochracea," *Journal of Acoustical Society of America*, vol. 98, pp. 3059–3070, December 1995.

[39] Olson, H., "Apparatus for converting sound vibrations into electrical variations," October 1932.

[40] pdorn, "Lens array drawing 10-069 part drawing v2," June 2010. Jenoptik Germany Mems Optical.

[41] Qureshi, M., "Integrated front-end analog circuits for mems sensors in ultrasound imaging and optical grating based microphones," phd thesis, Georgia Institute of Technology, August 2009.

[42] Raangs, R., "Exploring the use of the microflown," phd thesis, Lochem University, July 2005.

[43] Sagberg, H., Sudb, A., Solgaard, O., Bakke, K. A. H., and Johansen, I.-R., "Optical microphone based on a modulated diffractive lens," *Photonics Technology Letters*, vol. 15, pp. 1431–1433, October 2003.

[44] Scheeper, P., van der Donk, A., Olthuis, W., and Bergveld, P., "A review of silicon microphones," *Sensors and Actuators*, vol. 44, pp. 1–11, Febuary 1994.

[45] Schultz, T., "Acoustic wattmeter," *Journal of the Acoustical Society of America*, vol. 28, pp. 693–699, July 1956.

[46] Stockham, A., "Gatech 09-107 design report," September 2009. Jenoptik Germany Mems Optical.

[47] Stone, M. and Moore, B., "Tolerable hearing aid delays.ii. estimation of limits imposed during speech production.," *Ear Hear.*

[48] Thompson, S., "Tutorial on microphone technologies for directional hearing aids," *The Hearing Journal*, vol. 56, pp. 14–21, November 2003.

[49] Torkkeli, A., Rusanen, O., Saarilahti, J., Seppa, H., Sipola, H., and Hietanen, J., "Capacitive microphone with low-stress polysilicon membrane and high-stress polysilicon backplate," *Sensors and Actuators.*

[50] Traktman, A., "Eutectic die collets 3600 & 3700 series." http://ent.uci.edu/Hearing%20Aids.htm, 2011. The Regents of the University of California.

[51] Yaralioglu, G., Atalar, A., Manalis, S., and Quate, C., "Analysis and design of an interdigital cantilever as a displacement sensor," *Journal of Applied Physics*, vol. 83, pp. 7405–7415, March 1998.